



UNIVERSITY OF TWENTE.

Faculty of Electrical Engineering,
Mathematics & Computer Science

Design and fabrication of an ultrafast expanding microbubble valve array for use in a microreactor to measure sub millisecond reaction kinetics

Nishant Mishra
S2252570
M.Sc. Thesis
30th August 2021

Committee:

Prof. Dr. Ir. Mathieu Odijk

BIOS- Lab on a chip Group
Faculty of Electrical Engineering,
Mathematics and Computer Science
University of Twente, The Netherlands

Dr. Ir. Roald M. Tiggelaar

MESA+ NanoLab Cleanroom
MESA+ Institute for Nanotechnology
University of Twente, The Netherlands

Dr. Ir. Remco J. Wiegink

Integrated Devices and Systems Group
Faculty of Electrical Engineering,
Mathematics and Computer Science
University of Twente, The Netherlands

Design and fabrication of an ultrafast expanding microbubble valve array for use in a microreactor to measure sub millisecond reaction kinetics

Nishant Mishra¹, Johan G. Bomer¹, Henk-Willem Veltkamp², Meint J. de Boer², Roald M. Tiggelaar², and Mathieu Odijk¹,✉

¹BIOS Lab on a Chip Group, MESA+ Institute for Nanotechnology, Technical Medical Center and Max Planck Institute for Complex Fluid Dynamics, University of Twente, The Netherlands

²MESA+ NanoLab cleanroom, MESA+ Institute for Nanotechnology, University of Twente, The Netherlands

Photoelectrochemical reduction of Carbon Dioxide can be used to sequester carbon and provide synthetic alternatives to fossil fuels. The yields of these electrochemical reduction reactions can be improved using catalysts. Better catalysts can be designed by studying the kinetics of these reduction reactions. Infrared spectroscopy is one of the techniques to study these reactions. Recent advances in laser sources have enabled infrared spectroscopy in microseconds. Now, mass transport of gases needs to be controlled on the same time scale. In this work, a design cycle to fabricate a microvalve for controlling mass transport in a sub millisecond time scale was executed. A survey of the potential valving mechanisms on a microreactor was conducted. This was followed by design, simulation and calculations based on device dimensions, deflection and gas flow rates through such valves. A novel cleanroom process was used to define features at different depths with a single exposure mask. Photomasks were designed keeping the design choices and process flow in mind. Optimization of the process for fabricating these structures was attempted. The heat flow was modelled and the input electrical power was calculated. A control scheme for these valves was designed.

ultrafast valve | thermopneumatic bubble valve | super critical heating | single-mask pre-shape assisted multi-feature structures | aspect ratio dependent etching | multi depth structures | membrane release

Correspondence: m.odijk@utwente.nl

1. Introduction

Artificial photosynthesis is a class of chemical reactions used for storing solar energy in the form of chemical bonds of synthetic hydrogen or hydrocarbons(1). Such solar fuels, made from carbon dioxide (CO_2) or water, are possible alternatives to traditional fossil fuels. When matured, artificial photosynthesis could help slow down global warming by not only limiting the use of fossil fuels but also sequestering CO_2 from the air(1, 2).

Electrochemical reduction reactions of CO_2 with copper catalysts are of particular interest as they can produce hydrocarbons like "methane, ethylene, and ethanol with acceptable efficiency"(3). These reduction reactions with a solid catalyst and gaseous reactant are examples of heterogeneous catalysis, where the reactants are in a different phase from the catalyst. To study these catalyzed reactions for CO_2 reduction, many computational modeling methods such as density

functional theory, computational hydrogen electrode, potential dependent activation energy, molecular dynamics simulations, and solvation methods have been used(4). Experimentally, gas chromatography has been used to study the reaction products(5). However, this experimental work measured the gas phase products on the scale of 5 minutes to an hour and unstable intermediate products might not have been detected in this study. Apart from gas chromatography, another popular class of non-destructive methods to detect reaction products is electromagnetic spectroscopic analysis.

Spectroscopic analytical techniques measure the interaction of electromagnetic radiation and matter(6). A variety of spectroscopic techniques such as infrared (IR)(7, 8), Raman(9) (10), UV-Visible (UV-Vis)(11), and X-Ray absorption(12) have been used to study catalysis. A recent review of these techniques can be found in the work of Solsona et al. Mid infrared (4000 cm^{-1} to 400 cm^{-1}) spectroscopy is especially interesting for studying organic compounds, as it measures the various vibrational, rotational and vibro-rotational transitions of the chemical bonds(14). Recent advances in quantum cascade lasers and optical frequency comb techniques(15) have enabled mid IR Spectrometry in the 1-4 μs range(16). With a well-defined starting point, and enhanced mass transport for reactions, these improvements in IR spectroscopy technologies can enable us to study the intermediate reaction products at an ever shorter timescale using microreactor platforms(17). More information on catalysis, intermediate products, and Attenuated Total internal Reflection infrared spectroscopy (ATR-IR) can be found in Supp. note 1.

Microreactors are devices with features on the sub-millimeter scale on which continuous chemical processes are performed(1). A number of steps such as catalysis, mixing, heating, cooling, and analysis can be performed on a microreactor platform utilizing the high surface area to volume ratio when down scaling(18). The precise control of mass transport, as well as heat flow make microreactors useful in organic synthesis reactions(19). A picture of a microreactor for preferential oxidation of Carbon Monoxide outlining the main components is shown in Fig. 1(20).

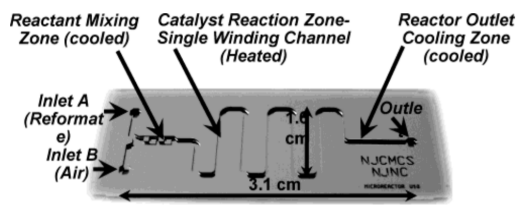


Fig. 1. Various components of a typical microreactor (Figure from (20)).

Microreactors are suited not only to photocatalytic reduction of CO_2 (21, 22), but can also be incorporated with spectroscopy to study the reaction processes (23–25). A schematic of a microreactor with integrated optics is shown in Fig. 2.

This work focuses on the design, simulation, and fabrication of an array of ultrafast microvalves for a microreactor with integrated ATR-IR sensing. The microreactor with ATR-IR sensing, described in the next section, can help detect the instantaneous products formed in photoelectrochemical reduction of CO_2 and aid the design of catalysts for artificial photosynthesis.

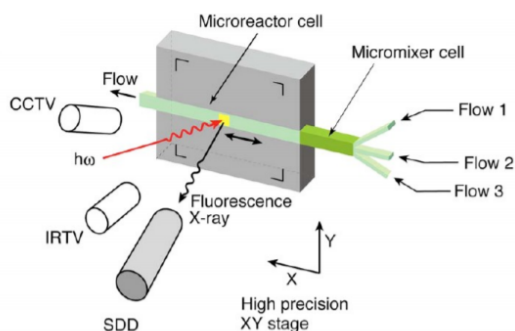


Fig. 2. An example of a microreactor with integrated optics (Figure from (23)).

2. Framework

This work was done in the context of previous work by Haverkate et al. which combined the advantages of Quantum Cascade Laser sources for IR spectroscopy, with those of microreactors. In their work, a platform (schematic in Fig. 3) was proposed to be built for screening suitable catalysts for CO_2 reduction. The microreactor platform was designed to study the short lived reaction products by taking advantage of the recent improvements in the speed of ATR-IR measurements. The proposed platform chip consists of various parts including an Internal reflection element (IRE) that acted as a waveguide for IR light along with the reactor chamber lined with the catalyst, as well as inlet and outlet valves for the reactant and product gases. Switching characteristics of these valves was critical to device operation. The valves would define a clear start to the reaction. Quick and precise mass transport would further allow filling and flushing the reactor to make multiple ATR-IR measurements, improving the signal to noise ratio.

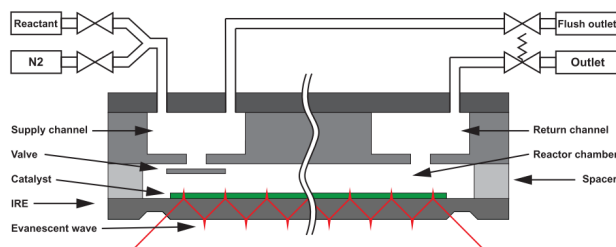


Fig. 3. Cross sectional schematic of the device platform proposed by Haverkate et al. (Figure from (17)).

In the previous work by Haverkate et al., a modular design of the different functions of the chip was proposed. However, no complete chip was fabricated due to device complexity and limited yield of the processing. In the scope of this work, we aim to execute a design cycle for the valves to be used in is ATR-IR microreactor on chip proposed by Haverkate et al. The present work is however limited to only fabricating the actuator, and valve head but not the valve seat, microfluidic channels, or reactor chamber with the catalyst and ATR-IR waveguide.

Besides pumps, valves are one of the most essential components in a microfluidic system that control the motion of a fluid (26). In the work of Haverkate et al., the desired characteristics of the valve were determined. A high operating temperature of up to $450^\circ C$ in the reaction chamber is needed to be able to analyze a variety of gas phase reactions. Further, a high operating outlet pressure of 10 Bar was required to enhance the diffusive flux of the gas into the chamber. In addition to this, the overall system operation cycle is desired to take $200\mu s$ or less. The time for diffusion based inflow of gas into the reaction chamber was calculated to be $80\mu s$ for an array of 5125 microvalves with an inlet radius of $5\mu m$ and a chamber of dimensions $20mm \times 10mm \times 5\mu m$.

3. Valving mechanisms

Based on the design criteria for this system mentioned above, we need the microvalve to operate within the sub-millisecond time scale, at a high outlet pressure, and high operating temperatures. A microvalve converts an electrical signal into a change in the pressure or fluid flow (27). As shown in Fig. 4, a valve has three main components- a channel where flow is to be controlled, a movable head or boss, and a valve seat where the valve head rests when closed (28).

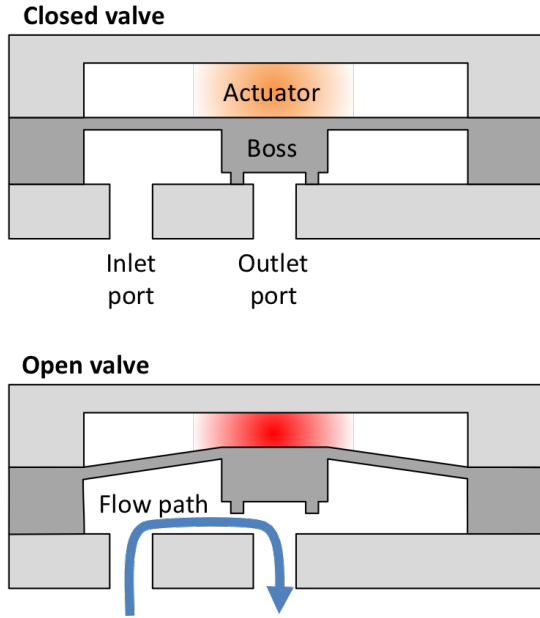


Fig. 4. A general schematic of a microvalve showing the flow path to be controlled and valve head moved by an actuator (Figure from (29)).

The valve head can be actuated by many ways- electrically, thermally, optically, or pneumatically. An in depth review of the various valve actuation mechanisms can be found in the literature(30, 31). In our survey (more details in Supp. Note 2) electrostatic, electromagnetic, piezoelectric and thermopneumatic valves have the fastest switching times in the sub millisecond domain and are of particular interest to our application.

Thermopneumatic valves (Fig.5) consist of a chamber with a deformable wall filled with a working fluid. The chamber includes a heater, which heats up the working fluid. The working fluid then expands, causing the flexible membrane to deform and seal the channel(30, 32, 33).

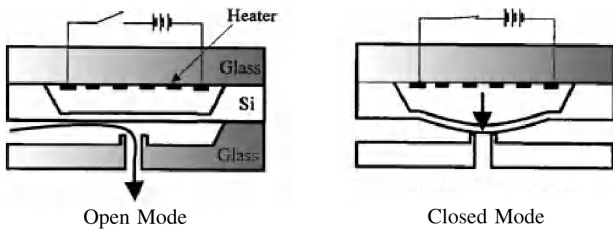


Fig. 5. A thermopneumatic valve (Figure from (33)).

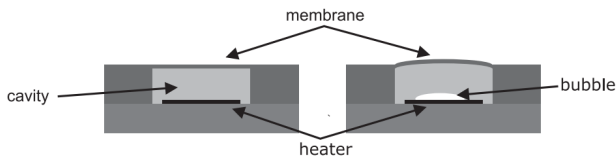
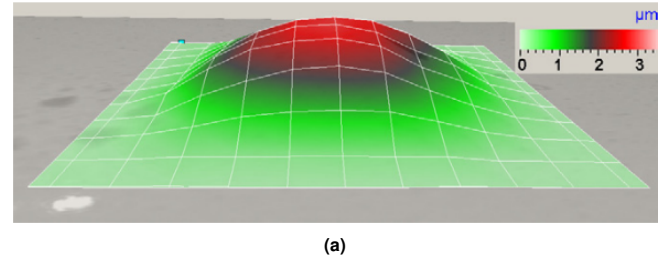


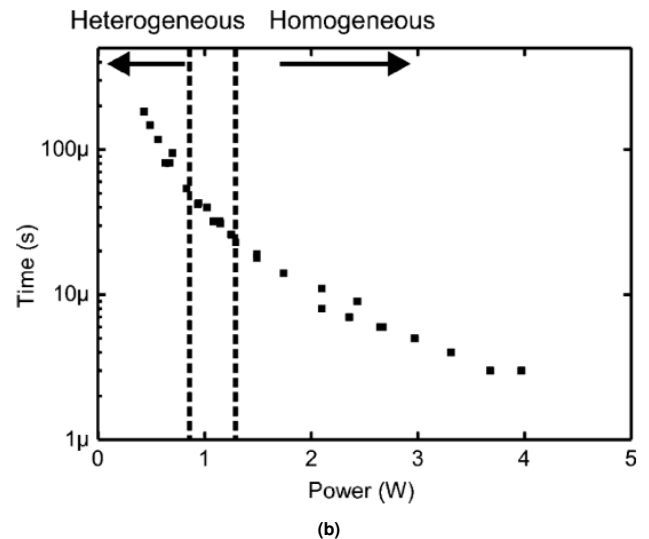
Fig. 6. Working principle of an explosive microbubble valve (Figure from (34)).

Thermopneumatic valves based on electric joule heating of the entire working fluid in the chamber have some inherent

inertia and are not suitable for sub millisecond switching applications. A variation on the thermopneumatic actuator is the explosive microbubble actuator as reported by Van den Broek and Elwenspoek. Here, sudden joule heating of a thin film of the liquid causes instantaneous nucleation of a bubble in the working fluid. The bubble also increases the volume of the working fluid chamber, deforming the membrane wall, sealing the channel (Fig. 6). Van den Broek and Elwenspoek reported a microbubble actuator which consisted of a $525\mu\text{m}$ deep cavity etched in silicon, a $1\mu\text{m}$ thick $250\mu\text{m} \times 250\mu\text{m}$ silicon nitride membrane, and a $50\mu\text{m} \times 250\mu\text{m}$ heater fabricated on a pyrex substrate. They reported a maximum deflection of the membrane to $3\mu\text{m}$ in $16\mu\text{s}$. Following the initial displacement, the membrane tends to oscillate around the mean position. They further estimated that the internal pressure for the membrane to be deflected to $3\mu\text{m}$ is 2 Bar. These parameters make this explosive microbubble actuator suitable for our use case. Van den Broek and Elwenspoek also measured the bubble nucleation time and mechanism with respect to applied power to the heater. In their work, Van den Broek and Elwenspoek investigated membrane sizes up to $1.5\text{mm} \times 1.5\text{mm}$ (Fig. 7(a)). They also measured the mode shapes on the membrane surface with respect to the frequency and the effect of heating power to the type of bubble nucleation (Fig. 7(b)).



(a)



(b)

Fig. 7. Main results from the work of van den Broek. (a) Surface scan of a $250\mu\text{m} \times 250\mu\text{m}$ membrane at peak displacement. (b) Effect of applied power and time on the type of bubble nucleation (Figures from (35)).

4. Device Schematic

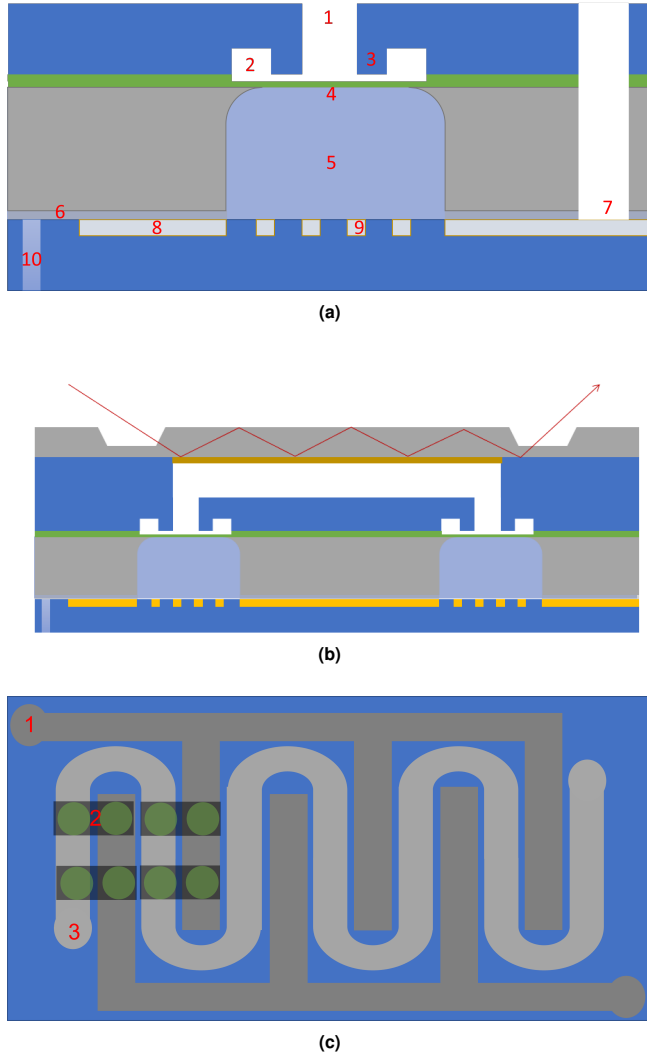


Fig. 8. (a) Schematic representation of side view of a single valve. (1) a cylindrical inlet/outlet connecting the reactor chamber to the main channels. (2) The main channels carrying gases to external gas source or exhaust (3) valve seat (4) flexible membrane (5) Chamber filled with working fluid, ethanol (6) channels connecting all the ethanol chambers together (7) access for electrical contacts (8) heat sink structures (9) heaters (10) access hole for filling in ethanol. (b) Schematic side view of a single reactor cell (1) ATR crystal with catalyst (2) reaction chamber (3) reactant inlet channel (4) product outlet channel. (c) Schematic top view of a chip showing the layers with (1) inlet and (3) outlet gas channels with (2) valves and reactor cells.

The valve controls the flow of gas from a main horizontal rectangular channel (Fig. 8(a)(2)) to a microreactor vertical circular sub-channel (Fig. 8(a)(1)). In the current chip design, an array (Fig. 8(c)) of such single reactor cells (Fig. 8(b), 8(c)(2)) that allow the flow of gas into (Fig. 8(b)(3)) and out of (Fig. 8(b)(4)) a microreactor chamber (Fig. 8(b)(2)) is designed. The ATR-IR crystal (Fig. 8(b)(1)) guides the light and enables ATR-IR measurements. Though some calculations have been made to justify the design choices, fabricating the gas flow channels and reactor chambers was considered to be outside the scope of this project.

The schematic of the valves along with the reactor chamber is indicated in Fig. 8(b). The thermopneumatic valve consists of a cavity in silicon filled with the working fluid,

ethanol (Fig. 8(a)(5)), a platinum on tantalum (Pt/Ta) embedded heater (Fig. 8(a)(9)) and a flexible Silicon rich Nitride ($SiRN$) membrane (Fig. 8(a)(4)). When the valve is closed, the membrane rests on a ring-like valve seat (Fig. 8(a)(3)). In addition to the (Pt/Ta) heat sink structures (Fig. 8(a)(8)) for cooling, each valve also has channels for the filling the cavity (Fig. 8(a)(6)) with the working fluid, ethanol.

On the chip level, accesses for the electrical interconnects (Fig. 8(a)(7)) as well as inlets for the ethanol to be filled in the channels (Fig. 8(a)(10)) are defined. The gas inlets (Fig. 8(c)(1)) follow a interdigitated design to minimize pressure drop, whereas the outlets follow a meandering path (Fig. 8(c)(3)).

5. Design Choices

The particular dimensions of the device were determined considering heuristics and scaling effects. Additionally Finite Element Method (FEM) and analytical simulations of the gas flow, in the main channels, membrane deflections, and heater power also affected the device dimensions.

5.1 Flow rates and hydraulic resistances. The gas flow towards and away from the reactor channel determines the dimensions of various components of the valve. To make multiple measurements as quickly as possible, it is important to not only minimize the switching time of the valve, but also to maximize the gas flow to fill and flush the reactor chamber. Pressure driven Poiseuille flow for fluids in rectangular channels is given by Equation 1, whereas in cylindrical channels it is given by Equation 2(36).

$$Q_R = \frac{4\mu l}{ab^3} \left[\frac{16}{3} - 3.36 \frac{b}{a} \left(1 - \frac{b^4}{12a^4} \right) \right]^{-1} \quad (1)$$

Here the height width and length of the channel are $2a, 2b$ and l respectively as in Fig. 26 (a) (in Supp. Note 3) and μ is the fluid viscosity in poiseuille.

$$Q_C = \frac{8\mu l}{\pi a^4} \quad (2)$$

Where the radius is a as in Fig. 26 (b) (in Supp. Note 3), and again l is the channel length, μ is the fluid viscosity in poiseuille.

An analogy can be made between fluid flow and electrical current flow as discussed in Supp. Note 3. Extending the electrical analogy further, the gas flow through the entire chip can be calculated by representing the gas fluidic network as an electrical network. An analysis of fluid flow by the electrical analogy is performed in Supp. Note 3. This analysis is based on the Kirchhoff matrix method for analyzing a ladder network as explained in the supplementary information of Odijk et al.

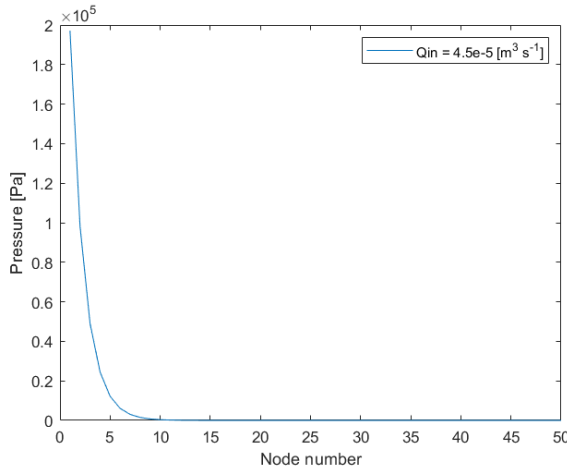


Fig. 9. Results from MATLAB script in Supp. Note 3 showing the pressure profile across the gas channel (Fig. 8(c)(3)). Each node represents a reactor cell along with its inlets and outlets.

Fig. 9 shows the general profile of the pressure inside the main supply channel 8(c)(3). We see that with an input flow rate of $4.5 \times 10^{-5} [m^3 s^{-1}]$, the inlet pressure is 2 Bar ($2 \times 10^{-5} [Pa]$) but drops to near zero by the 10th reactor. This exponential drop in pressure persists even if the number of cells is increased. To save computational resources, the conductance matrix and pressures were only calculated and plotted for a ladder network with 50 rungs. It was found that the flow rate drops to near zero by the 10th reactor independent of the input flow rate. This necessitates a parallel comb-like supply channel structure, instead of a series meandering supply channel.

5.2 Membrane dimensions and pressure.

5.2.1 Finite Element Method Simulations. The size, thickness, the pressure across the membrane, and material parameters of the membrane have an effect on the deflection profile and deflection speed. These factors, in turn affect the switching time, as well as the maximum radii of the gas inlets and outlets to be controlled.

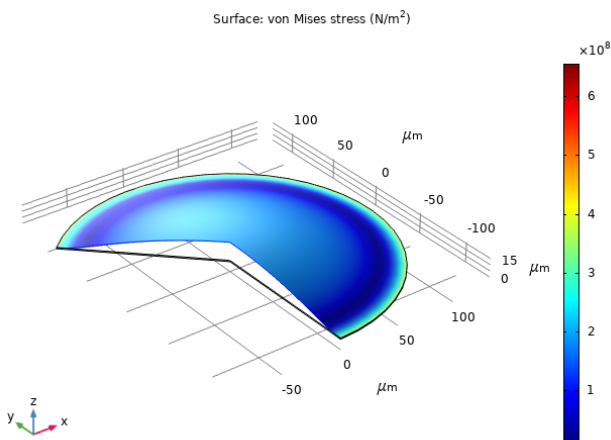


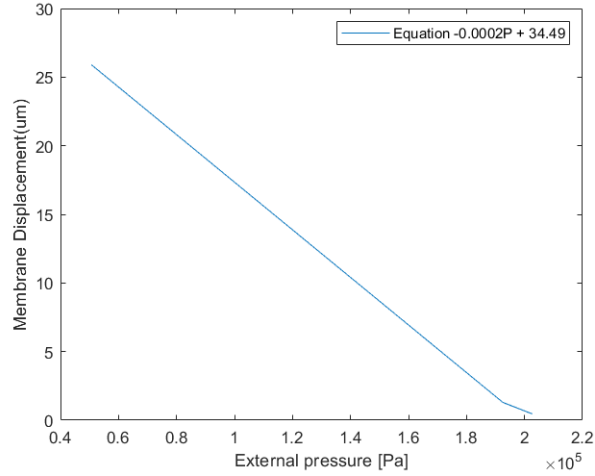
Fig. 10. COMSOL Model of Deformation on a $1 \mu m$ thick SiRN with an applied pressure of 2 Bar.

A model on COMSOL multiphysics was made to study the effect of these parameters. Stationary, time-dependent, and parametric sweep studies of the radius and applied pressure were conducted. The model consisted of a 2d axis symmetrical membrane with radius $125 \mu m$ and thickness of $1 \mu m$ with a maximum element size of $0.1 \mu m$. The default material properties for Silicon Nitride were chosen. The membrane was constrained on one edge, which corresponds to the circumference in the 3d object. An internal pressure of 2 Bar and an external pressure of 1 atm ($1.01325 \times 10^{-5} [Pa]$) was set for the stationary and time dependent studies.

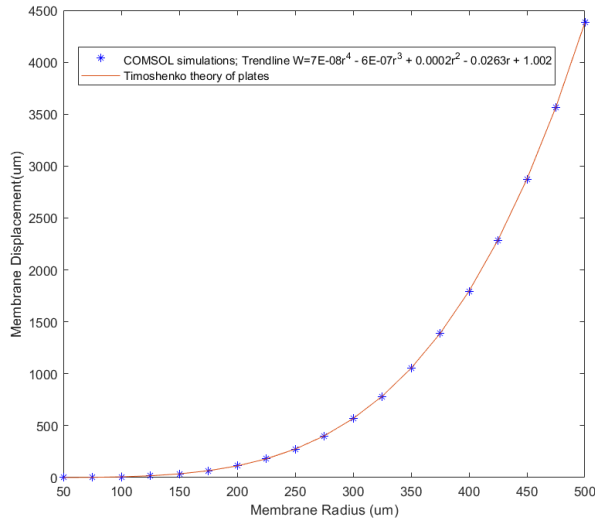
The stationary study result for the von Mises stress is shown in Fig. 10. The stress is highest on the clamped edges. The stationary study further indicated a maximum displacement of the centre of the membrane of $2.8847 \mu m$. This result was inconsistent with the parametric and time dependent sweeps and will be discussed later.

The time dependent study was conducted for $10 \mu s$ with a time step of $0.1 \mu s$. The time dependent study showed that the displacement of the centre of the membrane followed a damped sinusoidal pattern. The first peak corresponding to a maximum centre displacement of $34.226 \mu m$ was reached in $1.9 \mu s$ which fulfils our design criteria. It is assumed that if the membrane will contact the seat, the collision will be inelastic and the membrane will stay in place on the seat. Otherwise, at the cost of increasing device complexity, electrostatic actuation can be used in addition to the thermopneumatic actuation of the valve.

In the parametric studies, the maximum displacement was plotted against changes in the membrane radius and external pressure. The membrane radius was varied from 50 to $500 \mu m$ in steps of $25 \mu m$. It was found that the maximum displacement has a biquadratic dependence on the radius of the membrane as seen in Fig. 11(a). For the second sweep external pressure was varied from 0.5 to 2 atmosphere (atm) while the internal pressure was fixed at 2 Bar which is approximately equal to 2 atm. Fig. 11(b) shows that the maximum displacement has an inverse dependence on the pressure difference across the membrane. In both these parametric sweeps at an external pressure of 1 atm and a radius of $125 \mu m$ the maximum displacement of the membrane was $17.113 \mu m$.



(a)



(b)

Fig. 11. COMSOL simulation results of the effect on maximum displacement when sweeping the (a) external pressure, (b) membrane radius, superimposed upon the maximum displacement from the analytical model.

Furthermore, time dependent studies with varying initial radii and external pressures were conducted. The effect of these parameters on the time taken by the membrane to reach the first peak displacement was calculated. With all other factors constant, the external pressure has no effect on time taken to reach the maximum displacement, as seen in Table 1. On the other hand, increasing the radius of the membrane, increases the time taken to achieve maximum displacement as a cube as in Table 2.

5.2.2 Analytical Model of membrane deflection. The differences in the stationary and parametric study can be possibly explained by the different solution paths that the FEM software uses to minimize residuals and arrive at the results. In a parametric or time variant sweep, COMSOL uses the solution at the previous step as an input to solve the current parameter step(38).

To reconcile these differences between the stationary and parametric studies, an analytical model was used. The *SiRN* membrane was approximated as a plate with clamped edges. Using Timoshenko's theory of plates and shells(39), the maximum displacement was calculated to be $17.113\mu\text{m}$, agreeing with the results from parametric sweeps and time varying study. The Timoshenko theory results are plotted alongside the COMSOL results in Fig. 11(b). This analytical solution also confirmed the inverse dependence of maximum deflection on the pressure.

According to the Timoshenko theory, the maximum displacement at a point 'r' away from the centre of the membrane is given by:

$$W_{max,r} = \frac{q(a^2 - r^2)^2}{64D} \quad (3)$$

where q is the pressure difference across the membrane, a is the membrane radius. The flexural rigidity, D is given by:

$$D = \frac{Eh^3}{12(1 - \nu^2)} \quad (4)$$

Here E is the elastic modulus, h is the membrane thickness and ν is the Poisson's ratio.

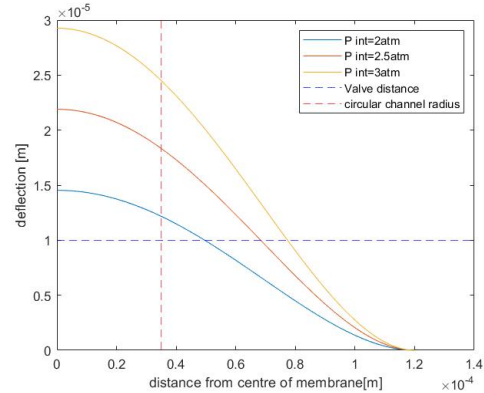


Fig. 12. Results of MATLAB script in Supp. Note 5 predicting membrane displacement at varying internal pressures and a radius of $125\mu\text{m}$. The intersection of the two dotted axes depicts the valve seat - the point where the membrane should contact in order to have a good seal.

A MATLAB script (Supp. Note 5) was written to plot the steady state profile of the membrane displacement at different internal pressures and radii using the above equation. It was found that for actuating a cylindrical channel of radius $35\mu\text{m}$ at a distance of $10\mu\text{m}$, a membrane of minimum radius $119\mu\text{m}$ would be required. Accounting for errors in the fabrication process we chose for a membrane size of $120\mu\text{m}$ as can be seen in Fig.12. The thickness of the membrane was chosen to be $1\mu\text{m}$ the same as the work of Van den Broek and Elwenspoek.

5.3 Parameters and Scaling effects. Using Equation 1, Equation 2, and Table 2 we can find the effect of the various parameters on switching speed and reactant gas flow rate.

Table 1. Effect of external pressure on maximum displacement and time taken by the membrane to reach it.

External Pressure [Bar]	First Displacement Peak [μm]	Time to first displacement peak [μs]
1	0.476	1.9
2	35	1.9
3	71.850	1.9
4	108.04	1.9

Table 2. Effect of membrane radius on maximum displacement and time taken by the membrane to reach it.

Membrane Radius [μm]	First Displacement Peak [μm]	Time to first displacement peak [μs]
62.5	2.1775	0.5
125	35	1.9
187.5	181.19	4.2
250	572.72	7.2

From Table 5 in Supp. Note 2 we can derive that the flow rate depends on the various parameters as:

$$Q \propto \frac{n P_{ext} B_r H_r^3 a_c^4}{L_r L_c} \quad (5)$$

where P_{ext} is the pressure outside the chamber driving the gas flow, H_r , B_r , and L_r are the height, breadth, and length of the rectangular inlet channel. a_c and L_c are the radius and length of the channel respectively, n is the number of inlets. H_{EtOH} and a_{EtOH} are the height and radius of the ethanol chamber.

The dimensions of the membrane (Fig. 8(a)(4)), horizontal main channels (Fig. 8(a)(2)), and vertical cylindrical channels (Fig. 8(a)(1)) determine the flow rate and switching speed.

6. Mask design and Device Fabrication

As seen in Fig. 8(a)(4-10), not including the valve seat, gas channels, or the reactor, the proposed device consists of two wafers bonded together anodically. The first is a Silicon wafer which contains a thin *SiRN* membrane on top, as well as chambers for ethanol, and accesses for electrical contact pads. The second is a MEMpax glass wafer, which contains platinum heaters, heat sink structures as well as inlets and outlets for the ethanol.

6.1 Etching multi-depth structures. Features at two different depths were to be fabricated in the silicon layer. The access for the electrical interconnects and membrane release at the chambers that hold the working fluid were to be etched to the complete depth of the wafer, $525 \mu m$. The channels interconnecting the chambers were to be etched to a shallower depth of approximately $60 \mu m$.

Recently, anisotropic Deep Reactive Ion Etching (DRIE) of grid structures followed by isotropic Vapour Phase Etching (VPE) has been reported for releasing MEMS structures of different footprints simultaneously by Zhao et al.

In this work, instead of using a traditional two mask process, a two step etch method, similar to the work of Zhao et al. was used. The Single-mask Pre-shape Assisted Multi-feature Structures (SPAMS) method in development by Haverkate et al. was used to define structures of different etch depths with a single mask. At first pre-shapes are defined using

DRIE (Fig. 13(b)). Unlike the sacrificial grid release technology used by Zhao et al., the areas etched by DRIE were of different size. The aspect ratio dependent etching (ARDE) property of DRIE allowed control over the etch depth of structures by controlling the exposed surface area of the pre-shapes.

After the pre-shapes have been defined, they are isotropically etched by Vapour Phase Etching (VPE) using XeF_2 . This isotropic VPE step connects pre-shapes to each other to form the final desired shapes (Fig. 13(c)).

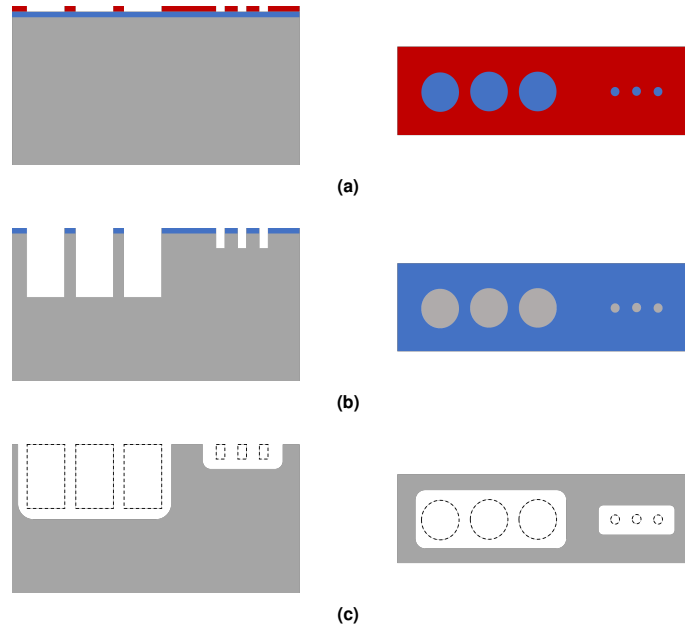


Fig. 13. Side and top view schematics of the wafer respectively showing (a) patterned photoresist (red) on hard mask (b) patterned hard mask (blue) followed by anisotropic etch (c) Post isotropic etch and hard mask removal step showing features at two different depths in silicon (grey). The dotted lines indicate the etch during the previous anisotropic etch step.

For the mask design, pre-shapes of two different radii were used to define the deeper and shallower features. The pitch, the maximum distance between two shapes of a kind, was constant. Assuming a perfectly isotropic etch by the vapor phase etching, and no local etch lag effects, both kinds of structures would connect to form the final features at different depths at the same time.

6.2 Mask Designs. Based on the design choices and process flow, three photomasks were designed using CleWin5. The masks were designed for metalization on the MEMpax layer, patterning of the silicon layer, and powder blasting access holes for ethanol in the MEMpax layer. Non-mirrored, inside-white masks were used for the Metalization and DRIE. A mirrored inside-black mask was used for the powder blasted ethanol inlets and outlets. The standard BIOS and MESA+ institute alignment markers by [van Nieuwkaas-teele](#) were included to be able to align the wafers to masks. The complete masks are presented in Supp. Note 4 and are made available online (43).

6.2.1 Metalization mask. The metalization layer consists of electrodes and heaters in the ethanol chamber, as well as heat sink structures on both sides of the ethanol chamber to cool the working fluid quickly.

Each of the individual valves had 5 parallel traces. Each of these parallel traces had 4 pinched sections in series that acted as microheaters (Fig. 14(a)). The resistance of the pinched and broader sections were the same, as calculated in Supp. Note 6. However, due to the smaller area of the pinched section, the heat flux at the pinched sections was higher.

Each $120\mu\text{m}$ radius valve had 20 heaters which could be turned on 4 at a time. The heaters would completely overlap with the ethanol chamber of radius $120\mu\text{m}$ but the first and last rows of heaters would fall just outside the $90\mu\text{m}$ radius chamber. Multiple microheaters increase the probability of bubble nucleation. Additionally, multiple microheaters allow a higher heat flux into the working fluid than a single microheater with the same applied potential. The parallel traces also allow for discrete control of the heat flux into a single ethanol chamber.

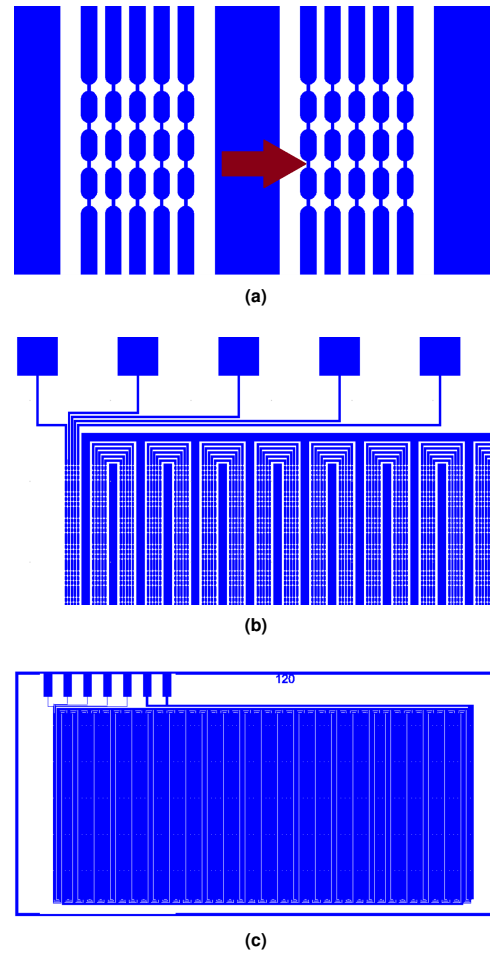


Fig. 14. (a) An enlarged view of two sets of heaters with 5 parallel traces each separated by cooling structures. The red arrow highlights a single 'pinched section' heater. (b) An enlarged view of a main chip showing how the first five traces connect to the meandering groups of heaters. (c) A main chip with 7 connector pads, 5 as sources for the heaters and 2 for the ground contact. The chip also contains cooling structures, a border for the dicing saw to follow and text indicating the valve radius.

The traces were connected to contact pads to be interfaced with spring loaded connectors or probes (Fig. 14(b)). At the last valve, the 5 parallel traces connected to a thicker ground trace. The ground trace had one fifth the resistance as compared to each of the five supply traces with heaters. The ground trace also terminated into two contact pads instead of one. The second ground trace and contact pad acted as a contingency or backup trace in case of adhesion issues due to high current and heat.

The heater traces followed a meandering path across the chip, connecting all 2808 individual valves on both the $90\mu\text{m}$ membrane radius and $120\mu\text{m}$ membrane radius main chips. On the other hand, the heat sink traces formed an interdigitated comb like structure. (Fig. 14(b,c))

To keep all features at the same potential during the anodic bonding process, each chip was surrounded by a metalized border between chips that tied the contact pads of the five heaters and two ground traces. The heat sink traces were also connected to ground.

The metalization border around each chip also provided a visual aid for aligning the path to be followed by the dicing saw after wafer bonding (Fig. 14(c)). The border was $300\mu\text{m}$

thick to account for the thickness of the dicing saw. At the areas connecting the contact pads to each other, the thickness of the metallic traces was reduced to $200\mu m$ so that even in case of alignment errors with the dicing saw, the contact pads no longer remain connected to each other after dicing.

Each main chip was given an identification number specifying the row and column so that its position on the wafer is known, in case of inconsistencies in the fabrication process or device performance. Similarly, the test chips were also given an alphanumeric code to identify their position on the wafer.

In addition to these chip level features, two flash zones were also defined on the wafer that were disconnected from all other functional structures like heaters, traces and contact pads. Electrical breakdown during the anodic bonding of MEMpax and silicon wafers would be more likely at these flash zones than at the structures on chip, hence protecting the structures. The complete photomask design highlighting all the features is presented in Supp. Note 4.

6.2.2 Powder Blasting Mask. The powder blast mask defined the inlets and outlets of the ethanol channels on the MEMpax glass wafer.

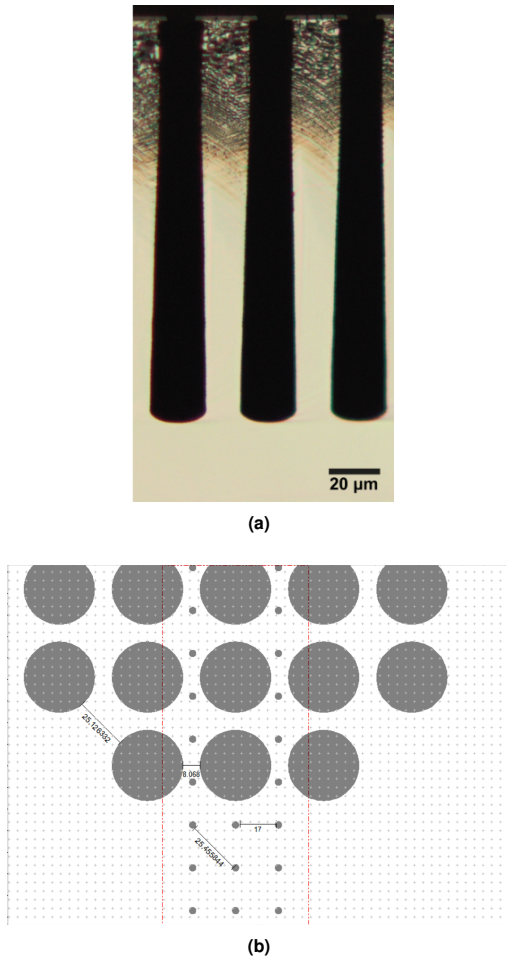


Fig. 15. (a) Image of DRIE profile from the work of [Haverkate et al.](#) (unpublished) based on which the pre-shape radii for this work were calculated (b) DRIE Mask showing pre-shapes of radii $1.5625\mu m$ and $16.40625\mu m$ with a maximum pitch of $25\mu m$.

6.2.3 Silicon etch mask. From partial results of [Haverkate et al.](#) (unpublished), circular structures were chosen as the pre-shapes. From Fig. 15 (a) it was estimated that for SPAMS pre-shapes with a pitch of $25\mu m$ and radius of $5\mu m$, a depth of $155\mu m$ is achieved. It was assumed that for the same settings for DRIE, the aspect ratio would be approximately the same. Therefore for the shallow channels pre-shapes of radius $1.5625\mu m$ were chosen. Whereas for the deeper chambers (Fig. 8(a)(5)) and the electrical access (Fig. 8(a)(7)), pre-shapes of radius $16.40625\mu m$ were chosen. These would lead to calculated etch depths of approximately $48.5\mu m$ and $508.5\mu m$ respectively. The pitch was maintained at $25\mu m$ for both shallow and deeper structures. This is shown in Fig. 15(b). After DRIE of these pre-shapes, VPE would be used to interconnect pre-shapes to form the final channels, chambers and electrical accesses. It is assumed that VPE would etch $12.5\mu m$ isotropically leaving us with channels of depth $60\mu m$ and chambers of depth $520\mu m$.

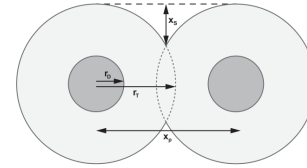


Fig. 16. Roughness induced on sidewalls perpendicular to the wafer due to connecting pre-shapes. Figure from unpublished work of [Haverkate et al.](#)

In the features formed by SPAMS, the channel sidewalls are not completely smooth perpendicular to wafer (Fig. 16). The surface roughness is due to pre-shapes connecting in the VPE step. For circular pre-shapes, sidewall roughness is given by the following equation by [Haverkate et al.](#):

$$x_s = r_t - \sqrt{r_t^2 - \frac{x_p^2}{4}} \quad (6)$$

where x_s is the amplitude of roughness of the channel walls r_t is the radius of the etched circle after VPE and x_p is the pitch between pre-shapes.

In our case this roughness calculated in Table 3

The main chips with 2808 valves each had an ethanol chamber radius of either 90 or $120\mu m$. The test chips with only one valve had ethanol chamber radii of 60 , 90 , 120 , and $150\mu m$.

7. Process flow and fabrication

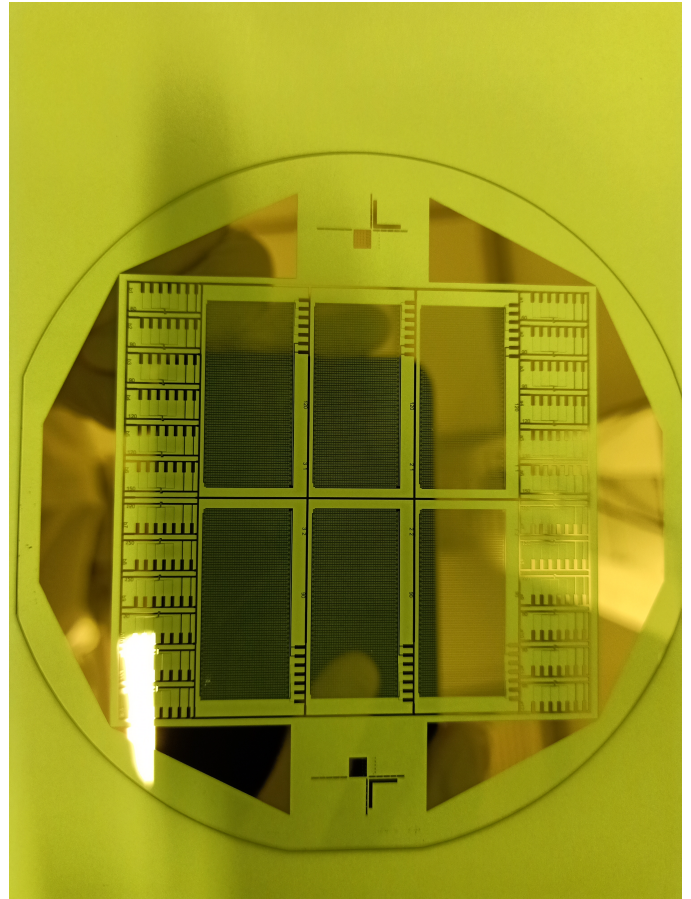
This section outlines the process flow followed in the cleanroom to fabricate the microvalves. The processing of these microvalves include many challenges such as through hole etching, multi depth structures, and isotropic etching for membrane release. The optimization of this process flow, as well as a detailed process flow is presented in Supp. Note 8. A schematic of the process flow is also presented in Fig. 49 and 50 in Supp. Note 8.

7.1 The MEMpax Wafer. A $500\mu m$ thick, $100mm$ diameter MEMpax wafer was cleaned and spincoated with Olin

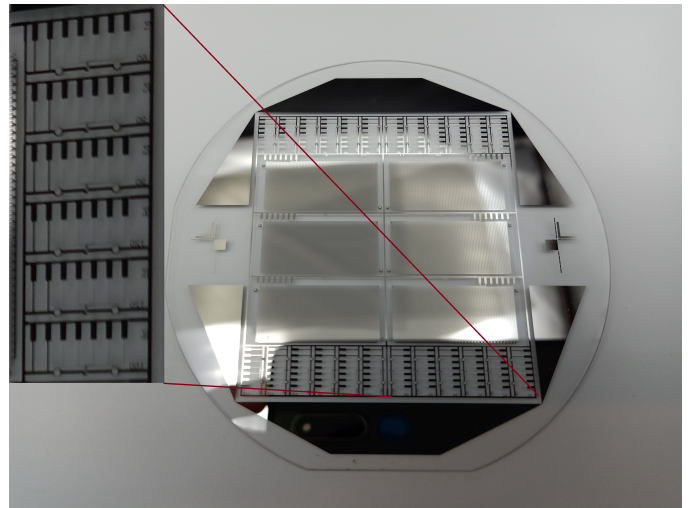
Table 3. Effect of pre-shape radius on sidewall roughness in the direction perpendicular to the wafer. All values are in μm .

Target feature Depth	Pre-shape radius (r_d)	Pre-shape Pitch(x_p)	Calculated post-VPE radius(r_T)	Calculated post-VPE roughness(x_s)
60	1.5625	25	14.0625	7.6201
520	16.40625	25	28.5625	2.8805

Oir 907-17 positive photoresist on the bottom side of the wafer after vapour phase priming with Hexamethyldisilazane (HMDS). The resist was patterned using a standard lithography process. The MEMPax wafer was etched according to the resist pattern in Buffered Hydrofluoric acid (BHF) to a depth of about 160nm. The etch depth was confirmed using the Veeco Dektak 8 surface profiler.



(a)

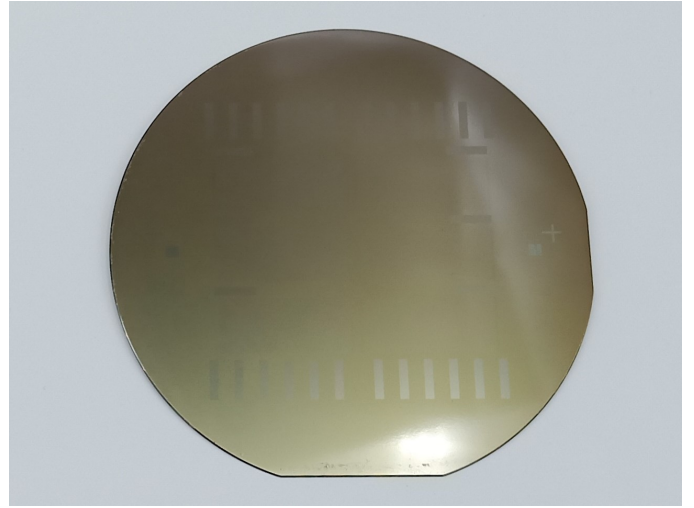


(b)

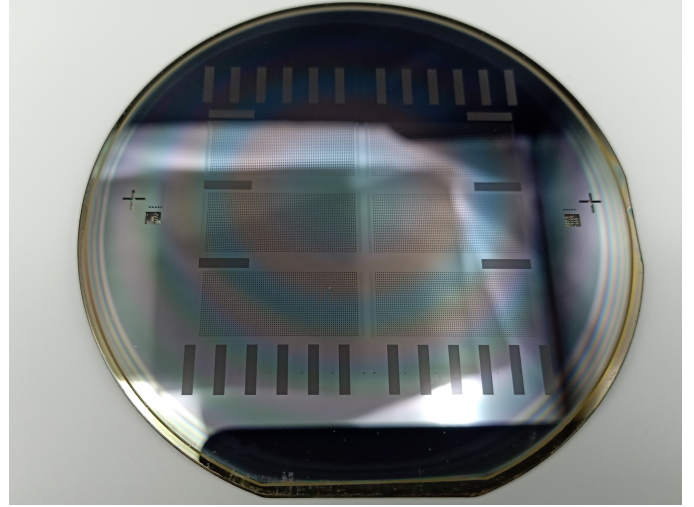
Fig. 17. (a) The MEMpax glass wafer with 6 main chips and 16 test chips on the side, all surrounded by 'flash zones' for anodic bonding. (b) Final MEMpax wafer with powderblasted holes. Inset: an enlarged view highlighting the location of inlet and outlet powderblasted holes on test chips and one of the main chips.

Following the etch, 10nm of Tantalum(Ta) for adhesion and

150nm of Platinum(*Pt*) was sputtered on the wafer using the T'COathy Sputtering system on the bottom face of the wafer. Next, the photoresist was removed to complete the liftoff process. The result can be seen in in Fig.17 (a). An Ordyl dry film resist was applied to the top side of the wafer. It was exposed via the powder blast photomask using the EVG 620 mask aligner and developed using hot water. Finally, inlet and outlet holes for ethanol channels were made by powder blasting with Al_2O_3 grains from Imersys Fused Minerals. The developed dry film resist is removed using a 1% solution of $NaHCO_3$ and the wafers were cleaned to remove particle and organic contaminants. Fig. 17(b) shows the wafer with powder blasted holes.



(a)



(b)

Fig. 18. Photographic images of the wafer after (a) RIE of the hard mask layer (b) DRIE of the bulk silicon under the hard mask layer.

7.2 The Si wafer. A $525\mu m$ thick, 100mm diameter, P++ Boron doped wafer was wet oxidized to grow a $2\mu m$ layer of Silicon dioxide (SiO_2). Nitto dicing foil was applied to protect the SiO_2 at the top. The SiO_2 on top was etched using Buffered Hydrofluoric acid (*BHF*). The dicing foil was removed from the bottom side and a $1\mu m$ thick layer of Silicon rich Nitride(*SiRN*) was grown on both sides by Low Pressure Chemical Vapour Deposition (LPCVD). Next, the top side of the wafer was coated with the Olin Oir 908-35 resist. It was exposed via the photomask and developed, defining the pre-shapes in photoresist. Following the patterning of photoresist, the SiO_2 and *SiRN* hard mask layer was patterned by RIE etching. Using the SiO_2 and *SiRN* layer as a hard mask, DRIE was used to form pre-shapes in silicon by transferring the pattern from the hard mask to the silicon.

Oxygen plasma and piranha cleaning were used to remove passivating fluorocarbons left on sidewalls from the DRIE process. Once the fluorocarbons were removed, a thin uniform layer of native silicon dioxide formed spontaneously on the sidewalls. The wafer was diced into chips and vapour phase etching with XeF_2 was used. This vapour phase etching step connected the pre-shapes to form the final ethanol chamber and channels, as well as released the membrane in the contact pad region.

8. Results and discussion

8.1 Optimization of the process flow in MEMpax. After photolithography, the MEMpax wafers were etched in *BHF* for 7 minutes to form trenches for the heaters. The estimated etch rate was 20-25nm/minute. At 200W sputter power tantalum was deposited for 1 minute followed by 6 minutes and 30 seconds of platinum. The profile was measured by the Dektak profilometer. The next samples were processed with an addition 10s of deposition with platinum. The

profile was measured again and now the metal was level with the MEMpax.

8.2 Optimization of the process flow in silicon. The SPAMS process has to be optimized for each new mask design. Due to time constraints and fabrication challenges, no working chips were fabricated. However, as a proof of concept, we were able to fabricate multi depth features using a single mask. The ethanol channels were etched to a depth of $450\mu m$ whereas the contact pad area was etched to $525\mu m$ and achieved membrane release. The ethanol chamber was etched to an intermediate depth between $450\mu m$ and $525\mu m$ but could not be measured.

A short summary of the optimization process is presented in the next section. A detailed overview of overcoming these challenges can be found in Supp. Note 8.

As shown in Supp. Note 4, the pre-shape mask was feature dense and consisted of a lot of small details. For the complete wafer, the initial exposed surface area was as high as $3.1273cm^2$. This presented a number of challenges during the fabrication process as listed below.

8.2.1 Photolithography. The photoresist used for defining the features on the hard mask was Olin Oir 907-35. This produced a relatively thick $3.5\mu m$ film on the wafer. In addition to this, the radius of the smaller pre-shapes was $1.5625\mu m$. A combination of small feature size and high film thickness meant that the photolithographic exposure dose had to be optimized to prevent underexposed features. This was done by means of increasing the dose time to 12s.

8.2.2 Patterning the hard mask. After the photolithography step, the pre-shapes were to be defined using RIE in the hard mask layer consisting of silicon nitride and silicon dioxide (Fig. 18(a)). We found that processing 4 wafers concurrently in the Plasma-therm 790 was inefficient. Our application has a high exposed surface area of silicon. This high surface area in turn limits the etch rate of silicon. This decrease in the etch rate due to a large exposed surface area is known as the loading effect. We found it more time efficient to process the wafers individually sequentially in the Adixen RIE system as this reduced the loading.

8.2.3 Etching the pre-shapes. DRIE was to be used to etch pre-shapes to the depths of 508.5 and $47.5\mu m$. This was a challenge with the current mask design due to the size and density of the pre-shapes. The first challenge with DRIE was the etch uniformity. The features at the centre got etched faster than the features on the edges of the wafer. The second challenge was poor etch selectivity. This meant that the hard mask would be etched away before the pre-shapes reached the required depths.

Multiple etch recipes were tried to solve these issues where parameters like the substrate temperatures, gas flow rates, cycle times, process pressures, platen, and plasma power were varied. The effects of varying these parameters are explored further in Supp. Note 8.

In the end, a standard $0^\circ C$ etch recipe was used for 45 minutes to still have $144nm$ of remaining hard mask (Fig. 18(b)).

However the pre-shape depths were 413 and $154\mu m$ and not as desired. While the larger pre-shapes were not deep enough, the smaller pre-shapes were etched deeper than expected the inverse etch lag regime was approached(44).

8.2.4 Vapour phase etching. The final step of the SPAMS process is to connect the pre-shapes defined in the previous DRIE step by vapour phase etching (VPE). At first a 2 Torr XeF_2 recipe was used. However this recipe was very slow and did not connect the pre-shapes even after 200 etch cycles of 30s each. Next a SF_6 plasma etch was used. Here, the etch rate was much faster and the contact pad region defined by the bigger pre-shapes etched till the $SiRN$ membrane but the smaller pre-shapes on the edges of the wafer did not interconnect. Hence, to get rid of the non-uniformity, we again switched back to a XeF_2 process, but this time with shorter pulses and a higher processing pressure.

Test chips of $1.5cm \times 0.5cm$ with a single channel and reservoir were fixed to a oxide coated carrier wafer using photoresist. The outside edges of the chips were painted with photoresist to prevent etching at the edges. These individual chips had a low loading with an initial exposed surface area of $0.0756cm^2$. The test chips were processed for 130-140 cycles of XeF_2 VPE at 3 Torr with each cycle lasting 15 seconds. The end result was that the silicon nitride membrane was released at the channel contact pad regions, however, the etch depths and membrane release at the chamber could not be confirmed by non-destructive optical methods without cleaving the chip. The SiO_2 hard mask layer was removed by placing the affixed sample and wafer in BHF for 15 minutes. The resulting chip is shown in Fig. 19. The cross section images can be found in Fig. 48 in Supp. note 8.

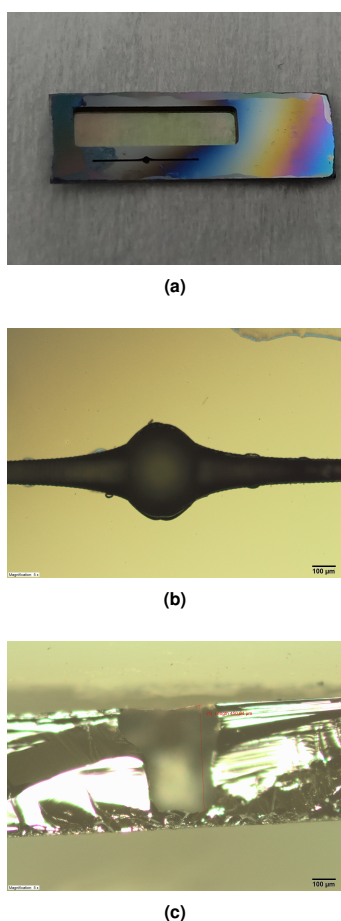


Fig. 19. (a) Photographic image of a single test chip with the silicon nitride membrane released at the contact pad area, and a horizontal micro-channel with a chamber in the middle. (b) Microscopy image of the chamber and test channel with the top hard mask layer removed. (c) Cross section of the chip showing a channel of depth of $450\mu m$.

8.3 The driving circuit. Heating the ethanol and operating the valves requires an input of electrical energy into the system. The ethanol in the chambers must be heated beyond the critical temperature to cause spontaneous nucleation of a bubble(34, 45).

Assuming only conductive heat transfer when the liquid is initially at rest, the heat flux from the heater can be calculated by using the electrical analogy of heat transfer. The thermal circuit is represented by Fig. 20.

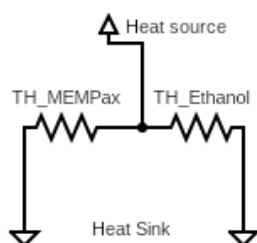


Fig. 20. Thermal circuit following the electrical analogy of heat flow.

Obtaining the power from the heater and knowing the dimensions and resistivity of the traces, we can calculate the poten-

tials and currents to be applied. To calculate the resistances, thin film resistivity values from the work of Tiggelaar were used as the thin film resistivity differs from bulk material resistivity.

It was calculated that for the smaller test chips with a single valve, a potential of 33.45V is required to initiate nucleation of the bubble at the trace with 4 heaters in series for an electric pulse of $10\mu s$. Further details about these calculations can be found in Supp. Note. 6. Increasing the pulse width would in turn lower the potential required. However it would also affect the switching speed of the valve. A microcontroller-based circuit was proposed to operate the valve in Supp. Note 7. Using a lab power supply and a MOSFET, the energy input into the heater trace could be controlled. This circuit also produced a $10\mu s$ trigger signal for a high speed camera to study the bubble nucleation dynamics of the valve.

9. Conclusions

Microreactors with integrated optics are suitable platforms for studying electrochemical reduction of CO_2 . To make use of the recent improvements in IR spectroscopy for studying short lived intermediate products, it is essential to precisely and swiftly control the flow of reactant and product gases. A design cycle was executed to fabricate such valves. A study of the various valve actuating mechanisms in literature revealed that a thermopneumatic bubble actuator would be most suitable for this purpose. FEM simulations, analytical models, and heuristics were used to make the design choices for an array of such valves. A novel process was attempted to be optimized to fabricate these valves. Multi depth structures were fabricated using a single mask design. However, further optimization of the mask design and process flows are required to produce functioning valves. The heat flow before bubble nucleation was modelled and the required potentials for spontaneous nucleation were calculated. A control circuit for the valves was proposed.

10. Recommendations

To solve the fabrication challenges in the silicon substrate, a mask design with lower loading can be used in the future. Furthermore, characterization runs or simulations are needed to study the effect of aspect ratios in masks with a higher loading. Subsequent redesign of the mask with pre-shapes would be required. A thinner substrate could also have been used to achieve membrane release with the same hard mask layer and DRIE techniques. A two mask process with KOH etching can also be used, but brings it's own set of challenges with monitoring the end point of the etch. To further improve the switching characteristics of the valve at the cost of increasing fabrication complexity, a corrugated instead of a planar $SiRN$ membrane can be used. The valving mechanism can also be combined with an electrostatic actuation mechanism but this would further complicate the control circuitry of the valve.

ACKNOWLEDGEMENTS

References

- Mishra
- et al.*
- | Ultrafast expanding microbubble valve array

- Spring" Model. <https://www.masterorganicchemistry.com/2016/11/11/bond-vibrations-ir-spectroscopy/>.
52. Shuo Cui, Radwan Chahal, Catherine Boussard-Plédel, Virginie Nazabal, Jean Louis Doualan, Johann Troles, Jacques Lucas, and Bruno Bureau. From selenium- to tellurium-based glass optical fibers for infrared spectroscopies. *Molecules*, 18(5):5373–5388, may 2013. ISSN 14203049. doi: 10.3390/molecules18055373.
 53. M. Carmen Estevez, Mar Alvarez, and Laura M. Lechuga. Integrated optical devices for lab-on-a-chip biosensing applications. *Laser and Photonics Reviews*, 6(4):463–487, jul 2012. ISSN 18638880. doi: 10.1002/lpor.201100025.
 54. Jean Michel Andanson and Alfons Baiker. Exploring catalytic solid/liquid interfaces by in situ attenuated total reflection infrared spectroscopy. *Chemical Society Reviews*, 39(12):4571–4584, nov 2010. ISSN 14604744. doi: 10.1039/b919544k.
 55. Miles J. Weida and Brandon Yee. Quantum cascade laser-based replacement for FTIR microscopy. *Imaging, Manipulation, and Analysis of Biomolecules, Cells, and Tissues IX*, 7902(February 2011):79021C, 2011. ISSN 1605-7422. doi: 10.1117/12.873954.
 56. Byunghoon Bae, Junghoon Yeom, Adarsh D. Radadia, Richard I. Masel, and Mark A. Shannon. A fully-integrated MEMS preconcentrator for rapid gas sampling. *TRANSDUCERS and EUROSENSORS '07 - 4th International Conference on Solid-State Sensors, Actuators and Microsystems*, 46(3):1497–1500, 2007. ISSN 1340-2625. doi: 10.1109/SENSOR.2007.4300428.
 57. Byunghoon Bae, Jaehyeong Han, Richard I. Masel, and Mark A. Shannon. A bidirectional electrostatic microvalve with microsecond switching performance. *Journal of Microelectromechanical Systems*, 16(6):1461–1471, dec 2007. ISSN 10577157. doi: 10.1109/JMEMS.2007.907782.
 58. Janet K. Robertson and Kensall D. Wise. A low pressure micromachined flow modulator. *Sensors and Actuators, A: Physical*, 71(1-2):98–106, nov 1998. ISSN 09244247. doi: 10.1016/S0924-4247(98)00160-5.
 59. Dieter Bosch, Bianca B. Heimhofer, G. Mück, Helmut Seidel, U. Thumser, and Wolfgang Welsler. A silicon microvalve with combined electromagnetic/electrostatic actuation. *Sensors and Actuators: A: Physical*, 37-38(C):684–692, jun 1993. ISSN 09244247. doi: 10.1016/0924-4247(93)80116-X.
 60. Jong M. Park, Allan T. Evans, Kristian Rasmussen, Tyler R. Brosten, Gregory F. Nellis, Sanford A. Klein, and Yogesh B. Gianchandani. A microvalve with integrated sensors and customizable normal state for low-temperature operation. *Journal of Microelectromechanical Systems*, 18(4):868–877, 2009. ISSN 10577157. doi: 10.1109/JMEMS.2009.2021097.
 61. Peige Shao, Zeno Rummeler, and Werner Karl Schomburg. Polymer micro piezo valve with a small dead volume. *Journal of Micromechanics and Microengineering*, 14(2):305–309, feb 2004. ISSN 09601317. doi: 10.1088/0960-1317/14/2/020.
 62. Philippe Dubois, Benedikt Guldman, and Nico F. de Rooij. High-speed electrostatic gas microvalve switching behavior. *Microfluidics and BioMEMS*, 4560(September 2001):217–226, 2001. doi: 10.1117/12.443061.
 63. COMSOL. What Is Piezoelectricity? | COMSOL Blog. <https://www.comsol.com/blogs/what-is-piezoelectricity/>.
 64. Kwang W. Oh, Kangsun Lee, Byungwook Ahn, and Edward P. Furlani. Design of pressure-driven microfluidic networks using electric circuit analogy. *Lab on a Chip*, 12(3):515–545, feb 2012. ISSN 14730189. doi: 10.1039/c2lc20799k.
 65. Henrik Bruus. *Theoretical Microfluidics*. Oxford University Press, 2008. ISBN 978-0-19-923509-4.
 66. National institute of standards and technology US department of Commerce. Ethanol. <https://webbook.nist.gov/cgi/cbook.cgi?ID=C64175&Type=TC#TC>.
 67. Michael S. Gerlt, Nino F. Läubli, Michel Manser, Bradley J. Nelson, and Jürg Dual. Reduced etch lag and high aspect ratios by deep reactive ion etching (DRIE). *Micromachines*, 12(5):1–8, 2021. ISSN 2072666X. doi: 10.3390/mi12050542.
 68. CJD Craigie, T Sheehan, VN Johnson, SL Burkett, Amy J Moll, and WB Knowlton. Polymer thickness effects on bosch etch profiles. *Journal of Vacuum Science & Technology B: Microelectronics and Nanometer Structures Processing, Measurement, and Phenomena*, 20(6):2229–2232, 2002. doi: 10.1116/1.1515910.
 69. René Wolf, Henk-Willem Veltkamp, and Meint de Boer. SPTS Pegasus – Si Etch - -19 Deg - Etch Process document, 2018. [https://mesaplusnanolab.ewi.utwente.nl/mis/generalinfo/downloads/usermanuals/268/Processsheet-SPTS-SietchSTD\[etch212\]sept2018.pdf](https://mesaplusnanolab.ewi.utwente.nl/mis/generalinfo/downloads/usermanuals/268/Processsheet-SPTS-SietchSTD[etch212]sept2018.pdf).
 70. René Wolf, Henk-Willem Veltkamp, and Meint de Boer. SPTS Pegasus - HARS - Etch218 Process document, 2018. [https://mesaplusnanolab.ewi.utwente.nl/mis/generalinfo/downloads/usermanuals/268/Processsheet-SPTS-Hars\[etch218\]sept2018.pdf](https://mesaplusnanolab.ewi.utwente.nl/mis/generalinfo/downloads/usermanuals/268/Processsheet-SPTS-Hars[etch218]sept2018.pdf).
 71. Tsengyou Syau, B. Jayant Baliga, and Raymond W. Hamaker. Reactive Ion Etching of Silicon Trenches Using SF₆ / O₂ Gas Mixtures. *Journal of The Electrochemical Society*, 138(10):3076–3081, 1991. ISSN 0013-4651. doi: 10.1149/1.2085371.
 72. C. J. Mogab, A. C. Adams, and D. L. Flamm. Plasma etching of Si and SiO₂ - The effect of oxygen additions to CF₄ plasmas. *Journal of Applied Physics*, 49(7):3796–3803, aug 1978. ISSN 00218979. doi: 10.1063/1.325382.
 73. Onno W. Purbo, C. R. Selvakumar, and Durgamadhhab Misra. Reactive Ion Etching of SOI (SIMOX and ZMR) Silicon in Nitrogen Containing CF₄ + O₂ and SF₆ + O₂ Plasmas. *Journal of The Electrochemical Society*, 140(9):2659–2668, 1993. ISSN 0013-4651. doi: 10.1149/1.2220882.
 74. Reza Abdolvand and Farrokh Ayazi. An advanced reactive ion etching process for very high aspect-ratio sub-micron wide trenches in silicon. *Sensors and Actuators, A: Physical*, 144(1):109–116, may 2008. ISSN 09244247. doi: 10.1016/j.sna.2007.12.026.
 75. Henri Jansen, Han Gardeniers, Meint De Boer, Miko Elwenspoek, and Jan Fluitman. A survey on the reactive ion etching of silicon in microtechnology. *Journal of Micromechanics and Microengineering*, 6(1):14–28, 1996. ISSN 09601317. doi: 10.1088/0960-1317/6/1/002.
 76. G. Cunge and Jean-Paul Booth. CF₂ production and loss mechanisms in fluorocarbon discharges: Fluorine-poor conditions and polymerization. *Journal of Applied Physics*, 85(8):3952–3959, 1999. ISSN 10897550. doi: 10.1063/1.370296.
 77. Pierre-Baptiste Vigneron, Francois Joint, N. Isac, R. Colombelli, and E. Herth. Advanced and reliable GaAs/AlGaAs ICP-DRIE etching for optoelectronic, microelectronic and microsystem applications. *Microelectronic Engineering*, 202:42–50, 2018. ISSN 01679317. doi: 10.1016/j.mee.2018.09.001.
 78. Henri V. Jansen, Meint J. De Boer, S. Unnikrishnan, M. C. Louwerse, and Miko C. Elwenspoek. Black silicon method X: A review on high speed and selective plasma etching of silicon with profile control: An in-depth comparison between Bosch and cryostat DRIE processes as a roadmap to next generation equipment. *Journal of Micromechanics and Microengineering*, 19(3), 2009. ISSN 09601317. doi: 10.1088/0960-1317/19/3/033001.
 79. Birck Nanotechnology center. STS Advanced Silicon Etch DRIE HRM System Trends, 2007. https://www.purdue.edu/discoverypark/birck/files/STS_ASE_DRIE_Trends.pdf.
 80. Henri Jansen, Meint de Boer, Johannes Burger, Rob Legtenberg, and Miko Elwenspoek. The black silicon method II: The effect of mask material and loading on the reactive ion etching of deep silicon trenches. *Microelectronic Engineering*, 27(1-4):475–480, 1995. ISSN 01679317. doi: 10.1016/0167-9317(94)00149-O.
 81. René Wolf, Henk-Willem Veltkamp, and Meint de Boer. SPTS Pegasus - DRIE of Silicon - Isotropic - Etch213, 2018. https://mesaplusnanolab.ewi.utwente.nl/mis/include/rcp_show.php?rcptn_headerID=460.

Supplementary Note 1: Catalysis and Spectroscopy

A. Catalysis. Although catalysts do not shift the equilibrium of a reaction, like artificial photosynthesis, they speed up reaction rates by lowering the energy barrier for a reaction to proceed(47). The artificial photosynthesis process consists of five main steps: light absorption, charge separation, migration, recombination and redox reactions(48).

Catalysts help make the reactions more efficient by providing alternative possible reaction pathways. Knowing these possible reaction pathways, their kinetics and intermediate products would help gain insights in designing better catalysts(47, 49). Fig. 21 shows the energy vs reaction coordinate diagram of a catalyzed reaction with intermediate products and an uncatalyzed reaction.

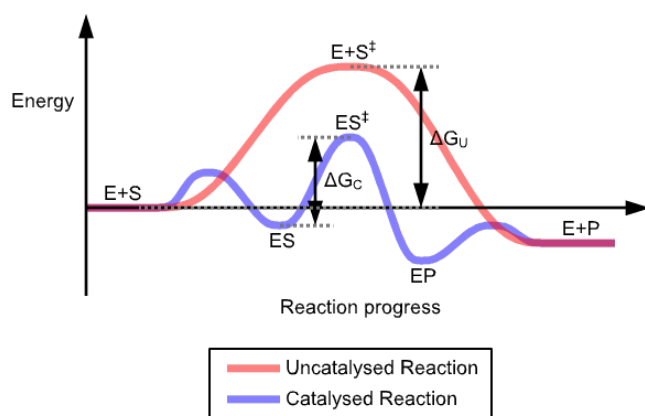


Fig. 21. Energy vs reaction coordinate for a catalysed and uncatalysed reaction. In a catalyzed reaction, intermediate products ES, ES[‡] and EP are formed (Figure from (50)).

B. Absorbance Spectroscopy and ATR-IR. In absorbance spectroscopy, incident electromagnetic radiation interacts with matter and gives us information about bond and atomic vibrations or crystal structure(51). Infrared spectroscopy is a type of absorbance spectroscopy where infrared light is incident on a sample and specific frequencies of the light are absorbed by the sample. The absorbed light corresponds to the vibrational frequencies of the sample molecule's bonds and can identify the sample composition and structure(25).

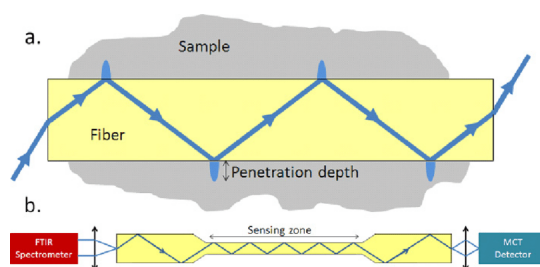


Fig. 22. Light being coupled into a waveguide. Evanescent waves being formed at the interfaces penetrating into the sample. Changes in the composition of the sample within the penetration depth changes the effective refractive index of the sample medium which is measured as a phase change by the detector (Figure from (52)).

Attenuated Total Reflection Infrared Spectroscopy (ATR-IR) is a subset of infrared spectroscopy. Fig 22 shows how in ATR-IR spectroscopy incident Infrared light is coupled into a waveguide when the angle is greater than the critical angle. Total internal reflection occurs at the interface of the sample and waveguide(52). This produces an evanescent field parallel to the interface, which exponentially decays as it penetrates into the sample(25). The composition of the sample at the point of total internal reflection affects the effective refractive index of the sample medium, causing an optical change in the light traveling through the waveguide(53). This optical change, such as due to absorbance, can be detected to study heterogeneous catalysis(54). The limited penetration depth of the IR Evanescent waves to near the catalyst surface is beneficial to studying heterogeneous catalysis as it reduces the contribution of the bulk of the fluid to the spectrum. This allows us to focus on reactions near the catalyst surface and hence improves the signal to noise ratio of the measurements(49).

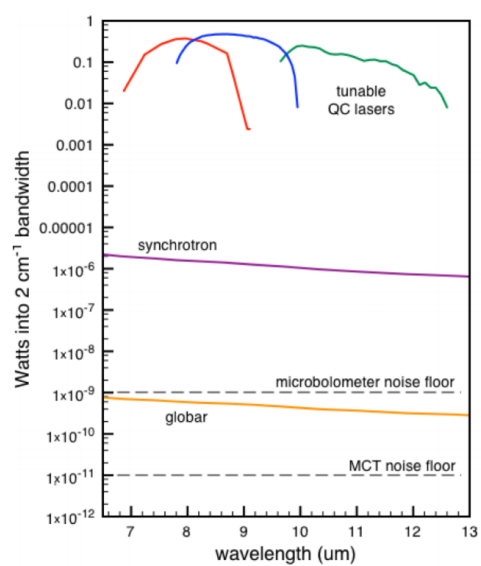


Fig. 23. Comparison of intensities of conventional and Quantum Cascade Laser sources through a $10\mu\text{m}$ pinhole (Figure from (55)).

As seen from Fig. 23, until recently conventional globar IR sources suffer from low intensity. The limitation of low intensities can be overcome by using Quantum Cascade lasers(25, 55).

Supplementary Note 2: Valves

A. Valve actuating mechanisms. A survey of the literature was carried out with the required ideal operating conditions in mind. Actuators with switching speeds in the 100s of microseconds were considered in this search. Piezoelectric, electrostatic and electromagnetic were the dominant mechanisms that were able to switch in the given time frame. An expanding microbubble thermopneumatic actuator was found to be the fastest of them all. The principles, limitations and improvements on electrostatic and piezoelectric valves are explored below.

Actuation Principle	Switching speed (μs)	Reference
Thermopneumatic (expanding microbubble)	16	(35)
Electrostatic	<50	(56)
Electrostatic	50	(57)
Electrostatic	<100 (simulated)	(17)
Electrostatic	100	(58)
Electromagnetic	300	(33)
Electrostatic and Electromagnetic	400	(59)
Piezoelectric	700	(60)
Piezoelectric	700	(61)

Table 4. Comparison of the switching times of the different valve actuation mechanisms in the sub millisecond domain

A.1. Electrostatic Valve actuators. Electrostatic valves consist of a fixed valve seat electrode and a second deformable membrane electrode. When electrical potentials are applied to each of the electrodes, an electric field is setup between the electrodes. Electrostatic attraction between the two electrodes causes the membrane electrode to clamp down and actuate the valve(56). Electrostatic valves usually require a high operating voltage on chip. Different schemes have been used to improve the performance of electrostatic valves such as an assisting pneumatic pressure (Fig.24(a))(56, 57) or assisting electromagnetic field(59), as well as structures like a double clamped membrane with an additional beam(Fig. 24(b))(17, 62).

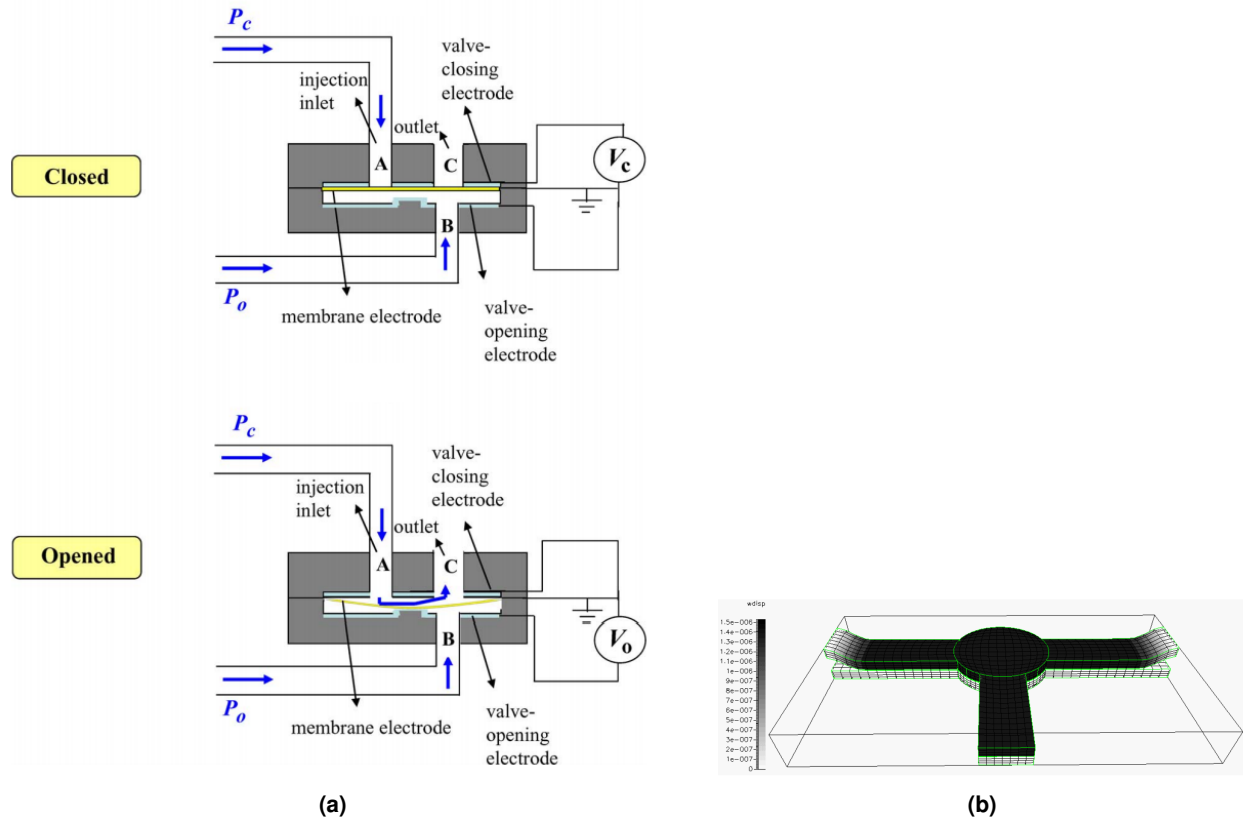


Fig. 24. Modifications to improve the performance of electrostatic valves (a) using a counter pressure (Figure from (57)) (b) using a double clamped membrane electrode with an additional beam(Figure from (62)).

A.2. Piezoelectric Valve Actuators. Piezoelectric valves use a piezoelectric actuator and a valve seat(60, 61). Piezoelectric actuators consist of crystals with polar bonds and no inversion symmetry. When a potential is applied across such a crystal,

Table 5. Effect of various parameters on the valve switching time and flow rate of reactant gases into the reaction chambers

Parameter	Flow rate scaling	Switching speed scaling
P_{ext}	Q^1	-
H_r	Q^3	-
B_r	Q^1	-
L_r	Q^{-1}	-
a_c	Q^4	t^2
L_c	Q^{-1}	-
n	Q^1	-
H_{EtOH}	-	-
a_{EtOH}	-	-

the oppositely charged atoms attract or repel changing the dimensions of the crystal as seen in Fig. 25(a). This is known as the inverse piezoelectric effect. However, even for higher voltages, piezoelectric valves have a low displacement stroke length. This can be overcome by using stacked actuators (Fig. 25) or hydraulic amplification(30).

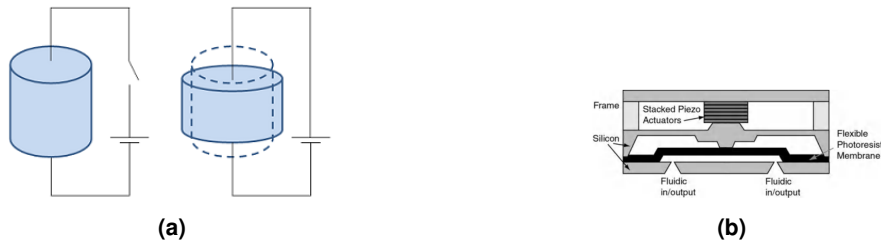


Fig. 25. (a) Schematic of a Piezoelectric crystal showing the inverse piezoelectric effect Figure from (63)) (b) Piezoelectric stack valve (Figure from (33)).

B. Valve Scaling effects. Using Equation 1, Equation 2, and Table 2 we can find the effect of the various parameters on switching speed and reactant gas flow rate. These are tabulated below.

Supplementary Note 3: Electric-Fluidic analogy for gas flow in reactor inlets

A. The Electric-fluidic analogy. An electric-fluidic analogy can be made to the parallels between Hagen-Poiseuille law and ohm's law(64, 65). These analogies (Table 6) allow us to use circuit analysis techniques from electrical engineering for analyzing the fluid flow.

Table 6. Some of the fluid and electrical analogues as described by Oh et al.

Electrical analogue	Fluidic analogue
Electrical Potential	Pressure
Current	Fluid Flow
Resistance	Fluidic Resistance
Electrons	Molecules in fluid

Using the electrical analogy of flow, this MATLAB code was used to calculate the fluidic resistance of pressure driven flow in main rectangular and cylindrical sub channels. The script is based on Equations 1 and 2 from the work of Oosterbroek which are repeated below for convenience.

$$Q_R = \frac{4\mu l}{ab^3} \left[\frac{16}{3} - 3.36 \frac{b}{a} \left(1 - \frac{b^4}{12a^4} \right) \right]^{-1}$$

$$Q_C = \frac{8\mu l}{\pi a^4}$$

B. MATLAB Script for calculating fluidic resistance.

```
% Fluidic Resistance calculations based on
% Oosterbroek, R. E. (1999). Modelling, design and realization of microfluidic
% components. Universiteit Twente.
```

```
clear all;
close all;
clc
```

```
eta=18.37e-6 %viscosity of air at 25c [Pa s]
```

```
%dimensions of circular channel[m]
r=40e-6;
h=515e-6;
```

```
%dimensions of rectangular inlet/outlet channel [m]
l1=300e-6;
b1=260e-6;
h1=40e-6;
```

```
i1=b1/2;
j1=h1/2;
```

```
%dimensions of reactor chamber[m]
l2=330e-6;
b2=600e-6;
h2=5e-6;
```

```
i2=b2/2;
j2=h2/2;
```

```
R_Circ=(8*eta*h)/(pi*r^4) %Fluidic resistance of circular channel[(Pa s)/m^3]
R_Rect=((4*eta*l1)/(i1*j1^3 *(16/3 - (3.36*j1*(1 - j1^4/(12*i1^4))))/i1)))
%Fluidic resistance of rectangular channel[(Pa s)/m^3]
R_Chamb=((4*eta*l2)/(i2*j2^3 *(16/3 - (3.36*j2*(1 - j2^4/(12*i2^4))))/i2)))
%Fluidic resistance of reaction chamber[(Pa s)/m^3]
```

$R_{Shunt} = (2 * R_{Circ}) + R_{Chamb}$
 %Series resistance of the inlet, reaction chamber and outlet

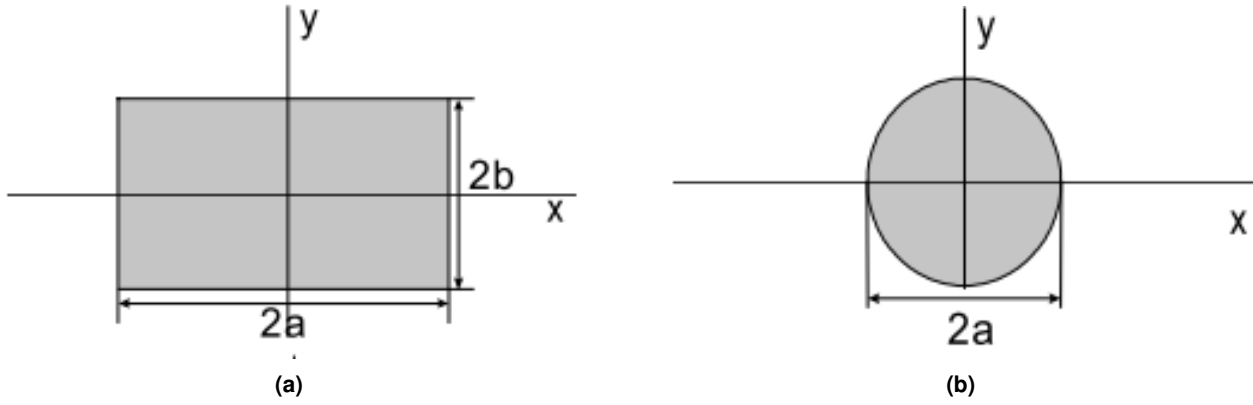


Fig. 26. Cross sections of rectangular and circular channels across which fluidic resistance is calculated (Figure from (36)).

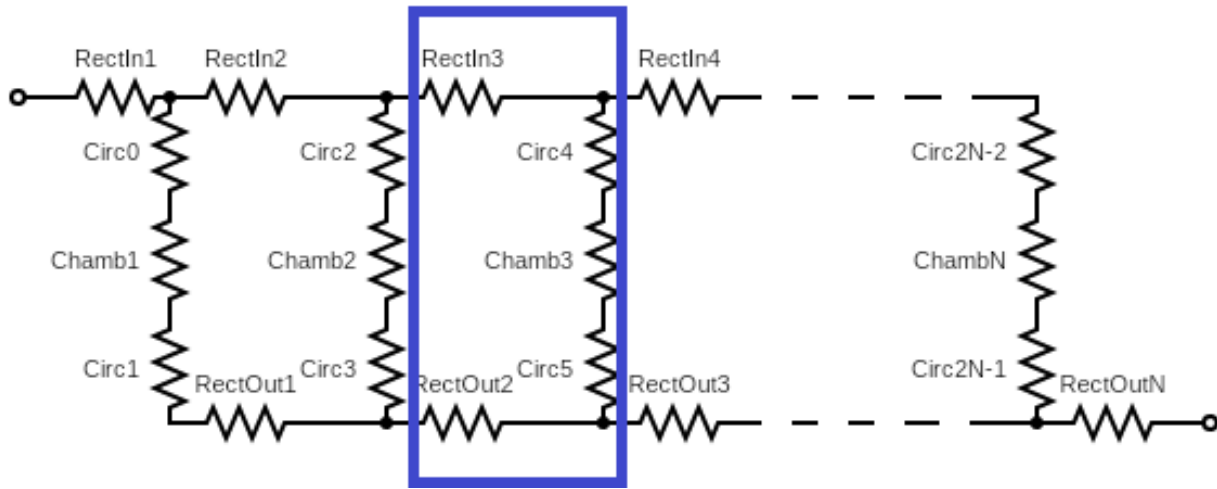


Fig. 27. Ladder network model of the fluidics on chip where the highlighted segment is repeated to represent all the reactor chambers connected fluidically in series

C. Electric network representation of the gas channels and reactor. As shown in Fig. 27, the proposed gas fluidic network can be represented as a ladder network of N rungs. The highlighted section is a repeating unit that consists of 5 fluidic resistances: Chamber resistance- R_{Chamb} (Fig. 8(b)(2)), the chamber inlet and outlet resistances- R_{Circ} (Fig. 8(a)(1)) and the main inlet and outlet resistances R_{RectIn} (Fig. 8(b)(3)) and $R_{RectOut}$ (Fig. 8(b)(4)).

A ladder network can be analyzed using a Kirchhoff matrix as explained in the supplementary information of Odijk et al. If we label the $2n$ nodes of a ladder network left to right and then top to bottom, the $2n \times 2n$ Kirchhoff matrix can be generated. The matrix for a ladder network is a symmetric matrix where the diagonal elements (i, j where $i=j$) are the sum of all conductances connected to the node i . The off diagonal elements (i, j) are the negative conductance of the resistance between i and j . The simplest ladder network consisting of 4 nodes is shown in Fig. 28. The associated Kirchhoff Matrix, M , is given by:

$$M = \begin{bmatrix} G_{T1} + G_{M1} & -G_{T1} & -G_{M1} & 0 \\ -G_{T1} & G_{T1} + G_{M2} & 0 & -G_{M2} \\ -G_{M1} & 0 & G_{M1} + G_{B1} & -G_{B1} \\ 0 & -G_{M2} & -G_{B1} & G_{M2} + G_{B1} \end{bmatrix}$$



Fig. 28. 4 node Ladder network model (Figure from (37)).

Grounding the bottom right node (node 4 in the example) we can generate the conductance matrix, C , by truncating the $2n^{th}$ row and column.

A boundary condition matrix, Q , indicating the input flow at node 1 can be generated and then the potential or pressure at all the nodes can be calculated as follows where V is the matrix of pressure:

$$V = Q \cdot C^{-1} \quad (7)$$

D. MATLAB script solving the Kirchoff matrix for Pressure at each node. A MATLAB Script was written to generate the conductance matrix of a $2n$ node ladder network given the resistances of repeating branches. The script also calculates the pressure at each node in the gas channel using the Kirchoff matrix method mentioned above.

```
%% To calculate potentials in an n ladder network
% Based on Supplementary Information of Odiijk, Mathieu, et al.
"Measuring direct current trans-epithelial electrical
% resistance in organ-on-a-chip microsystems."
Lab on a Chip 15.3 (2015): 745-752.

%% nodes are labeled from Left to Right and then top to bottom
% 1 - [Rx]- 2 - [Rx]-.....-n
% |         |         |
% [Ry]      [Ry]      [Ry]
% |         |         |
% n+1- [Rx]- n+2- [Rx]-.....-2n
%%
clc
close all
clear all

%% inputs
n=50;% n is the number of rungs of ladder network

%hydraulic resistances [(Pa s)/m^3]

Rx=4.4008e9;
Ry=9.9388e11;

Qin=4.5e-5;%flow rate [m^3 s^(-1)]
%%
%Converting branch resistances into conductances
Gx=1/Rx;
Gy=1/Ry;

%% Conductance matrix
C=zeros(2*n-1,2*n-1); %initialize conductance matrix of correct size

for i=1:2*n-1
```

```

for j=1:2*n-1

    if(abs(i-j)==1)
        if (i~=n)
            C(i,j)=-Gx;
        end
    end

    if (abs(i-j)==n)
        C(i,j)=-Gy;
    end

    if (i==j) %diagonal elements
        C(i,j)=Gx+Gy+Gx; %sum of all three conductances at that node
        if (i==1||i==n||i==n+1)
            C(i,j)=Gx+Gy; % except on first and last rung it is the sum of 2 conductances
        end
    end
end
end
C=triu(C);
G=C'+C;
for i=1:2*n-1
    for j=1:2*n-1
        if i==j
            G(i,j)=G(i,j)/2;
        end
    end
end
G; %conductance matrix

%% Boundary condition matrix

Q=zeros(1,2*n-1);
Q(1,1)=Qin; %input flow rate at node 1

V=Q*inv(C);

for i=1:n
    pot(i)=V(i);
end

node=[1:n];

plot (node, pot)
xlabel('Node number')
ylabel('Pressure [Pa]')
legend('Qin = 4.5e-5 [m^3 s^{-1}]')
hold on

```

Supplementary Note 4: Mask Designs

This section contains images of the masks designed. The CleWin file for all three masks is available online here.(43)

A. Powder Blast Mask. The powder blast mask defines the holes for inlet and outlet to fill ethanol in the chambers (Fig. 29). It is a mirrored inside black mask with wafer alignment markers.

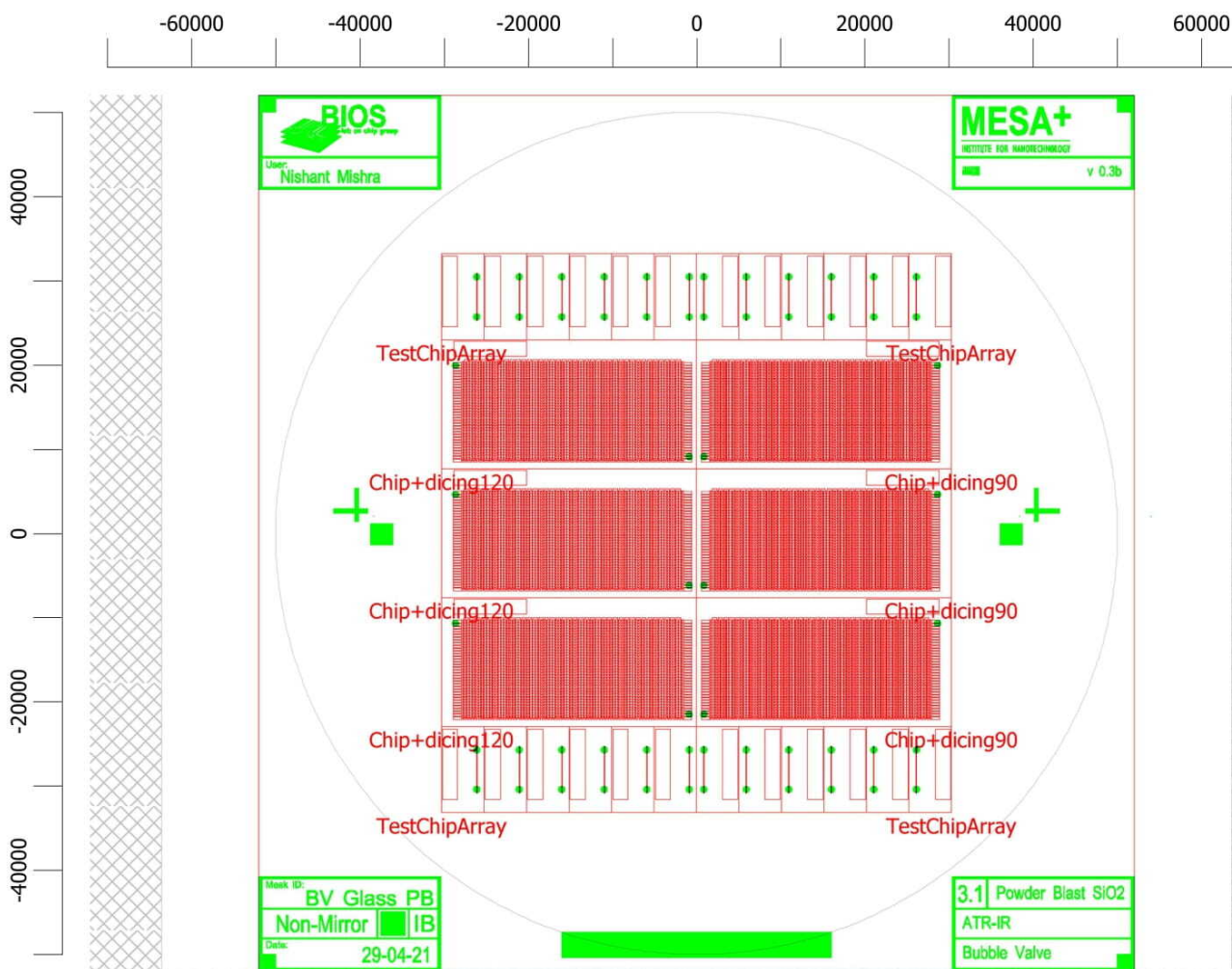


Fig. 29. The powder blast mask with main chips, test chips, and alignment markers.

B. Metalization Mask. The metalization mask defines the contact pads, heating resistors, and cooling structures on the sides of the valve (Fig. 30). The mask also includes flash zones for any arcs during anodic bonding to safely flash without damaging structures on the main or test chips. The mask also includes alignment markers. Specific features of the Metalization mask layer are highlighted in Fig. 31

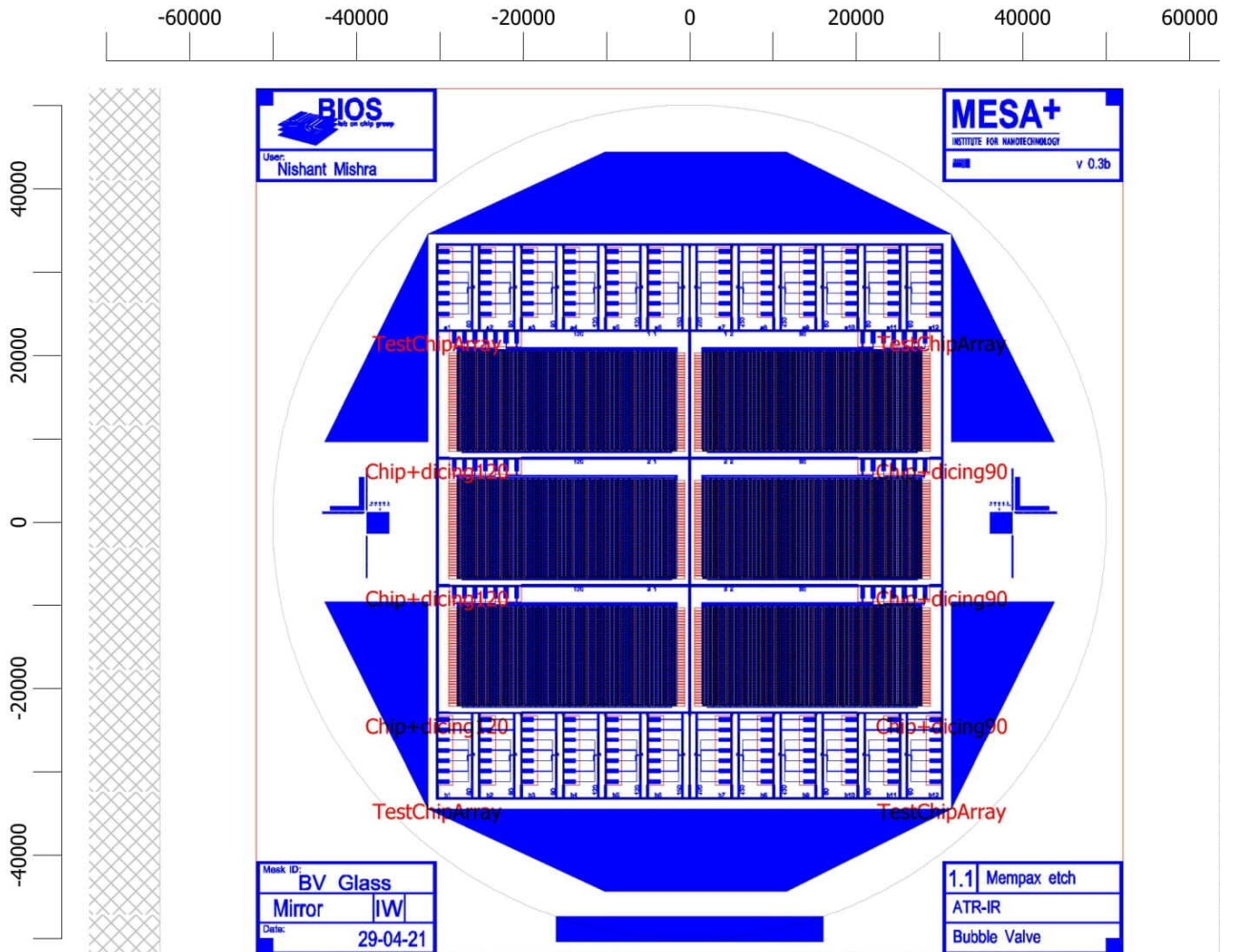


Fig. 30. The Metalization mask with main chips, test chips, flash zones and alignment markers.

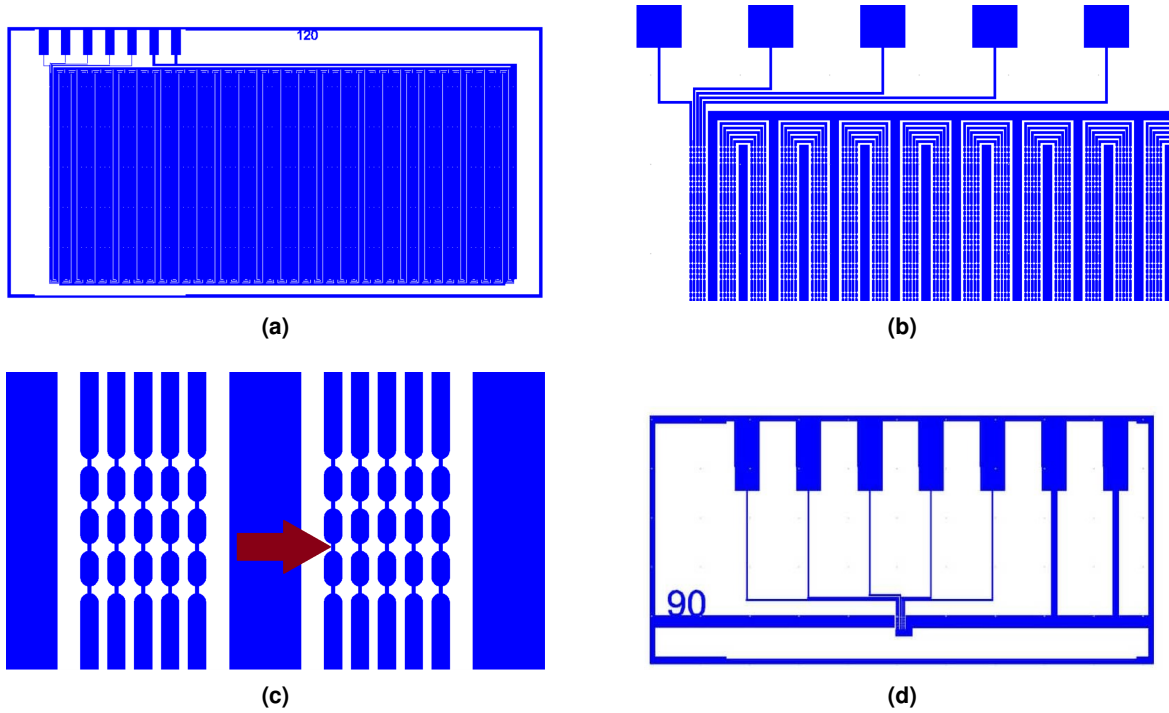


Fig. 31. (a)An enlarged view of a main chip with 7 connector pads, 5 as sources for the heaters and 2 for the ground contact. The chip also contains cooling structures, a border for the dicing saw to follow and text indicating the valve radius. (b)An enlarged view of a main chip showing how the first five traces connect to the meandering groups of heaters. (c)An enlarged view of two sets of heaters with 5 parallel traces each separated by cooling structures. The red arrow points to an individual 'pinched section' heater. (d) A test chip with a single heater cluster with the same scheme of contacts as the main chip, border for the dicing saw, and text indicating the radius of the valve.

C. Silicon etch Mask. The silicon etch mask contains the pattern for the anisotropic etch steps (Fig. 32). It consists of features defined by pre-shapes of two different sizes to be able to utilize the aspect ratio depending etching property of deep reactive ion etching. This would allow a single mask for multi depth structures. Silicon etch mask design at the main and test chips is highlighted in Fig. 33(a,e). The green overlay in Fig. 33(a,b,e) shows the powder blast mask for the ethanol filling ports. Fig. 33(c) shows the pre-shape pattern defining chambers and a channel before the VPE step, whereas in Fig. 33(d) is a simulated view of the pre-shapes interconnecting.

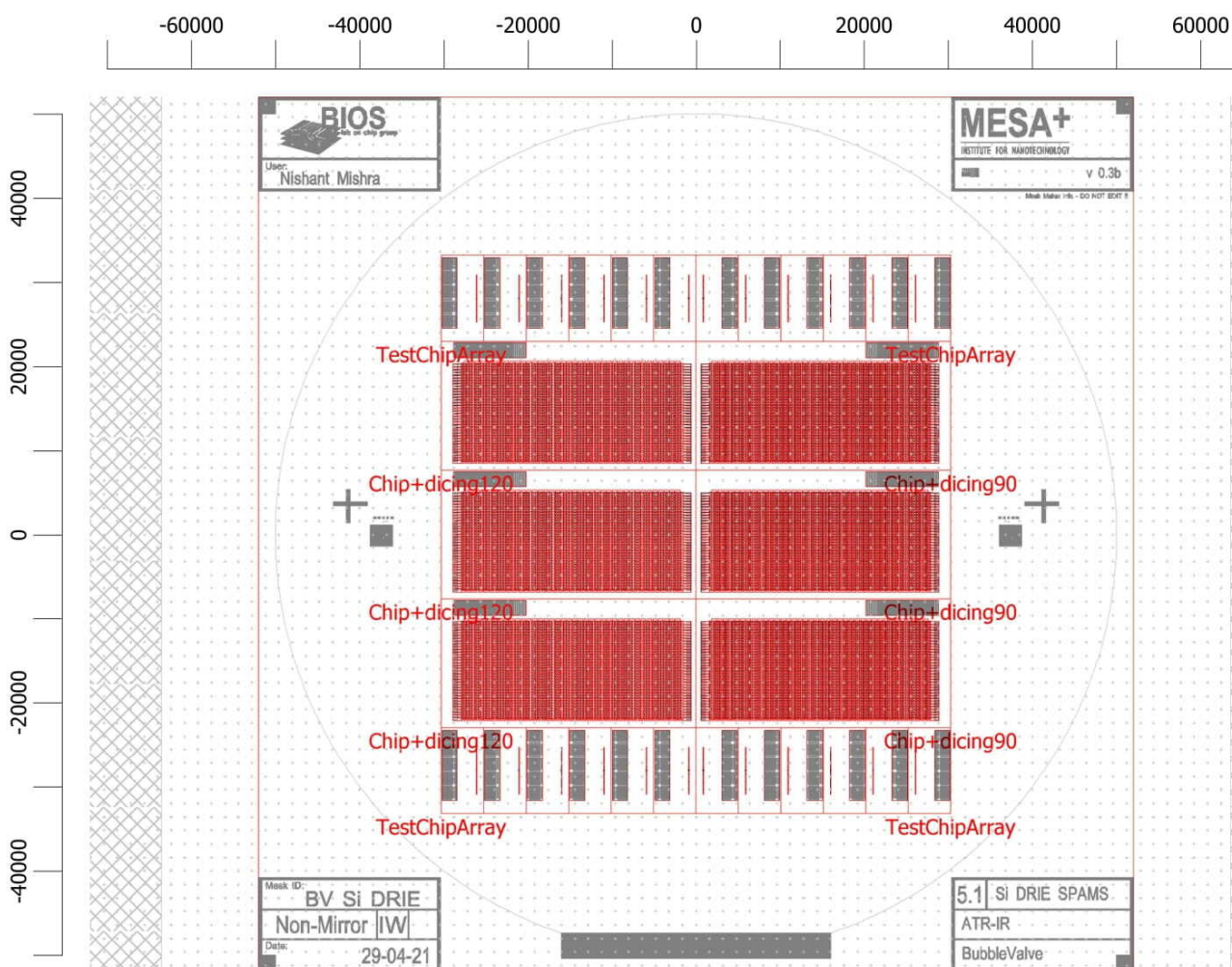


Fig. 32. The silicon etch mask with main chips, test chips, and alignment markers.

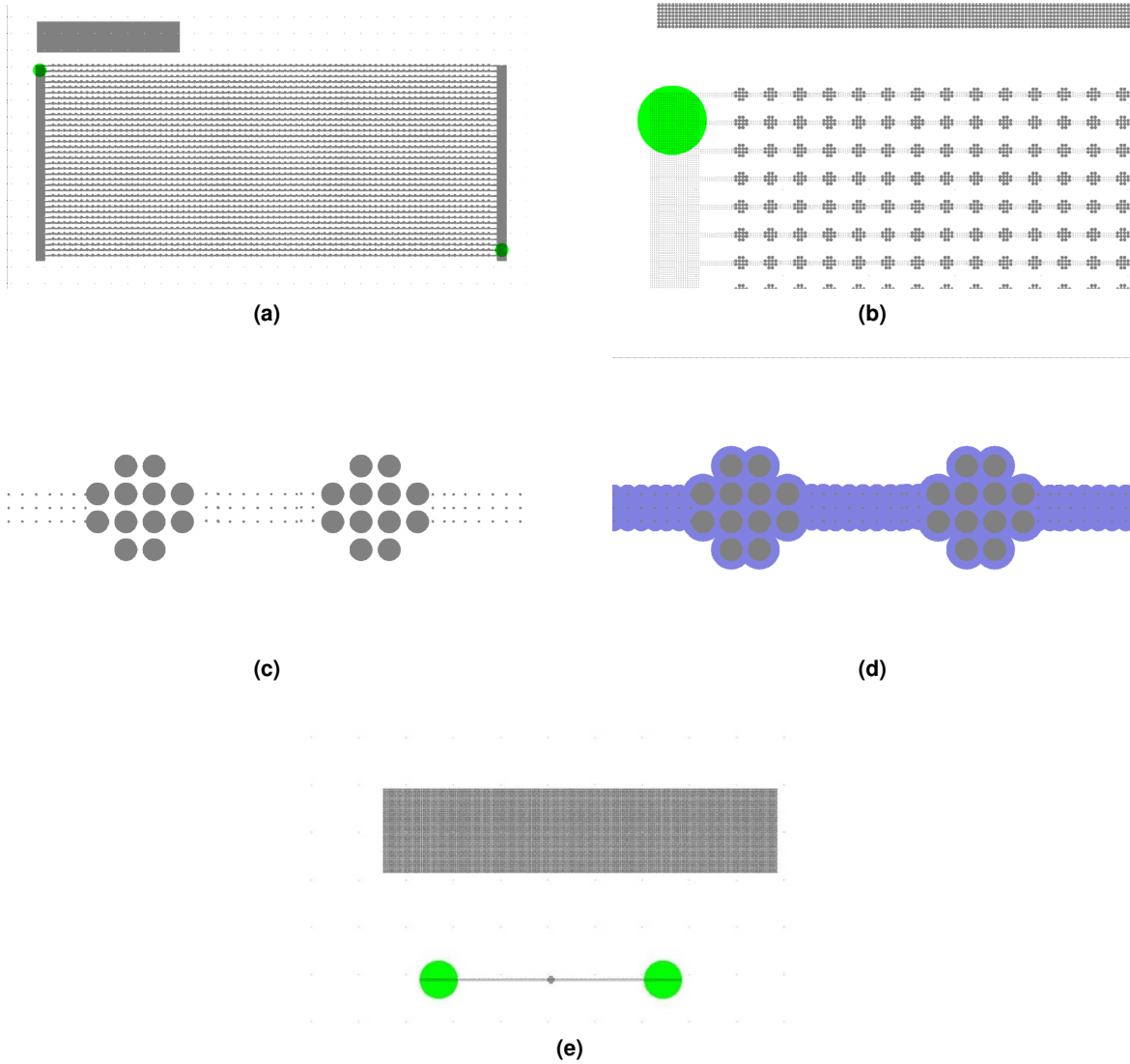


Fig. 33. (a) An enlarged view of a main chip with an opening for contact pads on the top left, two main feeder channels on the sides with an array of ethanol chambers in between. The green circles on the top left and bottom right channel define the powder blast holes. (b) a further enlarged view showing how the main feeder channel branches into sub channels connecting the chambers. (c) Smaller and larger pre-shapes used to define the channel and chamber. (d) a simulated view of the pre-shapes connecting after the isotropic etch step. (e) An enlarged view of a test chip with a single channel, single chamber and openings for contact pads. The green circles define the inlet and outlet of the ethanol channel.

Supplementary Note 5: Analytical calculations of Membrane deflection

A. MATLAB Script: Membrane deflection and profile. This MATLAB code was used to calculate the membrane deflection based on Timoshenko's theory of plates and shells(39).

```
close all;
clear all;
clc;

E= 295e9; %Elastic modulus SiN [Pa] 250 for SiN 295GPa for SiRN
nu= 0.23; %Poissons ratio SiN

valvingHeight=10e-6%distance to be travelled by valve [m]
channelRadius=35e-6%radius of circular channel[m]

h=1e-6; %membrane thickness [m]
a=119e-6; %membrane radius

D=(E*(h)^3)/(12*(1-nu^2)); %Flexural Rigidity for SiN membrane
q1=2e5-101325; %intensity of load, difference of pressures [Pa]
q2=2.5e5-101325; %intensity of load, difference of pressures [Pa]
q3=3e5-101325; %intensity of load, difference of pressures [Pa]

Wmax1=(q1*a^4)/(64*D) %max displacement of membrane [m]
Wavg1=Wmax1/3 %avg displacement[m]

r=linspace(0,a,100);%matrix of radius values[m]
W1=(q1*(a^2-r.^2).^2)/(64*D);%deflections vs radius[m]
W2=(q2*(a^2-r.^2).^2)/(64*D);%deflections vs radius[m]
W3=(q3*(a^2-r.^2).^2)/(64*D);%deflections vs radius[m]

plot(r,W1,r,W2,r,W3)
yline(valvingHeight,'--b')
xline(channelRadius,'--r')
legend({'P int=2atm','P int=2.5atm','P int=3atm','Valve
distance','circular channel radius'})
xlabel('distance from centre of membrane[m]')
ylabel('deflection [m]')
hold on
```

Supplementary Note 6: Calculations of Electrical Power

The power to be supplied to the heater is calculated following a thermal analysis used by [Van den Broek](#) and calculations of electrical power, voltage and current. A MATLAB script is written for calculating the same.

A. Thermal diffusion. The critical temperature is the temperature at which the gas cannot be liquefied by pressure alone(45). In our case, this means that a bubble will spontaneously nucleate at this temperature. For ethanol the critical temperature is 516 K(66).

The heat generated by the Pt/Ta heater will dissipate both into the MEMpax substrate below, as well as the ethanol above. The heat flux can be given by the thermal diffusion equation, which is analogous to Fick's first law of diffusion.

$$q = K \nabla T \quad (8)$$

Here q denotes the heat flux, k is the thermal conductivity, and T is the temperature.

The thermal diffusion length D is the proportionality constant in the heat equation analogous to Fick's second law of diffusion.

$$\frac{\partial T}{\partial t} = D \nabla^2 T \quad (9)$$

D here is given by

$$D = \frac{k}{\rho c_p} \quad (10)$$

Here c_p is isobaric heat capacity and ρ is the density of the material.

B. Thermal penetration depth. In our case, during the initial pulse, the liquid can be assumed stationary and hence convective heat transfer can be neglected. Additionally, heat transfer by radiation is neglected due to the relatively small temperature difference and area of the heater. This leaves only the convective mode of heat transfer. Depending upon the duration of the electrical pulse applied, the heat would penetrate to a distance equal to the diffusion length. This thermal penetration depth is given by

$$L = \sqrt{\pi D dt} \quad (11)$$

where dt is the time duration of applied heating pulse.

C. Thermal circuit. An electrical analogy can be used to analyze the heat flow in the system. Considering the heater as a source, heat will flow to the sink at room temperature with the two materials each having a particular thermal resistance.

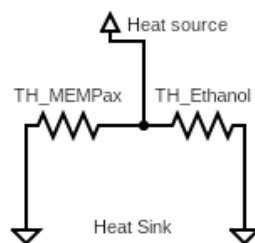


Fig. 34. Thermal circuit following the electrical analogy of heat flow.

As can be seen from Fig. 34, the two thermal resistances of MEMpax and Ethanol can be assumed to be in parallel. The thermal resistance of a material, R_{Th} is given by:

$$R_{Th} = \frac{L}{kA} \quad (12)$$

Where A is the area in contact and L is the path length. In our case the path length is equal to the thermal penetration depth. Using the thermal analogue of Ohm's law, where ΔT , the temperature difference is the driving force, the heat flow Q can be obtained.

$$Q = \frac{\Delta T}{R_{Th}} \quad (13)$$

D. Power calculations. The metalization mask design consists of 5 parallel traces, each that can be actuated independently. In the test chips with a single valve, each of the parallel traces consists of 4 pinched sections that act as heaters. The dimensions of these pinched sections is $5\mu m \times 10\mu m$ each.

Thus knowing the area of the pinched section and the heat flux from Eq. ??, the power dissipated at each pinched section can be calculated as follows:

$$q = \frac{P}{A} \quad (14)$$

where A is the area of the resistor.

The current required through each individual resistor can be found from the equation:

$$P = I^2 R \quad (15)$$

Here I is the current and R is the electrical resistance of the heater. The resistance R is given by

$$R = \rho_R \frac{l_{current}}{A_{crossSection}} \quad (16)$$

In the above equation ρ_R is the resistivity, $l_{current}$ is the direction along the flow of current and $A_{crossSection}$ is the cross section area perpendicular to the direction of current flow. It is important to note that the resistivity of thin films is different from the resistivity of bulk materials as noted by [Tiggelaar](#).

From these equations, the current through one of the resistor sections can be calculated to be 44.1 mA. From the dimensions of the contact pads, traces and heaters, the potential is calculated to be 33.45V for test chip with a single valve.

E. MATLAB Script. The MATLAB script to perform these calculations is given below.

```
clc;
clear all;

%% Diffusion length

k_l=0.171; %thermal conductivity of the liquid, Ethanol [W/(m K)]
k_s=1.143; %thermal conductivity of solid, MEMpax (pyrex) [W/(m K)]

rho_l= 789; %density of the liquid, Ethanol [Kg/ m^3]
rho_s= 2230; %density of the solid, MEMpax(pyrex) [Kg/ m^3]

cp_l=2460; %isobaric heat capacity of the liquid, Ethanol [J/ (Kg K)]
cp_s=750; %isobaric heat capacity of the solid, MEMpax(pyrex) [J/ (Kg K)]

D_l= k_l/(rho_l * cp_l); %Thermal diffusivity of ethanol [m^2/s]
D_s= k_s/(rho_s * cp_s); %Thermal diffusivity of MEMpax [m^2/s]

dt= 10e-6; %time of applied heating pulse [s]

L_l= sqrt(pi*D_l*dt); %Thermal diffusion length in ethanol [m]
L_s= sqrt(pi*D_s*dt); %Thermal diffusion length in MEMpax [m]

%% Thermal resistances
A= 5e-6 * 10e-6; %area of pinched section heater [m^2]

R_Th_l= L_l/(A*k_l); %Thermal resistance of the ethanol up till
%thermal penetration depth [K/W]
R_Th_s= L_s/(A*k_s); %Thermal resistance of the MEMpax up till
%thermal penetration depth [K/W]

R_Th_net=(R_Th_l*R_Th_s)/(R_Th_l+R_Th_s); %Net thermal resistance of the system [K/W]

%% Heat flow
dT=516.25-293.15; %Temperature difference between room temp and critical temp of ethanol [K]
```

```

q_net=dT/R_Th_net; %Net flow of heat from the Pt heater [W]

%% Current through resistor

trace_depth=160e-9; %Depth of sputtered layer of Pt/Ti [m]
rho_pt=0.16e-6; %Resistivity of thin film Pt/Ti [ohm m]
L_heater=10e-6;% length along the direction of
%current flow of heater [m]
A_cross_heater= 5e-6 * trace_depth; % heater area of cross section perpendicular to
%the direction of flow of current [m^2]
L_hconnector=50e-6; % length along the direction of
%current flow of sections connecting 2 heaters[m]
A_cross_hconnector=25e-6*trace_depth; %heater connector area of cross section
%perpendicular to the direction of flow of current [m^2]

%% Equating heat to electrical power

R_E_Heater=rho_pt*L_heater/A_cross_heater; %resistance of pinched heater section [ohm]
R_E_hconnector=rho_pt*L_hconnector/A_cross_hconnector;%resistance of section
%connecting two heaters [ohm]

I=sqrt(q_net/R_E_Heater) %Current through the resistor [A]

%% Potential across the Contacts

L_pad=1418e-6; %length of contact pad on test chip [m]
A_pad= 500e-6 * trace_depth; %area of cross section perpendicular to
%the direction of flow of current [m^2]
R_E_Pad=rho_pt*L_pad/A_pad; %resistance contact pad section [ohm]

L_trace=4600e-6; %Average trace length on test chip [m]
A_trace= 25e-6 * trace_depth;%area of cross section perpendicular to the direction of
%flow of current [m^2]
R_E_trace=rho_pt*L_trace/A_trace; %resistance of trace [ohm]

L_gnd= 70000e-6; %Length of ground trace [m]
A_gnd= 125e-6* trace_depth; %area of cross section perpendicular to the direction of
%flow of current [m^2]
R_E_gnd=rho_pt*L_gnd/A_gnd; %resistance of ground trace [ohm]

n_heaters=4; %Number of pinched heaters

R_E_net= (2*R_E_Pad)+(n_heaters*R_E_Heater)+R_E_trace+R_E_gnd;
%Total path electrical resistance on test chip [ohm]

V=I*R_E_net %Potential to be applied across the trace [V]

```

Supplementary Note 7: Control Circuit

A. Proposed control scheme for the heater. In this section, a proposed control circuit is presented (Fig. 35). The current in the heaters (represented by R_{Load}) needs to be controlled by a microcontroller. This control is necessary to not only operate the valves but also to prevent overheating of the system and possibly damaging the membrane. One of the required functions of the heater is also to be able to trigger a high speed camera for studying the bubble evolution dynamics.

Depending on the thermal coefficient of resistivity for Pt and Ta , the resistance of the traces would change with temperature. Following a calibration, measuring this temperature change would allow us to measure the temperature of the traces. The circuit consists of a current sense resistor, a current sense amplifier, a microcontroller, an opamp, and an NMOS. As the sense resistor is in series with the NMOS and the load trace heaters, the current through the sense resistor is the same as that through the heaters. The current sense resistor and amplifier can be used to measure the current.

The current sense resistor has a very low resistance and produces a corresponding low potential drop across itself. This potential difference is measured by the current sense amplifier and fed into the microcontroller. The microcontroller then controls the NMOS. In addition to this, the microcontroller also triggers the high speed camera with a (0-5V) TTL signal of $10\mu s$.

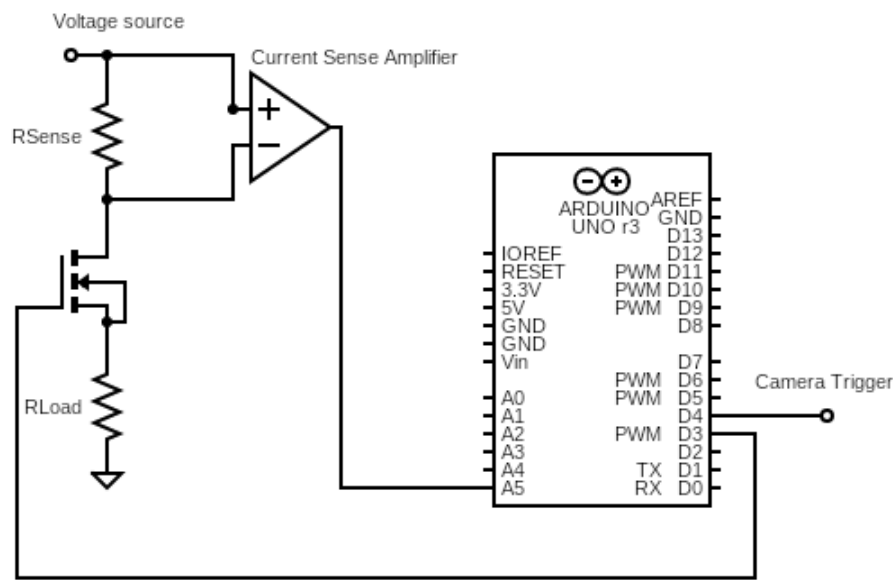


Fig. 35. Proposed circuit for controlling the heater

B. Example Arduino code for operation. An arduino code for triggering the high speed camera and producing a heating pulse is presented in this section. The code is based on the arduino example 'blink without delay'. Ideally the measurement and triggering functions could be separated into different cores if using a microcontroller such as the ESP32. The conversion factor between potential and temperature can be measured in calibration experiments. More complex transfer functions such as the Steinhart-Hart model can be used to approximate the relationship between temperature and resistance.

```
//Calibration and setting variables
int K=5;
int d=0.1; //delay between two heating pulses in ms
int HeaterOnTime=10; //period of heater pulse in us

//defining pins
const int nmos = 3;
const int cam = 4;
const char sens= A5;

//timing variables
unsigned long previousUs = 0;
unsigned long previousUs1 = 0;
```



```

//Other variables
int Vsens,Tmeasure,T;
int Tcrit=516;//critical temperature of ethanol in K

void setup() {
  // put your setup code here, to run once:
  Serial.begin(9600);

  pinMode(nmos,OUTPUT); //set up Digital output 3 to control NMOS
  pinMode(cam,OUTPUT); //set up Digital output 4 as trigger for camera
  pinMode(sens,INPUT);

}

void loop() {
  // put your main code here, to run repeatedly:
  Vsens = analogRead(sens);
  T= K*Vsens; //assuming a linear relationship between the current and temprature,
  //the value of K can be set after calibration

  if(T<Tcrit){
    camTrigger();
    heaterPulse();
  }
  delay(d);
}

void camTrigger(){
  //function to trigger a 5v 10us Square wave pulse for the high speed camera
  unsigned long currentUs = micros();
  digitalWrite(cam,HIGH);
  if (currentUs-previousUs>=10){
    previousUs = currentUs;
    digitalWrite(cam,LOW);
  }
}

void heaterPulse(){
  //function to trigger a 5v Square wave pulse for gating the MOSFET for
  //pulse duration HeaterOnTime
  unsigned long currentUs1 = micros();
  digitalWrite(nmos,HIGH);
  if (currentUs1-previousUs1>=HeaterOnTime){
    previousUs1 = currentUs1;
    digitalWrite(nmos,LOW);
  }
}

```

Supplementary Note 8: Process flows

A. Optimizing the SPAMS process. The SPAMS process consisted of preparing a hard mask, patterning it via Reactive Ion Etching (RIE). This is followed by anisotropic Deep Reactive Ion Etching (DRIE) and finally isotropic Vapour Phase Etching (VPE). The challenges encountered in this processing as well as the possible reasons and solutions are detailed in this section.

A.1. Patterning the Hard mask. The hard mask is a film of SiO_2 and $SiRN$ that is used to protect the bulk from being etched by the DRIE process. In our case the hard mask was to be patterned with many small pre-shape features. The first step in forming the hard mask was optical lithography, which was followed by RIE etching. We chose for a thicker Olin Oir 908-35 resist formulation that would give us a thicker, $3.5\mu m$, layer of photoresist. Since our smallest features had a radius of only $1.5625\mu m$, the exposure time of 9s was insufficient as seen in Fig. 36. The dose was adjusted by increasing the exposure time from 9s to 12s. This means that the effective dose was $272mJ/cm^2$ which ensured the complete opening of the smaller pre-shapes in the resist.

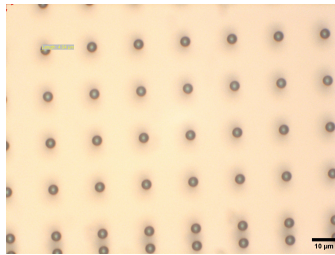


Fig. 36. Underexposed pre-shapes of diameter $3.125\mu m$ in Olin Oir 908-35 resist after 9s of exposure. The dark rings inside the pre-shapes indicate that the photoresist was underdeveloped

In the interest of parallelization of processing, the Plasma-Therm 790 was chosen that could process up to 4 wafers at once. The Plasma-therm 790 used a CHF_3/O_2 plasma to etch SiO_2 . However due to the large loading effect of pre-shapes, the etch rate and etch uniformity of the wafers was poor and directional as seen in Fig. 37. The etch rate was higher at the centre than at the edges. The wafers were rotated 90 degrees from their original position in the middle of processing to help improve uniformity. After 127 minutes of etching, the hard mask was successfully opened but for subsequent RIE etching the Adixen AMS100DE was used. The Adixen used a $C_4F_8 - He - CH_4$ cycle and had a predicted etch rate for SiO_2 of 500nm/min. This process was optimized for the hard mask of $1\mu m$ $SiRN$ and $2\mu m$ SiO_2 to take 7 minutes. This RIE setup could only etch one wafer at a time.

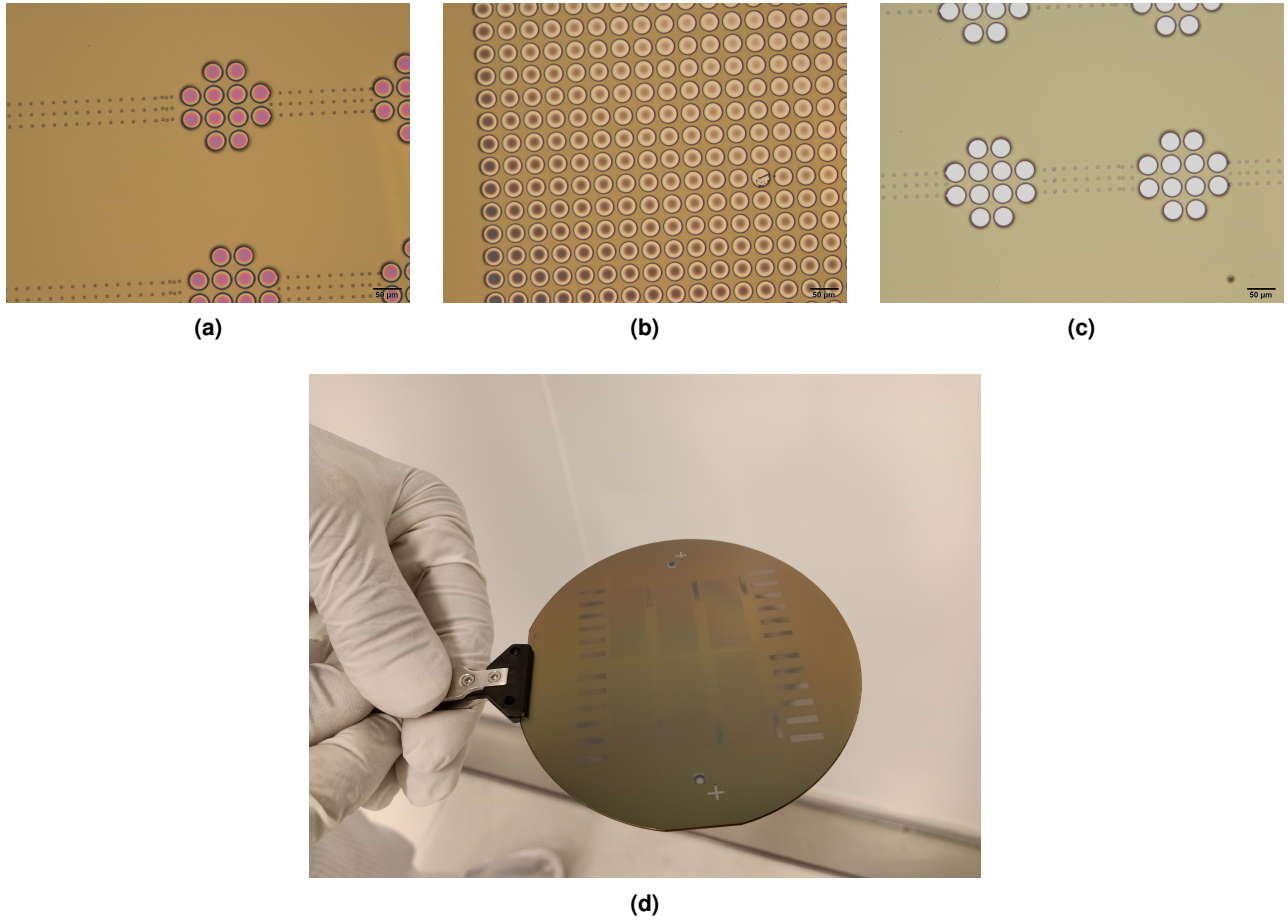


Fig. 37. RIE etch rate differences after 107 minutes of etching in the 4 wafer Plasma-therm RIE chamber. (a) Higher etch rate at the centre of the wafer. (b) Image taken at the right edge of the wafer showing a gradient in the opening of the hard mask towards the centre. The etch rate is higher near the centre than the edges (c) Complete opening of pre-shapes at the centre of the wafer after 127 minutes of etching. (d) Image of the complete wafer after 127 minutes of etching showing a dark radial pattern indicating etch rate differences near the edge.

A.2. Forming the pre-shapes. Once the hard mask was patterned, the recipe for the anisotropic DRIE etch was to be optimized. In the course of this work, we tried three different etch recipes and variations on them.

The DRIE Bosch process consists of three steps as shown in Fig. 38. At first the substrate exposed by the hard mask is etched isotropically by an ionized etching gas. Next, the reaction chamber is flushed and a passivating gas is introduced. This gas forms an etch resistant fluorocarbon layer on the mask, substrate and etched sidewalls. Next, optionally, a short pulse of the ionized etch gas is included which removes the fluorocarbon layer at the bottom of the trench but doesn't etch away the hard mask(67). Finally, the ionized etch gas is also accelerated towards the trench and the isotropic etch is repeated. This cycle is continued until the desired etch depth is reached. In this work, the SPTS Pegasus etch system was used for all DRIE recipes.

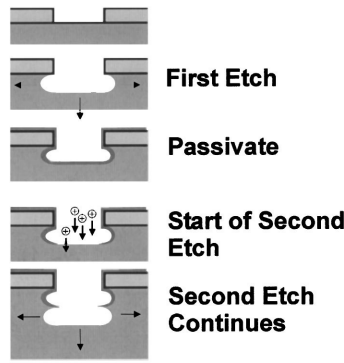


Fig. 38. Schematic showing the etch-passivate-etch cycle of DRIE. The thicker dark lines represent a layer of etch resistant polymer (Figure from (68)).

The standard silicon -19°C etch recipe: At first a high etch rate -19°C standard silicon etch recipe was used(69). This recipe consisted of 2 s of C_4F_8 deposition, followed by 2.5s of breaking the fluorocarbon with SF_6 which is followed up by further 4.5s of isotropic etching by SF_6 at a higher etch rate. After 20 minutes of this etch recipe, by focusing the z stage of a microscope first on the trenches, then on the hard mask layer, we estimated the depth of the bigger pre-shapes to be $225\mu\text{m}$. Based on the required depth of $508\mu\text{m}$, it was estimated that we should continue this etch for an additional 25 minutes for a total of 45 minutes. Kapton tape was used on the wafer alignment markers as they were getting etched deeper due to their relatively larger exposed surface area as compared to the pre-shapes.

Unfortunately, after the additional etch, the hard mask was completely eroded. The wafer was originally $525\pm 5\mu\text{m}$ thick with $1.5\mu\text{m}$ of SiO_2 , $1\mu\text{m}$ of SiRN and $3.5\mu\text{m}$ of Olin resist. The thickness of this wafer measured after the 45 minutes of etching using a stylus probe to be $412.5\mu\text{m}$ at the centre of the wafer and $502\mu\text{m}$ at the edge. This indicated that the etch rate at the centre was more than at the edge. The wafer was cleaved to measure the profile of the structures.

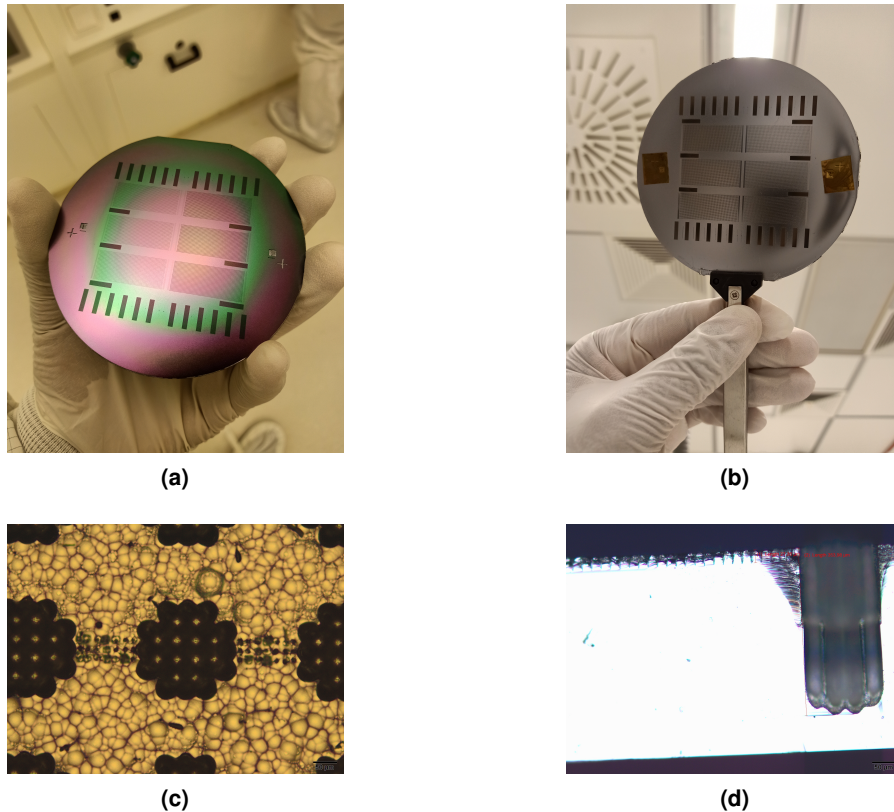


Fig. 39. Results of using the standard -19°C etch recipe. (a) Wafer with an estimated 800nm hard mask left after 20 minutes of etching. (b) wafer with an eroded hard mask but no membrane release. Microscopy images showing (c) damage on the silicon surface due to the RIE etch and (d) a cross section showing the ARDE effect with smaller pre shapes being etched to a lesser depth ($27\mu\text{m}$) than the bigger ones ($354\mu\text{m}$). From another image of the same wafer the remaining depth to release the membrane was $74\mu\text{m}$.

A variation on the standard etch recipe was also tried where the etching part of the cycle was increased from 7 to 7.4s and the deposition time was increased from 2 to 2.4s. This etch was carried out for 192 cycles and also led to hard mask erosion before membrane release.

The HARS recipe: The next variation that was tried was the Bosch high aspect ratio structures recipe (HARS)(70). This recipe consisted of 0.5s of deposition of C_4F_8 and 1.75s of etching by SF_6 at 20°C. However the flow rates and the power of the inductively coupled plasma were lower than the original standard silicon etch recipe.

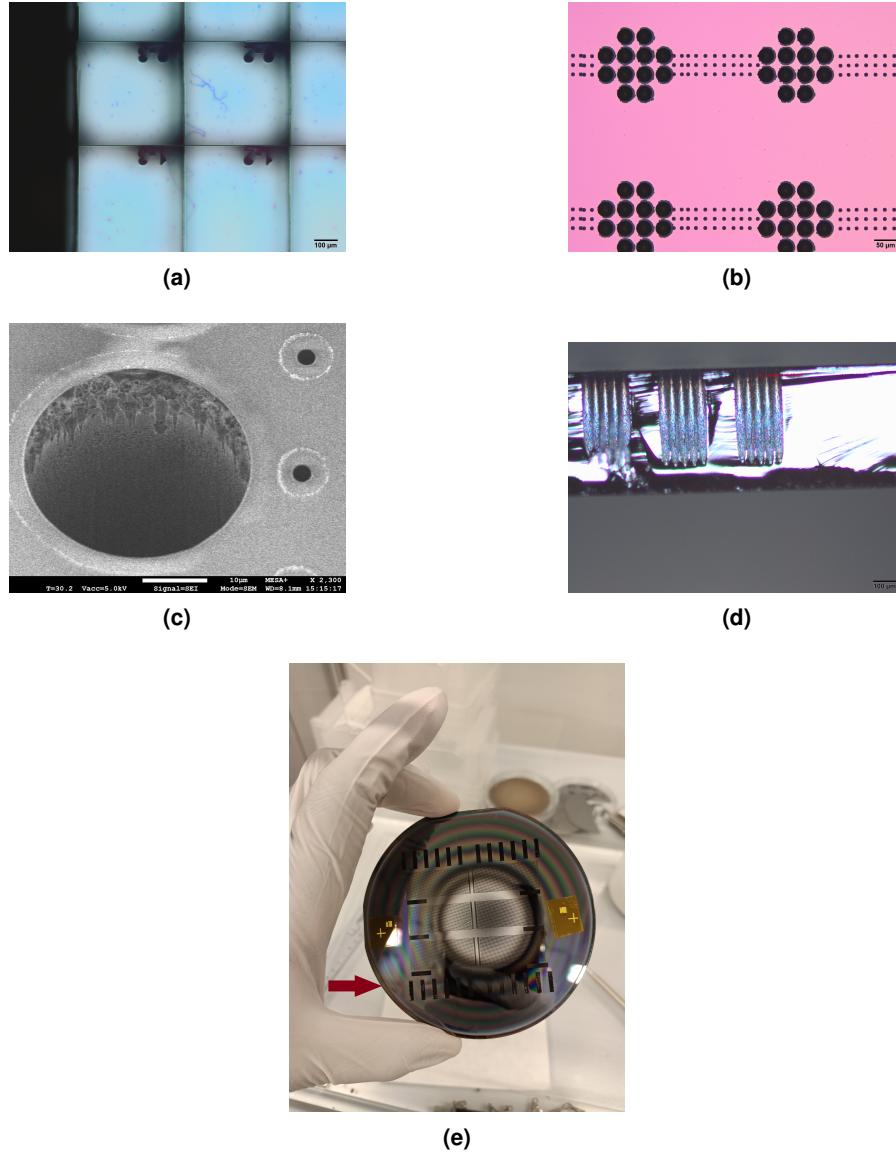


Fig. 40. Results of using the HARS etch recipe. (a) Membrane release at alignment markers. Specks of silicon reveal that a thin layer is left. (b) Pre-shape patterns etched in the silicon. (c) Tilted SEM image of one large and two of the smaller pre-shapes. (d) Cross section of the edge of a wafer processed for 2300 cycles showing an etch depth of $415\mu m$. (e) Picture of the complete wafer showing hard mask eroded in the centre after 2300 cycles. The arrow indicates a ring of the original unetched hard mask which is covered by the clamp ring in the SPTS system.

From the process document(70) we estimated that to etch to a depth of $508\mu m$ we would need to etch for 1560 cycles (approx. 1 hour). After 1350 cycles (approx. 50 minutes) of etching the hard mask remained and the membrane was released at the mask alignment pattern as seen in Fig. 40. Some specks of etched silicon seen in the microscopy images of the alignment markers revealed that the silicon nitride membrane was still present. The depth of the larger or smaller pre-shapes could not be estimated using non destructive methods such as focusing with the Z stage, tilted SEM, contact profilometry or white light interferometry because of the large aspect ratio of the pre-shape structures. It was assumed that these structures were deep enough and the

wafer was processed further which revealed that the depth was not enough. For further experiments with HARS and other recipes, a thicker hard mask was deposited with $1\mu\text{m}$ of Si_3N_4 and $2\mu\text{m}$ instead of $1.5\mu\text{m}$ of SiO_2 . Later a wafer was processed for 2300 cycles (86 minutes) but only etch depths of $391\mu\text{m}$ at the centre and $415\mu\text{m}$ at the edge were achieved before the thicker hard mask was etched away from the centre.

Variations in the number of cycles, SF_6 and Ar pressures, introducing oxygen, and changing platen powers were tried but the same issue was encountered- the etch rate was higher at the centre than at the edges and the hard mask would be eroded.

The standard silicon 0°C etch recipe: The final DRIE variation tried was the 0°C standard silicon recipe. Similar to the original silicon etch recipe, this DRIE recipe also consists of three steps- the deposition (2s), break(1.3s) and etch(5.7s). Further, the Inductive and capacitively coupled powers are the same and the only difference is that this 0°C etch has a higher pressure at the fluorocarbon break stage. At the fluorocarbon break stage active pressure controller (APC) is set to 100% in this recipe instead of at 8% for the -19°C standard silicon etch.

After 30 minutes of the 0°C etch, the wafer was diced and cleaved to measure the depths of the DRIE holes. As seen in Fig. 41(a) the bigger pre-shapes had a depth of $331\mu\text{m}$ and the smaller pre-shapes have a depth of $120\mu\text{m}$. One of the chips from the now diced wafer was secured to a dummy SiO_2 wafer and processed for a further 15 minutes, however the mask layer was etched away on this chip because of lower loading by the sample. This is shown in Fig. 41 (d).

Another wafer was processed with the same recipe in steps of 5 minutes from 30 to 45 minutes. After 45 minutes there was an estimated 200nm of mask layer remaining. The SPTS clamp ring covers the outer perimeter of the wafer as indicated by the red arrow in Fig. 40 (e). This results in an unetched ring of the mask on the wafer. The step height between the unetched ring of the mask and the etched portion was measured using the Dektak contact surface profilometer to be 3356nm. As the initial thickness of the nitride and oxide layers together was around 3500nm, this confirmed that only about 144nm of mask layer was remaining. This wafer was also diced and cleaved. The depths of the pre-shapes were measured to be 413 and $154\mu\text{m}$ for the bigger and smaller pre-shapes as seen in Fig. 41 (b). The 0°C etch recipe also undercut etched by $2\mu\text{m}$ from the pre-shapes as seen in Fig. 41 (c).

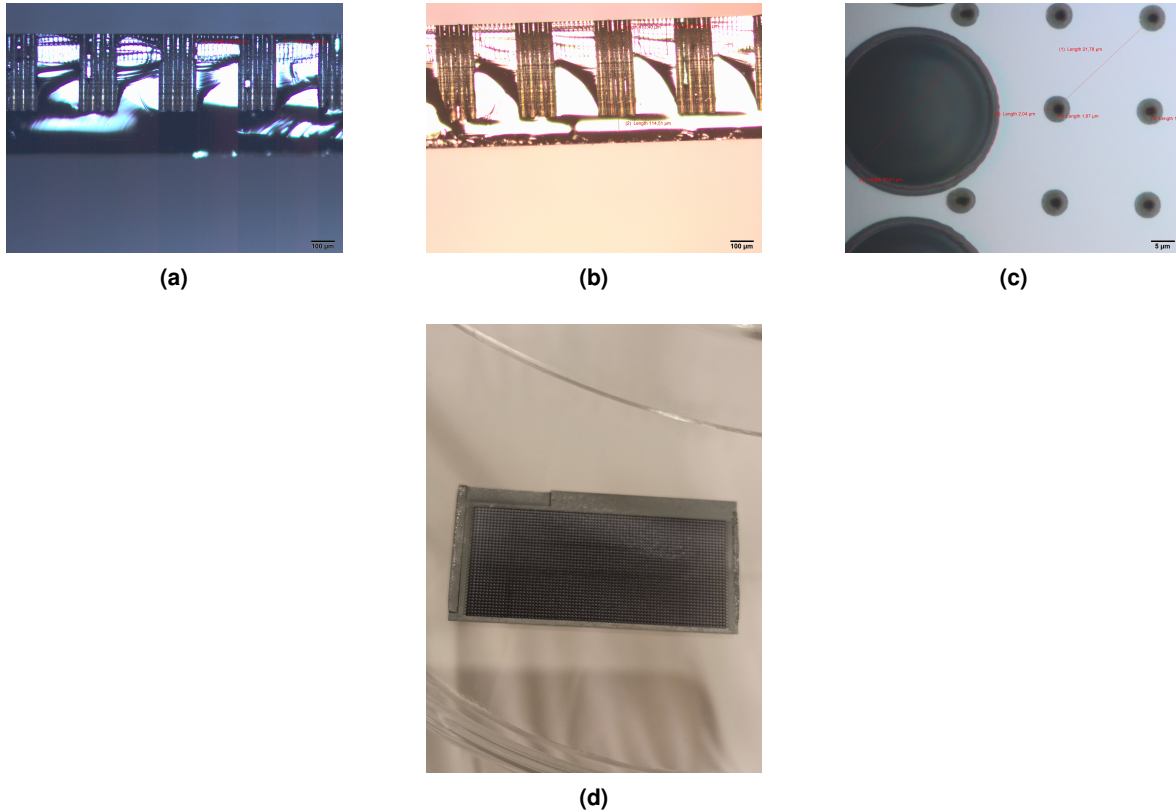


Fig. 41. Results of using the 0°C standard silicon etch recipe. Cross section of wafer after (a) 30 minutes of etching, (b) 45 minutes of etching. (c) Shows an undercut etch of approx. $2\mu\text{m}$ after 45 minutes of etching with the 0°C recipe. In (d) we see the erosion of the mask layer due to lower loading when diced and processed for an addition 15 minutes

In summary the three DRIE recipes and their variations were unsuccessful in producing the required $508\mu\text{m}$ deep holes with the bigger pre-shapes. The -19°C standard etch resulted in a depth of $354\mu\text{m}$, the HARS recipe resulted in a depth of $415\mu\text{m}$

and the 0°C standard etch resulted in a depth of $413\mu\text{m}$. One notable difference between all three recipes is that the micro loading effects were the least in the 0°C standard etch recipe. This means that all the pre-shapes of larger diameter were etched to a uniform depth. The smaller pre-shapes were also etched to the deepest depth with the 0°C etch recipe. Overall a combination of HARS 1350 cycles (approx. 50 minutes) and 200 cycles (30 min) of the 0°C produced the deepest trenches ($470\mu\text{m}$) for the bigger pre-shapes as seen in Fig. 42(a),(b). Unfortunately this process also eroded the hard mask required in the next steps (Fig.42(c)). In addition to that there was a difference of about $10\mu\text{m}$ in the etch depth at the centre compared to the edge.

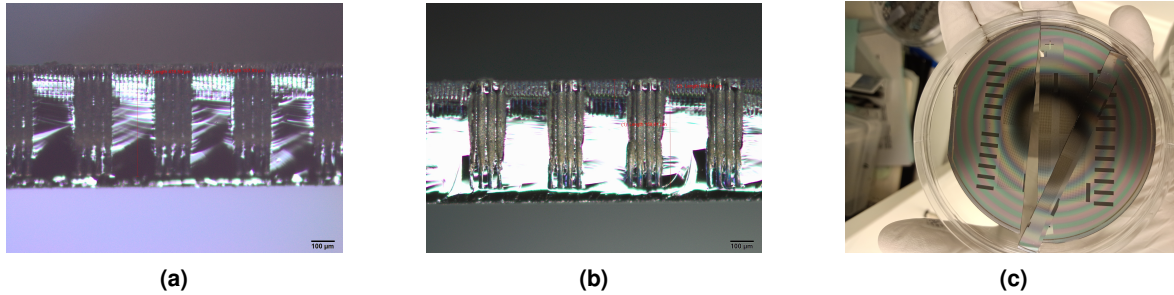


Fig. 42. Results of 50 minutes of HARS and 30 minutes of 0°C standard silicon etch recipe. Cross section of wafer (a) at the centre, (b) at the edge. (c) Image of the whole cleaved wafer showing erosion of the hard mask at the centre.

Effect of process parameters on DRIE etch The various process parameters that were varied in the above experiments affecting the etch rate, etch selectivity, etch lag and uniformity are discussed in this section.

- **Gas composition:** The DRIE etch process in the SPTS pegasus can use fluorocarbons like CHF_3 & C_4F_8 and non reactive gases like Ar , He , and N_2 and other gases like SF_6 & O_2 .

Plasmas of fluorine containing compounds such as SF_6 and CHF_3 are used to isotropically etch silicon via fluorine based chemistry. Addition of O_2 in SF_6 etching acts as an inhibitor in mixed mode DRIE. It is believed that O_2 competes with fluorine for the available bare silicon sites for chemisorption(71). Addition of O_2 in $\text{CHF}_3/\text{C}_4\text{F}_8$ pulsed mode etching increases the fluorine to carbon ratio of the halocarbon by forming $\text{C}-\text{O}$ compounds(72). The addition of N_2 increases the concentration of atomic fluorine(73). These in turn increases the lifetime of fluorine and hence the chemical etching.

On the other hand for gases like C_4F_8 which contain a higher amount of carbon act as inhibitors(68). At low bias applied at the substrate, polymerization into inert $(\text{CF}_2)_n$ polymers is favoured.

The plasmas of inert gases can be accelerated towards the substrate and isotropically etch silicon or fluorocarbon layers(74).

- **Flow rates and cycle times:** The flow rates of the etchant, and inhibitor gases determine the extent of isotropy of the etch cycle and the thickness of the passivation layer respectively. Increasing the fluorocarbon etch times of the inert gases will etch away the fluorocarbon at the bottom of the trenches, enabling higher etching at the next step. However increasing the fluorocarbon break time will also deplete the mask layer faster as it is a physical ion bombardment process instead of a chemically selective one(75). As mentioned earlier, adding O_2 to fluorocarbon etching increases the etch rate. On the contrary adding H_2 favours polymerization(75, 76).

The relative cycle times also determine the scallop size and overall processing times. Longer etch and deposition cycles will result in bigger scallops. On the other hand shorter cycles will produce smoother sidewalls at the cost of extended process time.

- **Pressure:** Higher pressure leads to more reactive species being generated(75) which in turn increase the etch rate. High pressure also favours selectivity(77).
- **Substrate Temperature:** A cooler substrate temperature decreases the energy available to the reaction and hence slows down the isotropic chemical etch rate(78). It also favours the polymer formation in the passivation steps. This in turn is beneficial for etch selectivity.
- **Platen power:** Increasing the platen power, increases the ion bombardment energy and the related etch(78). However this also increases the mask etching and decreases the selectivity.
- **Plasma power:** Sufficient plasma power is required to ionize the available gases. A higher concentration of reactive species lead to a higher etch rate(78).

- Process pressure: A higher pressure leads to a higher concentration of reactive species and an increased etch rate but can also lead to a reduced etch uniformity(79).

Conclusions and recommendations for the anisotropic etching The main challenge we faced during this step of the fabrication process was that the depth of the larger pre-shapes was not as calculated before the mask was eroded. Variation of factors such as process gas flow, platen bias, process pressure and etch times were tried unsuccessfully. For preservation of the hard mask, process pressure and platen bias, and substrate temperature were varied. A thicker hard mask ($2\mu\text{m}$ Oxide + $1\mu\text{m}$ Nitride) was also applied but increasing it further would not be feasible as it would make patterning the hard mask difficult. Metal masks were considered but would run the risk of resputtering and further complicating the processing(80). One possible solution is to redesign the mask with lower loading. Another possibility is to optimize the the pre-shape opening size for the required depths and a new mask.

A.3. Connecting the pre-shapes. Even though, the required etch depths were not reached, the isotropic etch step of SPAMS was attempted to be optimized in parallel. The challenges and potential solutions associated with the isotropic etch optimization are detailed in this section.

XeF_2 Vapour phase etching The first Isotropic etching steps to connect pre-shapes were performed with the wafer processed by the HARS recipe for 1350 cycles. The Xactix XeF_2 E1 series vapour phase etcher was used for etching with XeF_2 . The wafer was processed at a XeF_2 pressure of 2 Torr in steps of 15 cycles, with each cycle lasting 30 seconds. The entire wafer was loaded into the reaction chamber with sections being removed for cleavage and cross section microscopy after every 15 cycles as shown in Fig 43(a). It was assumed that the decrease in loading due to removal of one section of the wafer would be compensated by the newly formed edges of the wafer that were bare silicon. The vapour phase etching process was carried up to 210 cycles Fig. 43(b-e) before it was concluded that the etch rate is too low with this method. Fig. 43 (f) shows the bigger pre-shapes connecting together, however the smaller pre-shapes forming the channel were not yet connected.

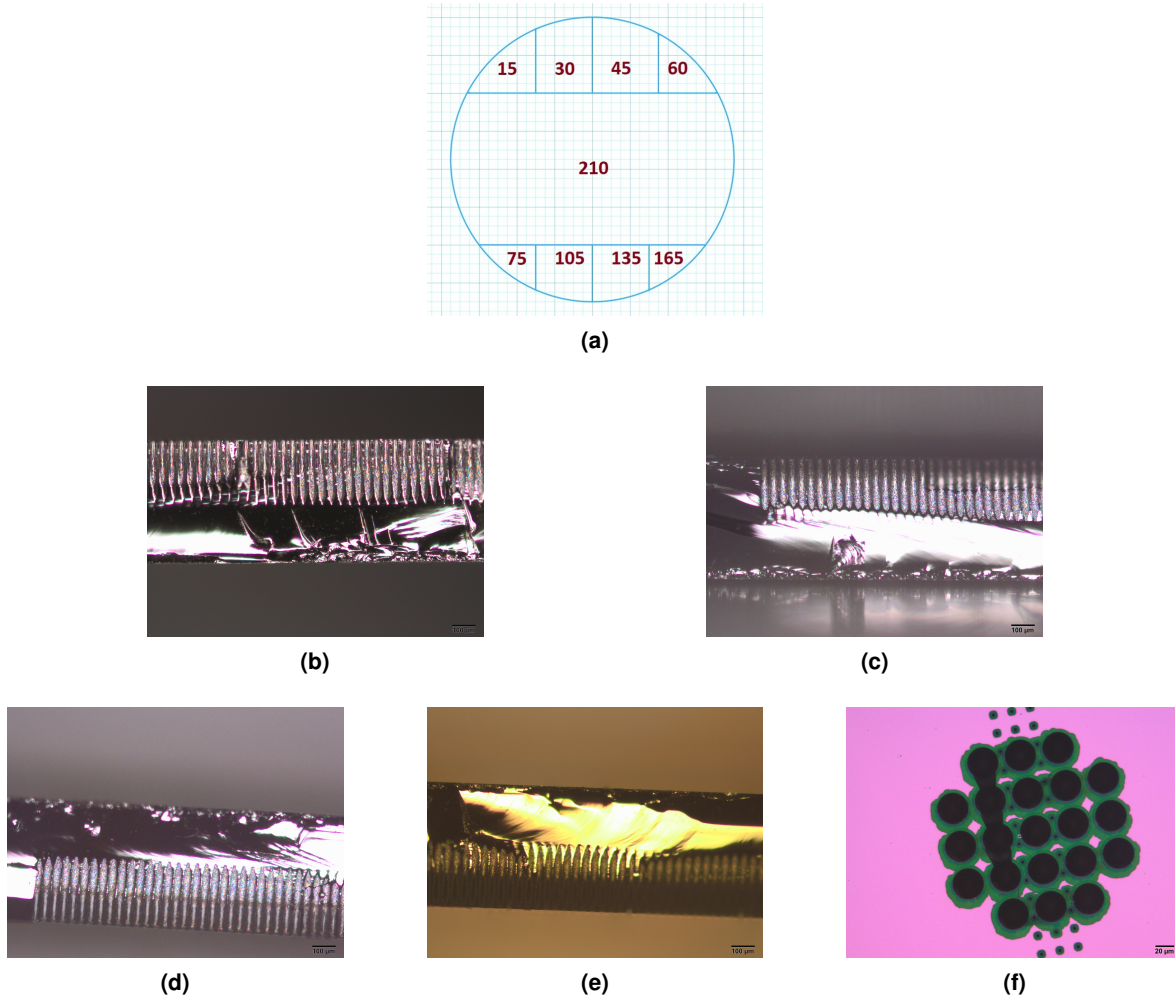


Fig. 43. (a) Schematic showing the number of cycles after which that section was removed and cleaved for a cross section. (b-e) Time series of cross sections showing the slow progression in etching at 15, 75, 135 and 165 cycles respectively. (f) Bigger pre-shapes connecting together but smaller pre-shapes remain disconnected after 135 cycles of XeF_2 etching.

SF_6 Plasma Isotropic etching To enhance the etch rate, a different chemistry was tried with a wafer processed for 1350 cycles of the DRIE HARS recipe. The SPTS-Pegasus etch equipment was used to perform a SF_6 plasma-based isotropic etch(81). As expected, the SF_6 plasma etch was faster. In Fig. 44 we see a 'bubbling effect' in the electrode contact pad area after 1 minute of SF_6 etching. This indicates that the 'walls' of the the pre-shapes have been etched away and the hard mask layer is freestanding. Fig. 44(b) shows the bigger pre-shapes being connected while the smaller pre-shapes are still not connected after 5 minutes of etching due to etch lag. The results of a total of 13 minutes of SF_6 etching are shown in Fig. 44(c) and (d). While in the centre of the chip the connecting channels were etched through, the main feeder channels on the edges of the chip did not connect after 13 minutes. At the contact pad areas the pre-shapes were etched away. In contrast to Fig. 39 (b) the $SiRN$ membrane was visible after 13 minutes of etching in Fig. 44(e). It was also noted that the etch was higher at the centre than at the edges of the wafer. This is visible in the contact pads regions on the edges being incompletely etched where as they are completely etched in the centre as seen in Fig. 44(e).

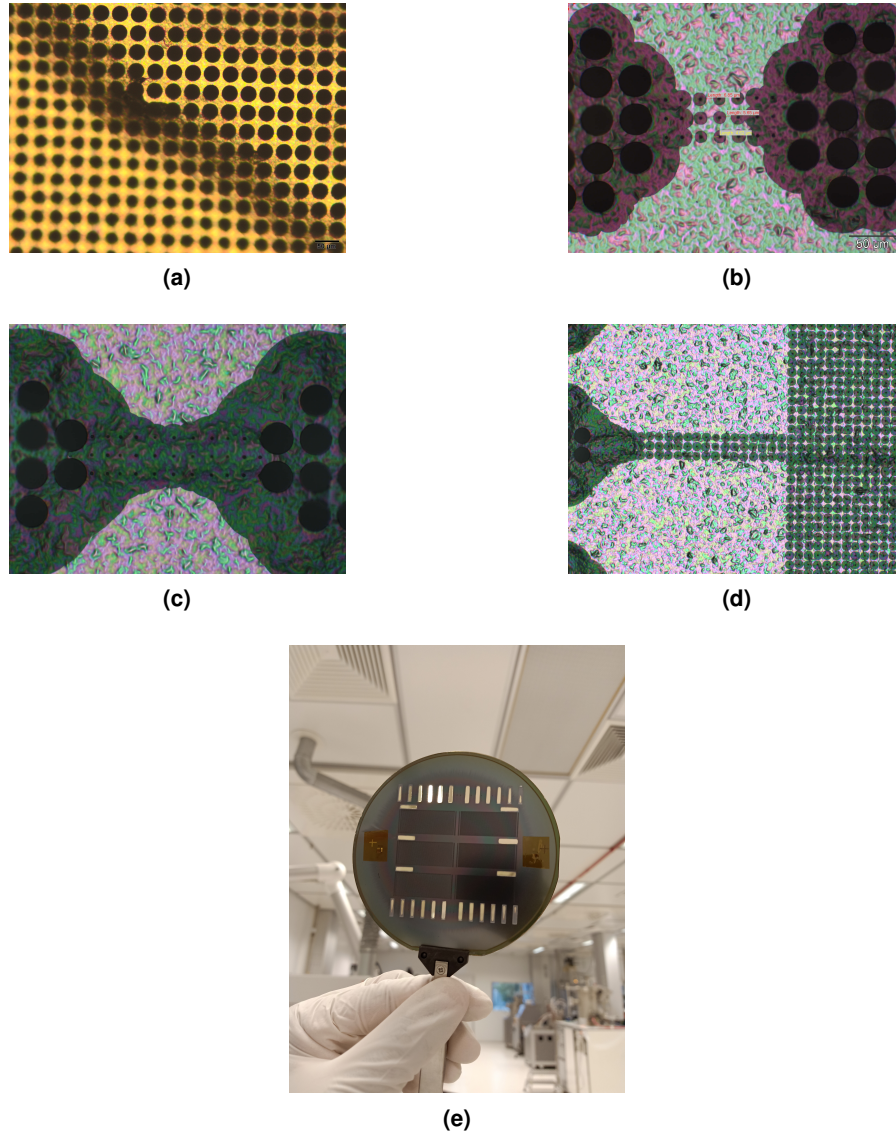


Fig. 44. (a) After 1 minute of SF_6 isotropic etching the contact pad area is hollow and the hard mask is free. (b) The pre-shapes for channels between chambers are not connected after 5 minutes of isotropic etching. After 13 minutes of isotropic etching (c) the channels in between chambers connect while (d) pre-shapes of channels side channels do not connect. (e) Picture showing a wafer level non uniformity in the membrane release witnessed by the partial etching of the rectangular contact pad openings on the edge of the wafer.

To solve the etch lag seen with less etching of the smaller pre-shapes variations were tried with adding oxygen, increasing the pressure and increasing the number of HARS etch cycles for the prior anisotropic etch stage. Fig. 45 (a) shows local etch non-uniformity after 5 minutes of etching with higher process pressures. In Fig. 45 after 15 minutes of isotropic etching (b) we see successful etching of the interconnecting and main channels near the centre but (c) near the edge, the ethanol chambers connect with each other but the side channels do not interconnect. (b) and (c) are on the same wafer with the same processing.

To solve the local etch non-uniformity as seen in Fig. 45(a), the fluorocarbon left by the DRIE step was removed by first ashing for 10 minutes in the Tepla 360M using O_2 and CF_4 plasma, followed by 30 minutes of stripping in Piranha solution. The result was a very uniform undercut etch as seen in Fig. 45(d). However, the etch lag between the different pre-shape sizes persisted.

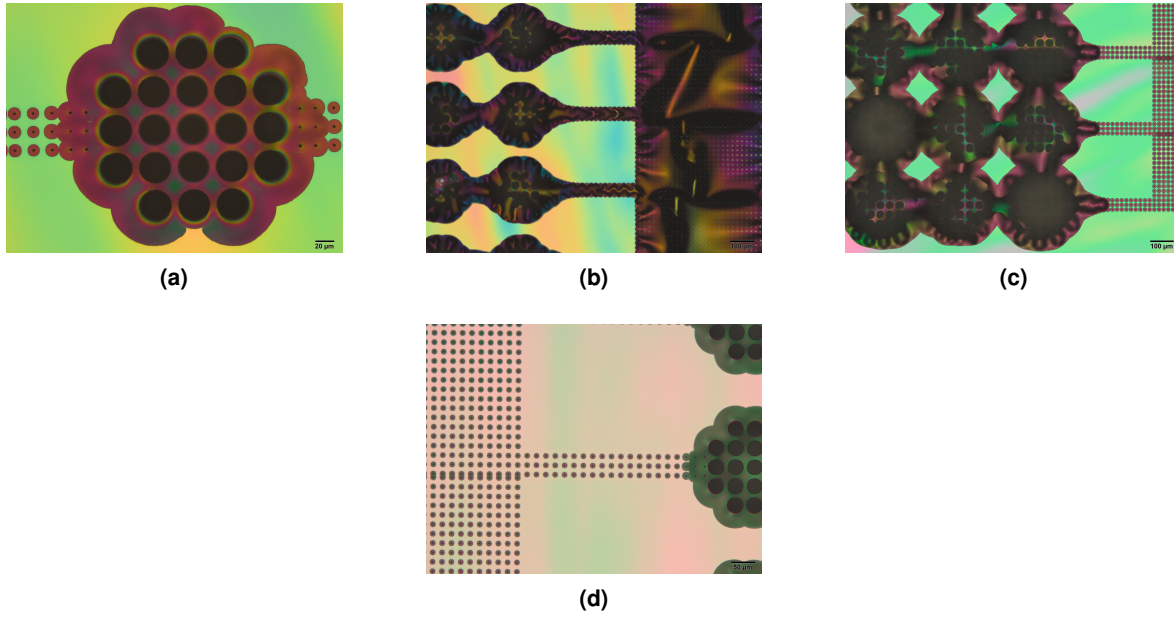


Fig. 45. (a) Occasional non-uniformities in the local undercut etching after 5 minutes of etching in SF_6 at a higher pressure. (b) Side channel pre-shapes interconnecting at the centre of the wafer (c) but not at the edges of the wafer. (d) shows the increase in local etch uniformity in etching for 5 minutes after an additional plasma and piranha cleaning step.

Modified XeF_2 etching SF_6 etching tried before suffered from a lack of wafer level uniformity, as well as lag with etching the smaller holes. This can be attributed to the non-uniformity of the plasma cloud in the SF_6 system. The etch rate in this system would be diffusion limited therefore the SF_6 etch was abandoned.

The Xactix XeF_2 system on the other hand does not have a plasma, and hence has a reaction rate controlled etch. However, the Xactix system is not constant flow, but rather a pulsed system. Therefore a new recipe was tried with a shorter cycle time of 15 seconds per cycle. The pressure of the expansion chamber was also increased to 3 Torr. For these experiments the wafer processed with a $0^\circ C$ etch for 45 minutes at the anisotropic etch step was used. The pre-shapes had an initial depth of 154 and $413\mu m$ for the smaller and larger ones respectively. The fluorocarbon layer was removed similarly using a combination of ashing and Piranha solution. To further reduce the loading on the system the wafer was diced and the test chips were processed one at a time.

At first a test chip was processed for 50 cycles at the above mentioned process parameters. The hard mask on the contact pad region was released (Fig. 46(a)) and both the channel and chamber pre-shapes connected, however the nitride membrane was mostly etched in this process (Fig. 46(c)). The wafer was cleaved to make a cross section and it was noted that $100\mu m$ of etching was required to release the membrane (Fig. 46(b)).

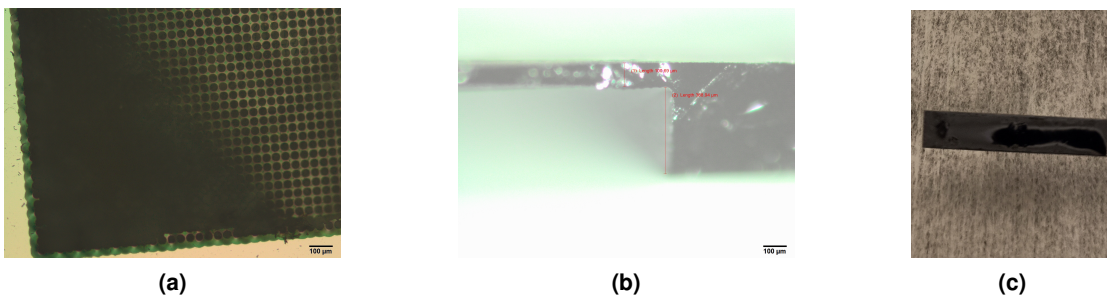


Fig. 46. Results of 50 cycles of high pressure, high frequency XeF_2 etch: (a) hard mask partially falling off in the contact pad region, (b) cross section indicating $100\mu m$ etch is still remaining. (c) Image of the back side of the wafer showing etched away nitride.

To protect the bottom side nitride layer from XeF_2 , the next test chip was fixed on an oxide coated wafer using Olin Oir 907-35 resist. The edges of the wafer were coated with the resist using a cleanroom swab. The wafer and chip were baked to evaporate solvents.

In addition to protecting the backside, the wafer was cleaned in a 2% HF solution to attempt to remove a layer of native silicon dioxide that started forming after the fluorocarbon layer was removed. This step was considered because there was a 14 day

period between the fluorocarbon strip and XeF_2 etch where the native oxide could form.

As expected, the back side nitride layer was protected and like the previous run, the channel and chamber pre-shapes were connected (Fig. 47(a)). The undercut etch at the contact pad area was measured to be $53\mu m$ after 50 cycles of etching (Fig. 47(b)). The wafer was cleaved and found to have a remaining etch depth of $83\mu m$ (Fig. 47(c)).

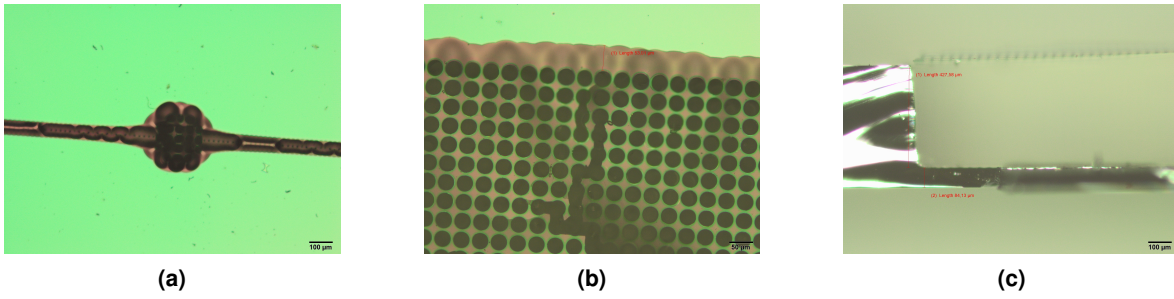


Fig. 47. Results of a second run of 50 cycles of high pressure, high frequency XeF_2 etch: (a) connected pre-shapes forming a single chamber and ethanol channel (b) $53\mu m$ of undercut at the connector pad region. (c) Cross section of chip indicating $83\mu m$ yet to be etched.

It was calculated that to etch an addition $80\mu m$ isotropically, 80 cycles would be required. However the HF cleaning step was skipped and more cycles could be required. Due to the limitation of the number of cycles on the Xactix etch system, first an etch for 100 cycles was performed (Fig. 48 (a)). An undercut of $90\mu m$ was measured at the contact pad region (Fig. 48(b)). This signified that the native oxide strip with HF reduced the etching time by 10 cycles. The etch was continued for a further 40 cycles for a total of 140 cycles to achieve membrane release at the contact pad region (Fig. 48 (e),(g)) and a fluidic channel depth of $450\mu m$ (Fig. 48(f)).

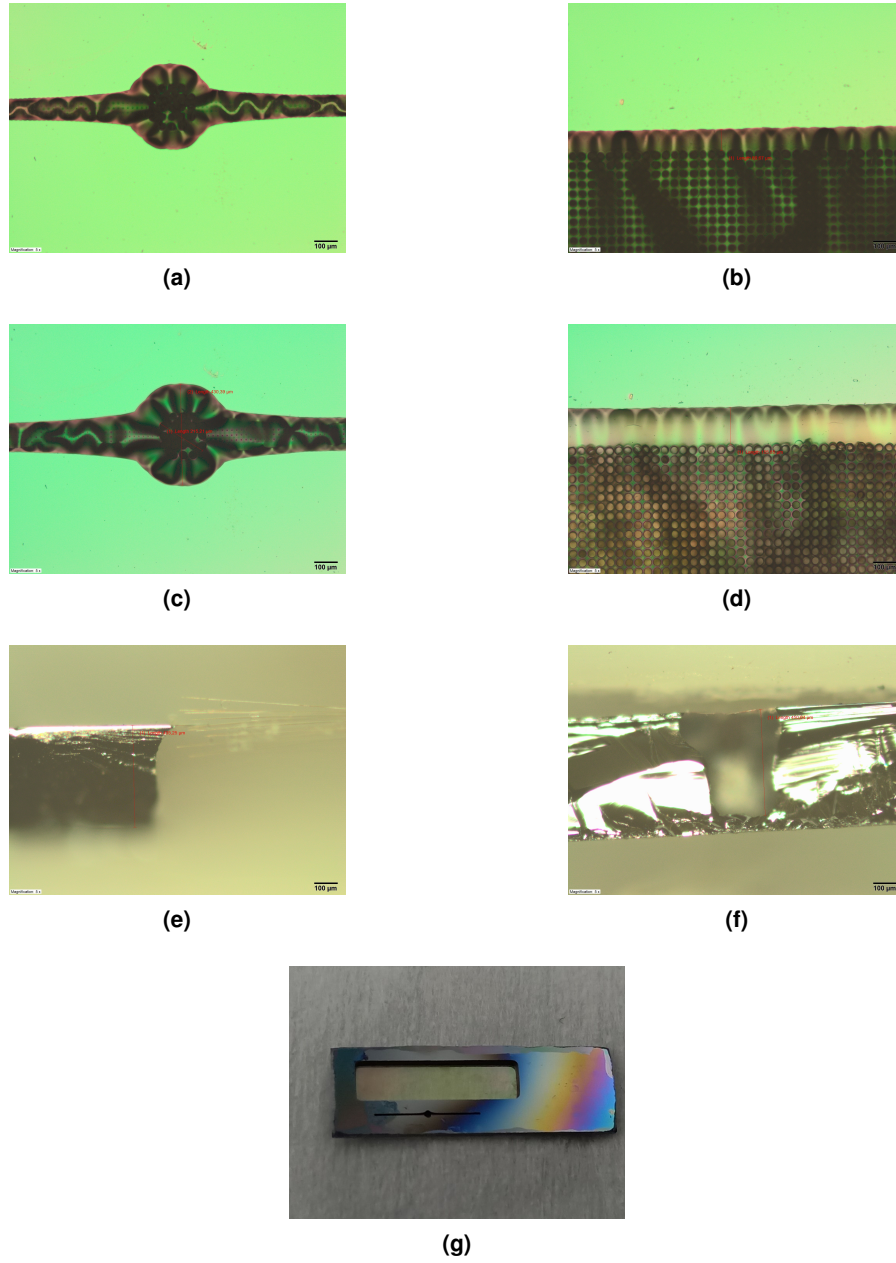


Fig. 48. Results of a second run 100 cycles of XeF_2 etch: (a) connected pre-shapes the chamber and channel (b) $90\mu m$ of undercut at the connector pad region. After 140 cycles of etching under cut at (c) the ethanol chamber measured to be $100\mu m$ radially, (d) at contact pad region measured to be $155\mu m$. Cross section of cleaved chip showing (e) only a thin nitride layer left in the contact pad region, (f) the ethanol connecting channel of depth of $450\mu m$. (g) Image of test chip before cleaving showing the thin transparent membrane.

B. Detailed process flows. The schematic representation of the entire process flow is given below in Fig. 49 and 50. This is followed by the detailed process flows with process parameters.

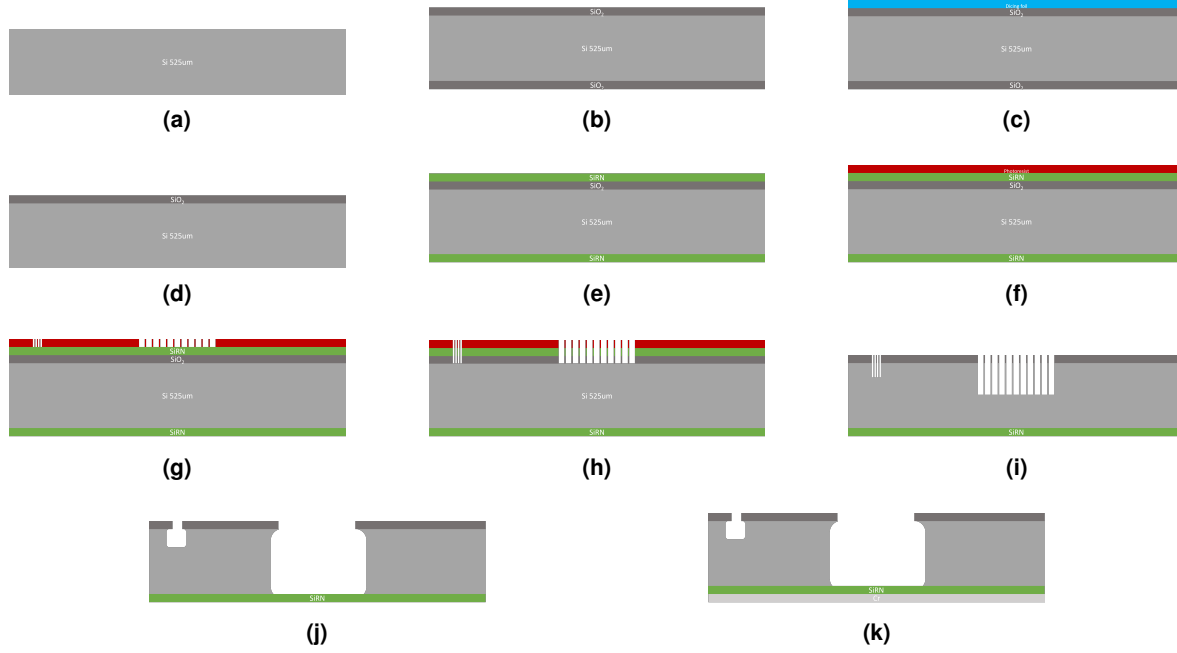


Fig. 49. Process flow of the silicon wafer: (a) Bare silicon wafer (b) 2um of wet oxide grown (c) Dicing foil placed on the bottom side (d) oxide etched on top side, dicing foil removed (e) $1\mu\text{m}$ SiRN grown on both sides (f) Back side coated with photoresist (g) Photolithography defining pre-shapes of different surface areas (h) Patterning of hard mask layers (i) anisotropic DRIE etch with ARDE (j) isotropic dry etch to release membrane (k) [optional] sputtering 10nm of reflective chromium for laser vibrometry experiments. Light grey- silicon, dark grey- silicon dioxide, blue- dicing foil, green- silicon rich nitride, red- photoresist.

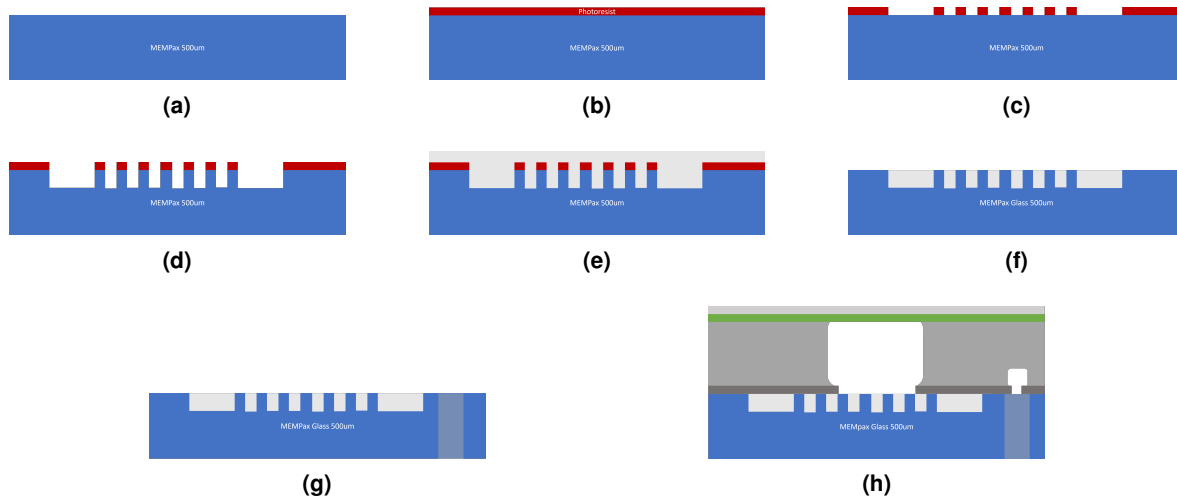


Fig. 50. Process flow of the MEMpax wafer: (a) Bare MEMpax wafer (b) spin coated with photoresist (c) Photolithography defining regions of electrical contacts (d) BHF etch (e) Sputtering 10nm Ta and 150nm Pt (f) liftoff (g) Powder blasting channel inlets and outlets (h) anodic bonding with silicon wafer. Blue- MEMpax, red- photoresist, silver- platinum/tantalum.

Name of process flow:	BubblevalveChamberWaferGlass
Platform:	MEMS
Creation date:	2021-04-13
Personal information	
User name:	Mishra, N.
Email address:	n.mishra@student.utwente.nl
Company/Chair:	Masterstudenten
Function:	Student
Project:	Bubblevalve
Name of supervisor:	Prof Mathieu Odijk
Process planning	
Process start:	
Process end:	
Status	
Name of advisor:	Tiggelaar, R.M.
Last revision:	2021-07-17
Approval:	
Approval date:	
Expiration date:	

ILP: In-line Processing	MFP: Metal-free Processing	UCP: Ultra Clean Processing	Removal of Residues
-------------------------	----------------------------	-----------------------------	---------------------

Step	Level	Process/Basic flow	User comments
------	-------	--------------------	---------------

1	Substrate MEMpax (#subs117)	NL-CLR-Cupboard Diameter: 100mm Thickness: 500µm
---	---------------------------------------	--

clean1002: In-line cleaning (WB16-ILP)

2	ILP	Cleaning in 99% HNO3 (#clean005)	NL-CLR-WB16 BEAKER 1 Purpose: removal of organic traces. Chemical: 99% HNO3 • Time: 5min NOTE: only dry wafers are allowed to enter this beaker in order to prevent dilution of the 99% HNO3!
3	ILP	Cleaning in 99% HNO3 (#clean006)	NL-CLR-WB16 BEAKER 2 Purpose: removal of organic traces. Chemical: 99% HNO3 • Time: 5min
4	ILP	Rinsing (#rinse001)	NL-CLR-WBs QDR Purpose: removal of traces of chemical agents. Choose one of the two rinsing modes: QDR = Quick dump rinsing mode Cascade = Overflow rinsing mode for fragile substrates

5	ILP	Substrate drying (#dry001)	NL-CLR-WBs (ILP) Single substrate drying: 1. Use the single-wafer spinner Settings: 2500 rpm, 60 sec (including 45 sec nitrogen purge) 2. Use the nitrogen gun (fragile wafers or small samples)	
6				Additional 10s of Cleaning in 2% HF + Quick dump rinse to get rid of volatile organic compounds from the box
7				Additional 2 min of cleaning in HNO ₃ (beaker 1) + Quick dump rinse to get rid of Fluoride contamination from previous step

litho1815: Lithography Oir 907-17 using Maximus 804 robot

8	ILP	Priming HMDS (vapor) (#litho602)	NL-CLR-SSE Maximus 804 • Vapor prime HMDS • 140 °C proximity bake
9	ILP	Coating of Olin OiR 907-17 (#litho104)	NL-CLR-SSE MAXIMUS 804 Resist: Olin OiR 907-17 • Program: OiR907-17 4" 4K
10	ILP	Development Oir (#lith112)	NL-CLR-SSE Maximus 804 • Developer: OPD4262 • Program: Maximus 804

etch1208: BHF etch (WB10-private use)

11	ILP	Etching of SiO₂ in BHF (1:7) (#etch125)	NL-CLR-WB09/10 PRIVATE USE BEAKER Chemical: BHF (1:7) • Temperature: room temperature Etch rates: • Thermal SiO ₂ : 60-80nm/min • PECVD SiO ₂ : 125nm/min • LPCVD SiO ₂ : 242 nm/min • Borofloat BF33: 20-25 nm/min • LPCVD Si ₃ N ₄ : 0.64 nm/min	160nm etch rate 20-25nm/min 6:25-8:00 mins
12	ILP	Rinsing (#rinse001)	NL-CLR-WBs QDR Purpose: removal of traces of chemical agents. Choose one of the two rinsing modes: QDR = Quick dump rinsing mode Cascade = Overflow rinsing mode for fragile substrates Rinse until message 'End of rinsing process' is shown on the touchscreen of the QDR, else repeat the rinsing process.	

NL-CLR-WBs (ILP)

NL-CLR-WDS (ILP)

13

ILP

Substrate drying
(#dry001)

Single substrate drying:

1. Use the single-wafer spinner
Settings: 2500 rpm, 60 sec (including 45 sec nitrogen purge)
2. Use the nitrogen gun (fragile wafers or small samples)

14

ILP

Step height measurement
(#metro500)**NL-CLR-Veeco Dektak 8**

Settings:

- Stylus force: 5.00mg
- Duration: 60sec
- Profile: Hills and Valleys

Please mention the scan length, meas range and the results of the depth measurement in the user comment.

Measure step height of trenches formed by BHF etch. Etch more until desired depth of 160nm is achieved.

film1632: Sputtering of Tantalum (TCOathy)

15

ILP

Sample preparation
(#film631)**NL-CLR-T'COathy**

Purpose: reduce outgassing and pump time.

- Use a dehydration bake (120°C, 5 mins) in WB22 after wet processing.
- Use only Kapton tape for fixing samples on a carrier wafer or a shadow mask* on a process wafer.

*TCO is the preferred supplier of shadow masks.

16

ILP

Sputter rate verification
(#film632)**NL-CLR-T'COathy**

Purpose: optional step to determine the sputter rate with the Woollam Ellipsometer. One material per wafer!

Use the standard process parameters underneath or calibrate according to the process parameters when using other pressure / power settings.

Layer	Target	Power (W)	Pre-time	Proc-time	P (x10-3) mbar
1	Au	200	1:00	0:30	6.6
1	Pt	200	1:00	1:00	6.6
1	Cr	200	1:00	2:00	6.6
1	Ta	200	1:00	2:00	6.6
1	Ti	200	1:00	2:00	6.6

- Follow calibration instructions in the equipment manual!

17

ILP

Sputtering of Ta
(#film635)**NL-CLR-T'COathy**

Application: deposition of Tantalum

- Base pressure: <1.0E-6 mbar

Layer	Target	Power (W)	Pre-time	Proc-time	P (x10-3) mbar
	Ta	200	1:00	...	6.6

- Estimated deposition rate ~ 10 nm/min

Desired thickness: 10nm
Approximate rate: 10 nm/min
Time: 1min

film1634: Sputtering of Platinum (TCOathy)

18

ILP

Sample preparation
(#film631)**NL-CLR-T'COathy**

Purpose: reduce outgassing and pump time.

- Use a dehydration bake (120°C, 5 mins) in WB22 after wet processing.

- Use only Kapton tape for fixing samples on a carrier wafer or a shadow mask* on a process wafer.

*TCO is the preferred supplier of shadow masks.

19 ILP

Sputter rate verification (#film632)

NL-CLR-T'COathy

Purpose: optional step to determine the sputter rate with the Woollam Ellipsometer. One material per wafer!

Use the standard process parameters underneath or calibrate according to the process parameters when using other pressure / power settings.

Layer	Target	Power (W)	Pre-time	Proc-time	P (x10-3) mbar
1	Au	200	1:00	0:30	6.6
1	Pt	200	1:00	1:00	6.6
1	Cr	200	1:00	2:00	6.6
1	Ta	200	1:00	2:00	6.6
1	Ti	200	1:00	2:00	6.6

- Follow calibration instructions in the equipment manual!

20 ILP

Sputtering of Pt (#film637)

NL-CLR-T'COathy

Application: deposition of Platinum

- Base pressure: <1.0E-6 mbar

Desired thickness:
150nm
Approximate rate:
20 nm/min
Time: 7.5 min

Layer	Target	Power (W)	Pre-time	Proc-time	P (x10-3) mbar
	Pt	200	0:30	...	6.6

- Estimated deposition rate ~ 20 nm/min

litho1500: Lift-Off with postive resists (WB11)

21 ILP

Lift-Off (#litho500)

NL-CLR-WB11 ULTRASONIC BATH

Purpose: removal of resist and excess metal from the surface of the substrate by ultrasonication in Acetone.

- Beaker 1: Acetone
- Time = 10 min

Single wafer processing:

Spray the wafer with Acetone for 30 sec and immediately spray with isopropanol (IPA) for 30 sec.

Batch wafer processing:

- Beaker 2: Acetone
- Time = 10 min
- Beaker 3: Isopropanol
- Time = 10 min

22 ILP

Substrate drying (#dry001)

NL-CLR-WBs (ILP)

Single substrate drying:

1. Use the single-wafer spinner
Settings: 2500 rpm, 60 sec (including 45 sec nitrogen purge)
2. Use the nitrogen gun (fragile wafers or small samples)

23 ILP

Inspection by Optical Microscopy (#metro102)

NL-CLR-Optical Microscopes

Use one of the Olympus microscopes for inspection.

24

ILP

Step height measurement NL-CLR-Veeco Dektak 8 (#metro500)

Settings:

- Stylus force: 5.00mg
- Duration: 60sec
- Profile: Hills and Valleys

Please mention the scan length, meas range and the results of the depth measurement in the user comment.

Measure to make sure that trenches are filled with the sputtered metals

25

Dry film resist lithography and exposure

1)Applying the film
 -Place a piece of Ordyl BF410 foil and the wafer between two sheets of cleanroom paper.
 -The inside surface of foil is the adhesive side.
 Use the curve on the foil as a guide.
 -Using the ABC 3500 pro series laminator at 70c at speed number 2 laminate the wafer with the resist
 -cut the excess resist using a snap off blade as close to the wafer as possible
 2)Exposure
 -Using the EVG 620, with hard contact, constant time, align expose for 4s via the powder blast mask
 3)Transport the samples in 3 individual wafer boxes to the BIOS labs.
 3)Development (At the BIOS lab)
 -Remove the protective transparent layer from the foil.
 -Spin at 500RPM and spray with hot 45c running water for 100s using the spin 150 tool.
 Polymerized parts of the resist will

26

turn lighter when developed.
-Spin dry for 30s, followed by drying by pressurized N₂. Finally dry on a hotplate at 60c. The foil turns dark blue when dry.

-Check the alignment under a microscope.

Powder blasting and removal of resist

- Store all wafers in a separate box for transport
- Powder blast using Imerys Fused Minerals Treibacher Alodur (~39um Al₂O₃ particles) at a container pressure of 5.5 bar at a mass flow rate of 0.2g/s, scan rate of 10 mm/s and step size of 0.5mm
- Confirm the opening of the powder blasted holes by visual inspection under a microscope.
- Remove the dry film resist by submerging wafers in a 1% solution of Sodium Bicarbonate at 50c for 3.5h.
- Rinse and dry the wafers
- Carry the wafers back in a clean box to the nanolab cleanroom
- Particle clean in the nanolab

Name of process flow:	BubblevalveChamberWaferSi
Platform:	MEMS
Creation date:	2021-04-12
Personal information	
User name:	Mishra, N.
Email address:	n.mishra@student.utwente.nl
Company/Chair:	Masterstudenten
Function:	Student
Project:	Bubble Valve
Name of supervisor:	Prof Mathieu Odijk
Process planning	
Process start:	
Process end:	
Status	
Name of advisor:	Tiggelaar, R.M.
Last revision:	2021-07-25
Approval:	
Approval date:	
Expiration date:	

ILP: In-line Processing	MFP: Metal-free Processing	UCP: Ultra Clean Processing	Removal of Residues
-------------------------	----------------------------	-----------------------------	---------------------

Step	Level	Process/Basic flow	User comments
------	-------	--------------------	---------------

1		Substrate Silicon (#subs102) NL-CLR-Wafer Storage Cupboard Orientation: <100> Diameter: 100mm Thickness: 525µm +/- 25µm Polished: Double side (DSP) Resistivity: 5-10Ωcm Type: p/boron	
---	--	---	--

clean1000: Pre-furnace cleaning (WB14-MFP)

2	MFP	Cleaning in 99% HNO₃ (#clean001) NL-CLR-WB14 BEAKER 1 Purpose: removal of organic traces. Chemical: 99% HNO ₃ • Time: 5min NOTE: only dry wafers are allowed to enter this beaker in order to prevent dilution of the 99% HNO ₃ !	
3	MFP	Cleaning in 99% HNO₃ (#clean002) NL-CLR-WB14 BEAKER 2 Purpose: removal of organic traces. Chemical: 99% HNO ₃ • Time: 5min	
4	MFP	Rinsing (#rinse002) NL-CLR-WBs QDR Purpose: removal of traces of chemical agents. Choose one of the two rinsing modes: QDR = Quick dump rinsing mode Cascade = Overflow rinsing mode for fragile substrates Rinse until message 'End of rinsing process' is shown on the touchscreen of the QDR, else repeat the rinsing process.	
5	MFP	Cleaning in 69% HNO₃ NL-CR-WB14 BEAKER 3A/3B	

		at 95 °C (#clean003)	<p>Purpose: removal of metallic traces. Chemical: 69% HNO₃</p> <ul style="list-style-type: none"> • Temperature: 95°C • Time: 10min
6	MFP	Rinsing (#rinse002)	<p>NL-CLR-WBs QDR Purpose: removal of traces of chemical agents.</p> <p>Choose one of the two rinsing modes: QDR = Quick dump rinsing mode Cascade = Overflow rinsing mode for fragile substrates</p> <p>Rinse until message 'End of rinsing process' is shown on the touchscreen of the QDR, else repeat the rinsing process.</p>
7	MFP	Substrate drying (WB14) (#dry022)	<p>NL-CLR-WB14 Optional drying step. After the QDR, you can transfer your substrates directly to a Teflon carrier and strip the native SiO₂ in 1% HF (WB15).</p> <p>NOTE: load your wafers within 4 hours after cleaning!</p> <p>Single substrate drying:</p> <ol style="list-style-type: none"> 1. Use the single-wafer spinner Settings: 2500 rpm, 60 sec (including 45 sec nitrogen purge). 2. Use the nitrogen gun (fragile wafers or small samples). <p>Batch drying of substrates: Use the Semitool for drying up to 25 substrates at once.</p>
8	MFP	Etching in 1% HF (#etch127)	<p>NL-CLR-WB15 1% HF BEAKER Purpose: remove native SiO₂ from Silicon. Chemical: 1% HF</p> <ul style="list-style-type: none"> • Temperature: room temperature • Time: 1min <p>Optional etching step. This step is obligatory for the MESA+ monitor wafer.</p>
9	MFP	Rinsing (#rinse002)	<p>NL-CLR-WBs QDR Purpose: removal of traces of chemical agents.</p> <p>Choose one of the two rinsing modes: QDR = Quick dump rinsing mode Cascade = Overflow rinsing mode for fragile substrates</p> <p>Rinse until message 'End of rinsing process' is shown on the touchscreen of the QDR, else repeat the rinsing process.</p>
10	MFP	Substrate drying (WB15) (#dry023)	<p>NL-CLR-WB15</p> <p>NOTE: load your wafers within 4 hours after cleaning!</p> <p>Single substrate drying:</p> <ol style="list-style-type: none"> 1. Use the single-wafer spinner Settings: 2500 rpm, 60 sec (including 45 sec nitrogen purge). 2. Use the nitrogen gun (fragile wafers or small samples). <p>Batch drying of substrates: Use the Semitool for drying up to 25 substrates at once.</p>

film1903: Wet Oxidation of Silicon or polySi (A3)

11	MFP	Cleaning in 99% HNO₃ (#clean001)	<p>NL-CLR-WB14 BEAKER 1 Purpose: removal of organic traces. Chemical: 99% HNO₃</p> <ul style="list-style-type: none"> • Time: 5min <p>NOTE: only dry wafers are allowed to enter this beaker in order to prevent dilution of the 99% HNO₃!</p>
12	MFP	Cleaning in 99% HNO₃ (#clean002)	<p>NL-CLR-WB14 BEAKER 2 Purpose: removal of organic traces. Chemical: 99% HNO₃</p>

			<ul style="list-style-type: none"> • Time: 5min
13	MFP	Rinsing (#rinse002)	<p>NL-CLR-WBs QDR Purpose: removal of traces of chemical agents.</p> <p>Choose one of the two rinsing modes: QDR = Quick dump rinsing mode Cascade = Overflow rinsing mode for fragile substrates</p> <p>Rinse until message 'End of rinsing process' is shown on the touchscreen of the QDR, else repeat the rinsing process.</p>
14	MFP	Cleaning in 69% HNO3 at 95 °C (#clean003)	<p>NL-CR-WB14 BEAKER 3A/3B Purpose: removal of metallic traces. Chemical: 69% HNO3</p> <ul style="list-style-type: none"> • Temperature: 95°C • Time: 10min
15	MFP	Rinsing (#rinse002)	<p>NL-CLR-WBs QDR Purpose: removal of traces of chemical agents.</p> <p>Choose one of the two rinsing modes: QDR = Quick dump rinsing mode Cascade = Overflow rinsing mode for fragile substrates</p> <p>Rinse until message 'End of rinsing process' is shown on the touchscreen of the QDR, else repeat the rinsing process.</p>
16	MFP	Substrate drying (WB14) (#dry022)	<p>NL-CLR-WB14 Optional drying step. After the QDR, you can transfer your substrates directly to a Teflon carrier and strip the native SiO2 in 1% HF (WB15).</p> <p>NOTE: load your wafers within 4 hours after cleaning!</p> <p>Single substrate drying: 1. Use the single-wafer spinner Settings: 2500 rpm, 60 sec (including 45 sec nitrogen purge). 2. Use the nitrogen gun (fragile wafers or small samples).</p> <p>Batch drying of substrates: Use the Semitool for drying up to 25 substrates at once.</p>
17	MFP	Etching in 1% HF (#etch127)	<p>NL-CLR-WB15 1% HF BEAKER Purpose: remove native SiO2 from Silicon. Chemical: 1% HF</p> <ul style="list-style-type: none"> • Temperature: room temperature • Time: 1min <p>Optional etching step. This step is obligatory for the MESA+ monitor wafer.</p>
18	MFP	Rinsing (#rinse002)	<p>NL-CLR-WBs QDR Purpose: removal of traces of chemical agents.</p> <p>Choose one of the two rinsing modes: QDR = Quick dump rinsing mode Cascade = Overflow rinsing mode for fragile substrates</p> <p>Rinse until message 'End of rinsing process' is shown on the touchscreen of the QDR, else repeat the rinsing process.</p>
19	MFP	Substrate drying (WB15) (#dry023)	<p>NL-CLR-WB15</p> <p>NOTE: load your wafers within 4 hours after cleaning!</p> <p>Single substrate drying: 1. Use the single-wafer spinner Settings: 2500 rpm, 60 sec (including 45 sec nitrogen purge). 2. Use the nitrogen gun (fragile wafers or small samples).</p> <p>Batch drying of substrates: Use the Semitool for drying up to 25 substrates at once.</p>
			NL-CLR-A3 FURNACE

20	MFP	Wet Oxidation of Silicon or polySi (MFP) (#film903)	<p>Application: wet oxidation of Silicon or polySi. Programs: WET750, WET800, WET900, WET1000, WET1150</p> <p>Settings:</p> <ul style="list-style-type: none"> • Standby temperature: 700°C • Temperature range: 750-1150°C • O₂ flow: 4slm • Ramp: 10°C/min <p>Please mention the following settings in the User Comments:</p> <ul style="list-style-type: none"> • Program: • Target thickness: nm • Time:min 	<p>Target thickness: 2 um Temperature: 1150c Time: 15h B2 furnace</p>
21	ILP	Particle inspection (#metro201)	<p>NL-CLR-COLD LIGHT SOURCE (SEM ROOM)</p> <p>Shine light onto the surface at an angle in a dark room to check for particles, haze and scratches in the coating(s) on the substrate. Please warn the administrator in case a coating from one of the furnaces contains (a lot of) particles!</p> <p>Contact Christaan Bruinink for questions.</p>	
22	ILP	Layer thickness measurement (#metro401)	<p>NL-CLR-WOOLLAM-2000UI ELLIPSOMETER</p> <p>Consult the user manual to perform a single point or a raster measurement. Use one of the available optical models to determine the layer thickness and optical constants of the coating on your substrate. Provide the following results in the digital logbook: thickness, refractive index (n) at 632.8nm and the nonuniformity of the layer (%range) of a 5-point scan.</p>	
23				<p>-Cover the wafer with Nitto dicing foil on top to protect oxide on one side from etching in the next step -Heat to 75c for 1 min to make sure that the foil sticks to the wafer -cut the excess dicing foil</p>
etch1207: Etching in BHF (WB06 - ILP)				
24	ILP	Etching in BHF (#etch117)	<p>NL-CLR-WB06 Use dedicated beaker BHF (1:7) Temp.: Room temperature</p> <p>Etch rates: Thermal SiO₂:60-80 nm/min PECVD SiO₂:125 nm/min</p>	<p>Etch SiO₂ on bottom side</p> <p>Thickness to be etched: 1um etch rate: 60-80 nm/min time:12:30 to 16:40</p>
25	ILP	Rinsing (#rinse001)	<p>NL-CLR-WBs QDR Purpose: removal of traces of chemical agents.</p> <p>Choose one of the two rinsing modes: QDR = Quick dump rinsing mode Cascade = Overflow rinsing mode for fragile substrates</p> <p>Rinse until message 'End of rinsing process' is shown on the touchscreen of the QDR, else repeat the rinsing process.</p>	
26	ILP	Substrate drying (#dry001)	<p>NL-CLR-WBs (ILP)</p> <p>Single substrate drying:</p>	

1. Use the single-wafer spinner
Settings: 2500 rpm, 60 sec (including 45 sec nitrogen purge)
2. Use the nitrogen gun (fragile wafers or small samples)

27

Remove
Dicing foil**film1205: LPCVD of low-stress SiRN (G3-50 MPa)**

28	MFP	System monitoring (#spc001)	NL-CLR-FURNACES Purpose: monitoring the stability of the furnaces in terms of deposition rate, non-uniformity and optical parameters. Procedure: 1. Take a Silicon wafer from the wafer box with monitor wafers 2. Fill in the digital logbook and write down the last 4 digits of the waferID in the User Comment 3. Write down the run number on the lid of the waferbox
29	MFP	Cleaning in 99% HNO3 (#clean001)	NL-CLR-WB14 BEAKER 1 Purpose: removal of organic traces. Chemical: 99% HNO3 • Time: 5min NOTE: only dry wafers are allowed to enter this beaker in order to prevent dilution of the 99% HNO3!
30	MFP	Cleaning in 99% HNO3 (#clean002)	NL-CLR-WB14 BEAKER 2 Purpose: removal of organic traces. Chemical: 99% HNO3 • Time: 5min
31	MFP	Rinsing (#rinse002)	NL-CLR-WBs QDR Purpose: removal of traces of chemical agents. Choose one of the two rinsing modes: QDR = Quick dump rinsing mode Cascade = Overflow rinsing mode for fragile substrates Rinse until message 'End of rinsing process' is shown on the touchscreen of the QDR, else repeat the rinsing process.
32	MFP	Cleaning in 69% HNO3 at 95 °C (#clean003)	NL-CR-WB14 BEAKER 3A/3B Purpose: removal of metallic traces. Chemical: 69% HNO3 • Temperature: 95°C • Time: 10min
33	MFP	Rinsing (#rinse002)	NL-CLR-WBs QDR Purpose: removal of traces of chemical agents. Choose one of the two rinsing modes: QDR = Quick dump rinsing mode Cascade = Overflow rinsing mode for fragile substrates Rinse until message 'End of rinsing process' is shown on the touchscreen of the QDR, else repeat the rinsing process.
34	MFP	Substrate drying (WB14) (#dry022)	NL-CLR-WB14 Optional drying step. After the QDR, you can transfer your substrates directly to a Teflon carrier and strip the native SiO2 in 1% HF (WB15). NOTE: load your wafers within 4 hours after cleaning! Single substrate drying: 1. Use the single-wafer spinner Settings: 2500 rpm, 60 sec (including 45 sec nitrogen purge). 2. Use the nitrogen gun (fragile wafers or small samples). Batch drying of substrates: Use the Semitool for drying up to 25 substrates at once.
35	MFP	Etching in 1% HF	NL-CLR-WB15 1% HF BEAKER

		(#etch127)	<p>Purpose: remove native SiO₂ from Silicon. Chemical: 1% HF</p> <ul style="list-style-type: none"> • Temperature: room temperature • Time: 1min <p>Optional etching step. This step is obligatory for the MESA+ monitor wafer.</p>	
36	MFP	Rinsing (#rinse002)	<p>NL-CLR-WBs QDR Purpose: removal of traces of chemical agents.</p> <p>Choose one of the two rinsing modes: QDR = Quick dump rinsing mode Cascade = Overflow rinsing mode for fragile substrates</p> <p>Rinse until message 'End of rinsing process' is shown on the touchscreen of the QDR, else repeat the rinsing process.</p>	
37	MFP	Substrate drying (WB15) (#dry023)	<p>NL-CLR-WB15</p> <p>NOTE: load your wafers within 4 hours after cleaning!</p> <p>Single substrate drying:</p> <ol style="list-style-type: none"> 1. Use the single-wafer spinner Settings: 2500 rpm, 60 sec (including 45 sec nitrogen purge). 2. Use the nitrogen gun (fragile wafers or small samples). <p>Batch drying of substrates: Use the Semitool for drying up to 25 substrates at once.</p>	
38	MFP	Loading of wafers (#film217)	<p>NL-CLR-LPCVD FURNACES Program: UN-/LOAD</p> <p>RESTRICTION: the maximum loading capacity of process wafers is 25 (excl. the boat fillers).</p> <p>Procedure:</p> <ol style="list-style-type: none"> 1. Start the UN-/LOAD program after cleaning 2. Let the filler wafers cool down for 5 minutes 3. Load your wafers within 30 minutes 4. Place the monitor wafer in the center of the wafer carrier 5. Always use a full wafer load 	
39	MFP	LPCVD of Si₃N₄ (50 MPa) (#film205)	<p>NL-CLR-G3 FURNACE Application: deposition of low-stress Silicon Nitride. Program: SIRN04</p> <p>RESTRICTION: maximum thickness is 1.6µm.</p> <p>Settings:</p> <ul style="list-style-type: none"> • Temperature: 820°C (zone 1), 850°C (zone 2), 870°C (zone 3) • Pressure: 150mTorr • SiH₂Cl₂ flow: 72sccm • NH₃ flow: 22sccm • N₂ low: 150sccm <p>Please mention the following settings in the User Comments:</p> <ul style="list-style-type: none"> • Target thickness: nm • Time:min 	<p>Target thickness: 1µm</p> <p>NB: Grows on both sides</p>
40	ILP	Particle inspection (#metro201)	<p>NL-CLR-COLD LIGHT SOURCE (SEM ROOM)</p> <p>Shine light onto the surface at an angle in a dark room to check for particles, haze and scratches in the coating(s) on the substrate. Please warn the administrator in case a coating from one of the furnaces contains (a lot of) particles!</p> <p>Contact Christaan Bruinink for questions.</p>	
41	ILP	Layer thickness measurement (#metro401)	<p>NL-CLR-WOOLLAM-2000UI ELLIPSOMETER</p> <p>Consult the user manual to perform a single point or a raster measurement. Use one of the available optical models to determine the layer thickness and optical constants of the coating on your substrate. Provide the following results in the digital logbook: thickness, refractive index (n) at 632.8nm and the nonuniformity of the layer (%range) of a 5-point scan.</p>	

42	ILP	Layer thickness measurement (#metro401)	NL-CLR-WOOLLAM-2000UI ELLIPSOMETER Consult the user manual to perform a single point or a raster measurement. Use one of the available optical models to determine the layer thickness and optical constants of the coating on your substrate. Provide the following results in the digital logbook: thickness, refractive index (n) at 632.8nm and the nonuniformity of the layer (%range) of a 5-point scan.	
litho1802: Lithography of Olin Oir 908-35 (positive resist - ILP)				
43	ILP	HMDS priming (#litho600)	OPTION 1 Liquid HMDS priming NL-CLR-WB21/22 HOTPLATE Purpose: dehydration bake Settings: • Temperature: 120°C • Time: 5min After the dehydration bake, perform the liquid priming with minimum delay! NL-CLR-WB21 Primus SB15 Spinner Primer: HexaMethylDiSilazane (HMDS) Settings: • Spin mode: static • Spin speed: 4000rpm • Spin time: 30s OPTION 2 Vapor HMDS priming NL-CLR-WB28 Lab-line Duo-Vac Oven Primer: HexaMethylDiSilazane (HMDS) Settings: • Temperature: 150°C • Pressure: 25inHg • Dehydration bake: 2min • HMDS priming: 5min CAUTION: let the substrates cool down before handling with your tweezer!	
44	ILP	Coating of Olin OiR 908-35 (#litho102)	NL-CLR-WB21 PRIMUS SB15 SPINNER Resist: Olin OiR 908-35 Spin program: 4000 Settings: • Spin mode: static • Spin speed: 4000rpm • Spin time: 30s	
45	ILP	Prebake of Olin OiR 908-35 (#litho004)	NL-CLR-WB21 PREBAKE HOTPLATE Purpose: removal of residual solvent from the resist film after spin coating. Settings: • Temperature: 95°C • Time: 120s	
46	ILP	Alignment & exposure of Olin OiR 908-35 (#litho302)	NL-CLR-EV620 AND 6200NT MASK ALIGNERS Settings: • Separation: 50µm • Contact mode: proximity/soft contact/hard contact/vacuum contact • Exposure mode: constant time/.../... • Exposure time: 9sec This exposure time is based on the Hg lamp with a power of 12mW/cm2. Settings:(EVG6200NT) • Separation: 50µm • Contact mode: proximity/soft contact/hard contact/vacuum contact • Exposure mode: UV-LED GHI-line 204 mJ/cm2 • Exposure setting needs to be optimized for optimal result, depending on structures on the mask!	exposure time = 12s

This exposure is based on UV-LED light source.

47	ILP	After exposure bake of Olin OiR resists (#litho005)	NL-CLR-WB21 POSTBAKE HOTPLATE Purpose: Settings: • Temperature: 120°C • Time: 60s
48	ILP	Development of Olin OiR resists (#litho200)	NL-CLR-WB21 DEVELOPMENT BEAKERS Developer: OPD4262 • Beaker 1: 30sec • Beaker 2: 15-30sec
49	ILP	Rinsing (#rinse001)	NL-CLR-WBs QDR Purpose: removal of traces of chemical agents. Choose one of the two rinsing modes: QDR = Quick dump rinsing mode Cascade = Overflow rinsing mode for fragile substrates Rinse until message 'End of rinsing process' is shown on the touchscreen of the QDR, else repeat the rinsing process.
50	ILP	Substrate drying (#dry001)	NL-CLR-WBs (ILP) Single substrate drying: 1. Use the single-wafer spinner Settings: 2500 rpm, 60 sec (including 45 sec nitrogen purge) 2. Use the nitrogen gun (fragile wafers or small samples)
51	ILP	Postbake of Olin OiR resists (#litho008)	NL-CLR-WB21 POSTBAKE HOTPLATE Purpose: Settings: • Temperature: 120°C • Time: 10min
52	ILP	Inspection by Optical Microscopy (#metro101)	NL-CLR-Nikon Microscope Use the Nikon microscope for inspection.

etch1731: Etching of thin nitrides, oxides and shallow Si by CHF₃/O₂ Plasma (TEtske)

53	ILP	Chamber clean (TEtske) (#etch198)	NL-CLR-TEtske Application: removal of organic and fluorocarbon residues on the chamber wall. Select the correct etch chamber and electrode for your etch process (see next step). • Electrode temperature: 10°C • Valve position: 15% (resulting in a pressure of ~42mTorr) • O ₂ flow: 50sccm • Power: 100Watt • Time: 10 min • Load: 54% • Tune: 23% The etch chamber is clean at the moment the plasma color is white and the DC bias is >500V.	Etch SiRN + SiO ₂ on top side
54	ILP	RIE with CHF₃/O₂ Plasma (#etch193)	NL-CLR-TEtske Application: plasma etching of thin layers of various oxides and nitrides, shallow etching (nm) in Silicon and pre-conditioning for XeF ₂ etching. Use Kapton tape or Kapton foil to protect the edge of the wafer and therefore avoid damage during processing in KOH or TMAH. Select the dirty chamber and the styros electrode. • Electrode temperature: 10°C • Pressure: 10mTorr • CHF ₃ flow: 25sccm	SiRN thickness = 1µm Etch rate = 60nm/min SiO ₂ thickness = 2µm Etch rate = 30 nm/min

- O2 flow: 5sccm
- Power: 60Watt
- DC bias: -500 up to - 540Volt

Etch rate SiRN (G3-SiRN): 60 nm/min
 Etch rate SiO2: 30 nm/min
 Etch rate Si: 15-25 nm/min
 Etch rate Olin OiR resists: 50 nm/min

total etch
time for both
layers= 01:22
(hh:mm)

check
endpoint by
visual
inspection at
features on
edges. SiO2
mask is
darker than
bare Si.

55

ILP

Stripping of Resists (#strip100)

NL-CLR-TePla300

Application: stripping of resists by O2 plasma after plasma etching.

skipped

PLEASE NOTE

- 1. RESTRICTION:** do not strip resists on chromium in the TePla300, but instead use the TePla360 (choose: recipe 041).
- 2. BACKUP:** TePla300 down? Contact the administrator if you can continue your processing in the TePla360.

Step	O2 (sccm)	N2 (sccm)	P (mbar)	Power (W)	Time (h:mm:ss)
Preheating	0	500	1.0	800	0:10:00
Stripping of resist	500	0	1.0	800	*

* Select one of the following recipes to strip the resist, depending on the thickness of the resist, treatment of the resist and the number of wafers. Use the abort option in the last step if you sample requires a shorter stripping time.

Program 01: time = 10 min

Program 02: time = 30 min

Program 04: time = 60 min

56

Rem
Res

Removal of metal traces in RCA-2 (#residue504)

NL-CLR-WB09

Purpose: removal of metal traces originating from plasma tools in order to protect the cleaning efficiency of the wet benches. For this reason, RCA-2 is compulsory in case you continue:

- cleaning in the Pre-Furnace Clean (WB14-MFP)
- processing in the Ultra-Clean Line - Front End (WB12-UCP)
- processing in the Ultra-Clean Line - Back End (WB13-UCP)

Chemicals: HCl:H2O2:H2O (1:1:5 vol.%)

PLEASE NOTE

- 1. CAUTION:** do not process substrates with metal patterns in RCA-2.
- 2. NO REUSE:** reuse of RCA-2 is forbidden! Contact the administrator in case there is no empty RCA-2 beaker available in WB09.

Procedure:

- Pour 1500ml* of DI water into the beaker
- Turn on the stirrer
- Add 300ml* of Hydrogen Chloride (HCl)
- Heat up the solution to 70°C (setpoint heater = 80°C)
- Slowly add 300ml* of Hydrogen Peroxide (H2O2)
- Submerge your samples as soon as the temperature is above 70°C
- Time = 15min

* Use a glass graduated cylinder of 500ml to measure the volume of the chemicals.

skipped

57

ILP

Rinsing (#rinse001)

NL-CLR-WBs QDR

Purpose: removal of traces of chemical agents.

skipped

Choose one of the two rinsing modes:

QDR = Quick dump rinsing mode

Cascade = Overflow rinsing mode for fragile substrates

Rinse until message 'End of rinsing process' is shown on the touchscreen of the QDR, else repeat the rinsing process.

58

ILP

Substrate drying
(#dry001)

NL-CLR-WBs (ILP)

skipped

Single substrate drying:

1. Use the single-wafer spinner
Settings: 2500 rpm, 60 sec (including 45 sec nitrogen purge)
2. Use the nitrogen gun (fragile wafers or small samples)

etch1653: Directional DRIE of Silicon STD - high etch rate at 0°C (SPTS Pegasus)

59

ILP

DRIE of Silicon STD
(#etch241)

NL-CLR-SPTS Pegasus
Application: BOSCH high etch rate etching of microstructures.
Recipe: #B-Si etch @0degC #etch241

Etch Pre-
shapes top
oxide side

Settings:

- Platen temp: 0°C
- He pressure: 20Torr

Step (in order)	Deposition	Break (boost)	Etch
Time (sec)	2	1.3	5.7
C4F8 flow (sccm)	400	0	0
SF6 flow (sccm)	0	350	800
APC (mTorr/%valve)	8%	100%	8%
ICP (W)	3000	3000	3000
CCP – RF (W)	0	300	40

Check the process sheet for settings and details:

[https://mesaplusnanolab.ewi.utwente.nl/mis/generalinfo/downloads/usermanuals/268/Process%20sheet%20-%20SPTS%20-%20Si%20etch%20basic%20\[etch2xx\]%20sept%202018.pdf](https://mesaplusnanolab.ewi.utwente.nl/mis/generalinfo/downloads/usermanuals/268/Process%20sheet%20-%20SPTS%20-%20Si%20etch%20basic%20[etch2xx]%20sept%202018.pdf)

60

ILP

Chamber - Chuck Clean
(#etch219)

NL-CLR-SPTS Pegasus

Application: removal of organic and fluorocarbon residues from the chuck and chamber wall.
Recipe: #A-Clean after use #etch219

Parameters:

O2 flow: 200sccm
Pressure: 5mTorr
ICP: 2500W
CCP: 20W (RF)
Time: 15min

Note: after cleaning the substrate holder temp will be set to 20°C. Perform this recipe at the moment you are done etching.

61

ILP

Stripping of Resists and Fluorocarbon
(#strip104)

WARNING - PLEASE READ

This recipe is efficient for stripping of fluorocarbon in microstructures with aspect ratios < 5. Contact the administrator in case you want to strip fluorocarbon in microstructures with aspect ratios > 5 or fluorocarbon in nanostructures. This recipe attacks silicon and nitride coatings on the nanometer scale!

NL-CLR-TePla360

Application: stripping of resists and fluorocarbon after DRIE BOSCH processing by O2/CF4 plasma.

Step	O2 (sccm)	Ar (sccm)	CF4 (sccm)	H2 (sccm)	P (mbar)	Power (W)	Time (h:mm:ss)
Preheating	0	600	0	0	0.6	1000	0:10:00
Resist stripping	250	0	0	0	0.5	800	*
Fluorocarbon stripping	237	0	13	0	0.5	800	0:01:00
Residual Fluorocarbon stripping	250	0	0	0	0.8	800	0:01:00

* Select one of the following recipes depending on the thickness of the resist, treatment of the resist and the number of wafers.

Recipe 035: time = 10min

Recipe 037: time = 20min

Recipe 036: time = 60min

To remove
FC
Recipe 35

10 min
preheating in
600 sccm Ar
0.6mBar
1000W
10 min
ashing in 250
sccm O2 at
0.5mBar
800W
1 min
Polymer
removal in
237 sccm O2
at 0.5mBar
800W
1 min
FLuorine
removal in
250 sccm O2
at 0.8mBar
800W

BACKUP: The TePla300 is not a backup for this processing! If the TePla360 is down, contact the administrator.

PLEASE NOTE It is mandatory to remove metal traces originating from plasma tools in RCA-2 (residue1505), e.g. plasma etching or stripping in O₂ plasma, in case you:

- continue with UCP processing
- continue with high-temperature processing (MFP)

62

Rem
Res

Removal of metal traces in RCA-2
(#residue504)

NL-CLR-WB09

Purpose: removal of metal traces originating from plasma tools in order to protect the cleaning efficiency of the wet benches. For this reason, RCA-2 is compulsory in case you continue:

- cleaning in the Pre-Furnace Clean (WB14-MFP)
- processing in the Ultra-Clean Line - Front End (WB12-UCP)
- processing in the Ultra-Clean Line - Back End (WB13-UCP)

Chemicals: HCl:H₂O₂:H₂O (1:1:5 vol.%)

PLEASE NOTE

- 1. CAUTION:** do not process substrates with metal patterns in RCA-2.
- 2. NO REUSE:** reuse of RCA-2 is forbidden! Contact the administrator in case there is no empty RCA-2 beaker available in WB09.

Procedure:

- Pour 1500ml* of DI water into the beaker
- Turn on the stirrer
- Add 300ml* of Hydrogen Chloride (HCl)
- Heat up the solution to 70°C (setpoint heater = 80°C)
- Slowly add 300ml* of Hydrogen Peroxide (H₂O₂)
- Submerge your samples as soon as the temperature is above 70°C
- Time = 15min

* Use a glass graduated cylinder of 500ml to measure the volume of the chemicals.

Piranha clean
for 30 mins at
90°C to remove
fluorocarbons

63

ILP

Rinsing
(#rinse001)

NL-CLR-WBs QDR

Purpose: removal of traces of chemical agents.

Choose one of the two rinsing modes:

QDR = Quick dump rinsing mode

Cascade = Overflow rinsing mode for fragile substrates

Rinse until message 'End of rinsing process' is shown on the touchscreen of the QDR, else repeat the rinsing process.

64

ILP

Substrate drying
(#dry001)

NL-CLR-WBs (ILP)

Single substrate drying:

1. Use the single-wafer spinner
Settings: 2500 rpm, 60 sec (including 45 sec nitrogen purge)
2. Use the nitrogen gun (fragile wafers or small samples)

followed by
drying on
120°C hotplate
for 2 minutes
to evaporate
water out of
the pre-shape
structures

65

(Optional) 2
min native
oxide
removal in
1%HF for 2
minutes
followed by
QDR, spin
drying and
drying on a
120°C hotplate
for 2 minutes

etch1105: Gas-Phase Etching of Silicon using XeF₂ (Xactix)

66

ILP

Chamber clean (TEtske)
(#etch198)

NL-CLR-TEtske

Application: removal of organic and fluorocarbon residues on the chamber wall.

Select the correct etch chamber and electrode for your etch process (see next step).

- Electrode temperature: 10°C
- Valve position: 15% (resulting in a pressure of ~42mTorr)
- O₂ flow: 50sccm
- Power: 100Watt
- Time: 10 min
- Load: 54%
- Tune: 23%

The etch chamber is clean at the moment the plasma color is white and the DC bias is >500V.

67

ILP

Pre-conditioning for XeF₂ (#etch106)

NL-CLR-Tetske

Application: pre-conditioning step for gas-phase etching of Silicon with XeF₂

Select the clean chamber and the styros electrode.

Settings:

- Electrode temperature: 10°C
- Pressure: 10mTorr
- CHF₃ flow: 25sccm
- O₂ flow: 5sccm
- Power: 60Watt
- Time: 2min

68

ILP

Gas-phase etching of microchannels #etch103

NL-CLR-Xactix XeF₂

Standard settings:

- Temperature expansion chamber: 40°C
- Temperature etch chamber: 35°C
- Base pressure: 0.3Torr
- Loading/unloading: 3 purges with N₂

Adjustable settings in normal etch mode:

	Setting	Range
XeF ₂ pressure*	3Torr	0.5-6.0Torr
N ₂ pressure	-	0.0-20.0Torr
Etch time	30s	1-180s
# of cycles	see comment	1-100 cycles

*XeF₂ pressure is the expansion chamber pressure.

The number of cycles depends on the depth of the channel. Write down the target etch depth of the channel, the number of cycles and lot number(s) of the etching run(s) in the user comment.

Etch time must be adjusted to loading. Higher pressure and lower cycle times are preferred.